André Mendes Antunes

Licenciado em Ciências de
Engenharia Eletrotécnica e de Computadores

A Smart IoT Node using a Hybrid Edge-Computing Strategy for Environmental Multiparameter Sensing

Dissertação para obtenção do Grau de Mestre em

Engenharia Eletrotécnica e de Computadores

Orientador:	João Pedro Abreu de Oliveira, Prof. Doutor, Universidade Nova de Lisboa - Faculdade de Ciências e Tecnologia

Júri

Presidente:	Doutor João Almeida das Rosas - FCT/UNL
Arguentes:	Doutor Nuno Filipe Silva Veríssimo Paulino - FCT/UNL
	Doutor João Pedro Abreu de Oliveira - FCT/UNL

FACULDADE DE
CIÊNCIAS E TECNOLOGIA
UNIVERSIDADE NOVA DE LISBOA

Março, 2021

A Smart IoT Node using a Hybrid Edge-Computing Strategy for Environmental Multiparameter Sensing

Este documento foi gerado utilizando o processador (pdf)LaTeX, com base no template "novathesis" [1] desenvolvido no Dep. Informática da FCT-NOVA [2].
[1] https://github.com/joaomlourenco/novathesis [2] http://www.di.fct.unl.pt

"I've actually not read any books on time management."
- Elon Musk

Acknowledgements

First of all i would like to express my gratitude to my supervisor Professor João Pedro Oliveira for his hard work, support and advice throughout this dissertation. In spite of the ongoing pandemic and the difficult situation we faced, he always managed to provide prompt help and guidance, which lead to the results that were achieved.

I would also like to thank my parents, mostly for creating me, but also for their patience, support and prompt reminders to keep myself fed throughout these five years.

Thanks to my cousin, as well, for his patience and ready availability to read and spellcheck this dissertation about a subject completely foreign to him.

And lastly, thank you to all my friends who provided fun, entertaining, memorable, but also sometimes weird moments which helped me keep some glimmer of mental sanity throughout the whole college experience.

Abstract

The Internet of Things (IoT) has been growing at an immense pace over the last few years and there are no predictions of slowing down anytime soon, but most importantly, not only has it been growing in size but it has also been growing in capabilities, performance and diversity. Diversity is incredibly important but also fracturing, in this context. As IoT sensor nodes get more performant and diverse, their adaptability and reconfigurability ends up being lost in the search for ultimate performance.

As a way to unify these individual single purpose sensor nodes, a need and an opportunity present themselves to develop a singular multi-parameter, multi-sensor IoT node, that can make use of the latest reconfigurable technology to adapt itself to the requirements of each type of sensor, while maintaining the very high performance and precision of dedicated sensor nodes.

This dissertation work will thus focus on developing an architecture and building a prototype circuit board for a multi-sensor, reconfigurable IoT node based on a state-of-the-art System-on-Chip (SoC) with extremely high resolution measurement capabilities, which can interface with virtually any type of existing sensor. This architecture and prototype are intended to serve as a stepping stone in the path to develop a capable IoT node which can interface with a wider range of sensor and have a higher precision than what is currently available.

Keywords: IoT, Sensor Node, Flexible, Reconfigurable, High-Precision, SoC

Resumo

A *Internet of Things (IoT)* tem vindo a crescer a passos largos ao longo dos últimos anos, e não apresenta quaisquer sinais de abrandar o seu crescimento num futuro próximo. No entanto, não só tem vindo a crescer em tamanho, mas também nas suas capacidades, performance e diversidade. Enquanto que a diversidade é extremamente importante, neste contexto, é também fraturante. À medida que os nós IoT melhoram em performance e diversidade, a sua adaptabilidade e reconfigurabiliade acaba por ficar em segundo plano na procura do pico de performance.

Com o objetivo de unificar estes nós de sensores com propósitos singulares, apresenta-se uma oportunidade e uma necessidade de desenvolver um único nó IoT capaz de fazer interface com uma multiplicidade de sensores distintos, usando tecnologia de ponta reconfigurável para se adaptar às necessidades de cada tipo de sensor, mantendo ainda assim a alta performance e precisão de nós de sensor dedicados.

A presente dissertação irá então focar-se no desenvolvimento de uma arquitetura de sistema e criação de um protótipo em placa de circuito impresso referente a um nó IoT multisensor reconfigurável, baseado num SoC de última geração com capacidades de medição extremamente elevadas, que consiga fazer interface com qualquer tipo de sensor existente. Esta arquitetura de sistema e protótipo são desenvolvidos com a intenção de servirem como ponto de partida para o desenvolvimento de um nó IoT de interface com sensores, que tenha a capacidade de medir qualquer tipo de sensor com uma precisão superior àquilo que está atualmente disponível.

Palavras-chave: IoT, Nó de Sensores, Flexível, Reconfigurável, Alta Precisão, SoC

Contents

List of Figures xvii

List of Tables xix

Listings xxi

Acronyms xxiii

1 Introduction 1

1.1 Motivation . . . 1
1.2 Objectives . . . 2
1.3 Contributions . . . 2
1.4 Organization . . . 3

2 Research and Concept Work 5

2.1 IoT: Internet of Things . . . 6
2.1.1 IoT Node . . . 6
2.1.2 Microcontroller . . . 7
2.1.3 Communication . . . 8
2.2 Sensors for Environmental monitoring . . . 10
2.2.1 Temperature Sensors . . . 11
2.2.2 Conductivity Sensors . . . 11
2.2.3 pH Sensors . . . 13
2.3 Data Acquisition and Conversion . . . 14
2.3.1 Voltage Measurement . . . 14
2.3.2 Current Measurement . . . 15
2.3.3 Successive Approximation Register ADC . . . 15
2.3.4 Delta-Sigma ADC . . . 16
2.4 Reconfigurable Hardware . . . 17
2.4.1 Reconfigurable Digital Systems . . . 17
2.4.2 Reconfigurable Analog Systems . . . 18
2.5 Edge Computing . . . 19
2.6 Concept Work . . . 20

2.6.1 Design and Architecture 20
2.6.2 Block Diagram for the Proposed Architecture 22
2.6.3 Preliminary Testing 22

3 Board Development **25**
3.1 Hardware Development 26
3.1.1 Final Component Selection 27
3.1.2 Noise Considerations 28
3.1.3 Radio Frequency Section 29
3.1.4 High Precision Analog Front End 31
3.1.5 Channel Multiplexers 33
3.1.6 Board Assembly 34
3.1.7 Power Consumption Considerations 35
3.2 Software Development 38
3.2.1 PSoC Creator 38
3.2.2 Analog Channel Selection 40
3.2.3 USBUART Transmit and Receive 40
3.2.4 Sensor Data Acquisition 41

4 Board Testing **45**
4.1 Testing of the Multiplexers 46
4.2 Testing the Internal Delta-Sigma ADC with Low Value Resistors 47
4.2.1 20-Bit Mode 48
4.2.2 18-Bit Mode 50
4.2.3 16-Bit Mode 52
4.2.4 14-Bit Mode 54
4.2.5 Drawing Conclusions From the Data 56
4.3 Testing the Internal Delta-Sigma ADC with High Value Resistors and Investigation into the Current DAC 59
4.3.1 20-Bit Mode 60
4.3.2 18-Bit Mode 60
4.3.3 16-Bit Mode 60
4.3.4 Measuring the Voltage of an External Battery 61
4.3.5 Comparing the Developed PCB with a Prototyping Kit 62
4.4 Testing the AD5941 Analog Front End and u-blox SARA-N2 NB-IoT Module 63

5 Conclusion **67**
5.1 Future Work 68

Bibliography **71**

A Code For the Initial MUX and ADC Experiments **77**

B IoT Node Schematic and Layout **81**

C PSoC Creator Analog Routing Window **95**

D MATLAB Script for Sampled Data Processing **97**

List of Figures

2.1 IoT Node Architecture Block Diagram. 7
2.2 Sub-optimal power usage when using a single core architecture. 8
2.3 Optimized power usage when using multiple core architectures. 8
2.4 Representation of a conductivity sensor, adapted from [26]. 12
2.5 Compensation Voltage in relation to pH of the measured solution, adapted from [30]. 14
2.6 Flowchart of the functioning principle of SAR ADCs, adapted from [33]. . . 15
2.7 Graphical representation of the possible paths in a SAR ADC, adapted from [34]. 16
2.8 Basic architecture of a Delta - Sigma DAC, adapted from [34]. 17
2.9 Basic architecture of an FPGA, adapted from [35]. 17
2.10 Basic architecture of an FPAA, adapted from [41]. 18
2.11 Edge vs Cloud Computing, adapted from [44]. 19
2.12 Comparison of the simplified block diagram of the ADuCM355 and the AD5941 Analog Front-End (AFE) modules, obtained from the respective product data sheets, [46] and [47], respectively. 21
2.13 Block diagram of the proposed IoT Node. 22
2.14 System implemented in PSoC Creator for testing. 23

3.1 High Precision Analog Front End Daughter Board Schematic. 26
3.2 Finalized block diagram of the proposed IoT Node. 27
3.3 SARA-N2 block diagram, obtained from the module's data sheet [51]. 30
3.4 AD5941 Block Diagram, obtained from the product's data sheet [47]. 32
3.5 High Precision Analog Front End Daughter Board Layout. 33
3.6 3D Render of the IoT Node's PCB and AD5941 Daughter Board. 34
3.7 Block Diagram on the "Top Design" Window of PSoC Creator. 38
3.8 Configuration Page of the Delta-Sigma ADC in PSoC Creator. 42

4.1 Picture of the assembled IoT Node and AD5941 Daughter Board. 45
4.2 Internal Configuration of the MAX14661 Multiplexers. 46
4.3 Results of measurements using 20-bit $\Delta - \Sigma$, Multi Sample (Turbo), SR = 92 SPS, Buf. Gain = 2, 5.000 Samples per Measurement. 48
4.4 Results of measurements using 20-bit $\Delta - \Sigma$, Multi Sample (Turbo), SR = 182 SPS, Buf. Gain = 1, 5.000 Samples per Measurement. 49

4.5 Results of measurements using 18-bit $\Delta - \Sigma$, Multi Sample (Turbo), SR = 1238 SPS, Buf. Gain = 2, 10.000 Samples per Measurement. 50
4.6 Results of measurements using 18-bit $\Delta - \Sigma$, Multi Sample (Turbo), SR = 2477 SPS, Buf. Gain = 1, 10.000 Samples per Measurement. 51
4.7 Results of measurements using 16-bit $\Delta - \Sigma$, Multi Sample (Turbo), SR = 5505 SPS, Buf. Gain = 2, 20.000 Samples per Measurement. 52
4.8 Results of measurements using 16-bit $\Delta - \Sigma$, Multi Sample (Turbo), SR = 11010 SPS, Buf. Gain = 1, 20.000 Samples per Measurement. 53
4.9 Results of measurements using 14-bit $\Delta - \Sigma$, Multi Sample (Turbo), SR = 14840 SPS, Buf. Gain = 2, 20.000 Samples per Measurement. 54
4.10 Results of measurements using 14-bit $\Delta - \Sigma$, Multi Sample (Turbo), SR = 29861 SPS, Buf. Gain = 1, 20.000 Samples per Measurement. 55
4.11 Comparison of Internal and External Reference Noise Performance, from [54]. 57
4.12 Comparison between single ended and differential noise performance, from [54] 58
4.13 Oscilloscope trace of the AD5941's 1.82 V Regulator. 63
4.14 Oscilloscope trace of the AD5941's 2.5 V Regulator. 64
4.15 Logic Analyzer Data of a SPI Write Command to the AD5941. 64
4.16 Logic Analyzer Data of a SPI Read Command to the AD5941. 65

B.1 3D Render of the IoT Node's PCB and AD5941 Daughter Board. 81
B.2 Sensor Node Schematic, Page 1. 82
B.3 Sensor Node Schematic, Page 2. 83
B.4 Sensor Node Schematic, Page 3. 84
B.5 Sensor Node Schematic, Page 4. 85
B.6 Sensor Node Schematic, Page 5. 86
B.7 Sensor Node Schematic, Page 6. 87
B.8 Sensor Node Layout, Top Copper Layer. 88
B.9 Sensor Node Schematic, First Inside Copper Layer. 89
B.10 Sensor Node Schematic, Second Inside Copper Layer. 90
B.11 Sensor Node Schematic, Bottom Copper Layer. 91
B.12 Sensor Node Schematic, Top Silkscreen. 92
B.13 Sensor Node Schematic, Bottom Silkscreen. 93

C.1 PSoC Creator Analog Routing. 95

List of Tables

2.1 Comparison of metrics on wireless communication protocols. 9

4.1 Noise values of measurements using 20-bit $\Delta - \Sigma$, Multi Sample (Turbo), SR = 92 SPS, Buf. Gain = 2, 5.000 Samples per Measurement. 48

4.2 Noise values of measurements using 20-bit $\Delta - \Sigma$, Multi Sample (Turbo), SR = 182 SPS, Buf. Gain = 1, 5.000 Samples per Measurement. 49

4.3 Noise values of measurements using 18-bit $\Delta - \Sigma$, Multi Sample (Turbo), SR = 1238 SPS, Buf. Gain = 2, 10.000 Samples per Measurement. 50

4.4 Noise values of measurements using 18-bit $\Delta - \Sigma$, Multi Sample (Turbo), SR = 2477 SPS, Buf. Gain = 1, 10.000 Samples per Measurement. 51

4.5 Noise values of measurements using 16-bit $\Delta - \Sigma$, Multi Sample (Turbo), SR = 5505 SPS, Buf. Gain = 2, 20.000 Samples per Measurement. 52

4.6 Noise values of measurements using 16-bit $\Delta - \Sigma$, Multi Sample (Turbo), SR = 11010 SPS, Buf. Gain = 1, 20.000 Samples per Measurement. 53

4.7 Noise values of measurements using 14-bit $\Delta - \Sigma$, Multi Sample (Turbo), SR = 14840 SPS, Buf. Gain = 2, 20.000 Samples per Measurement. 54

4.8 Noise values of measurements using 14-bit $\Delta - \Sigma$, Multi Sample (Turbo), SR = 29861 SPS, Buf. Gain = 1, 20.000 Samples per Measurement. 55

4.9 Signal-to-Noise Ratio of measurements using 20-bit $\Delta - \Sigma$, Multi Sample (Turbo), SR = 182 SPS, Buf. Gain = 1, 5.000 Samples per Measurement. 57

4.10 Signal-to-Noise Ratio of measurements using 20-bit $\Delta - \Sigma$, Multi Sample (Turbo), SR = 182 SPS, Buf. Gain = 1, 5.000 Samples per Measurement. 57

4.11 Noise values of measurements using 20-bit $\Delta - \Sigma$, Multi Sample (Turbo), SR = 182 SPS, Buf. Gain = 1, 5.000 Samples per Measurement. 60

4.12 Noise values of measurements using 18-bit $\Delta - \Sigma$, Multi Sample (Turbo), SR = 2477 SPS, Buf. Gain = 1, 10.000 Samples per Measurement. 60

4.13 Noise values of measurements using 16-bit $\Delta - \Sigma$, Multi Sample (Turbo), SR = 11010 SPS, Buf. Gain = 1, 20.000 Samples per Measurement. 60

4.14 Noise values of measurements using 20-bit $\Delta - \Sigma$, Multi Sample (Turbo), SR = 182 SPS, Buf. Gain = 1, 5.000 Samples per Measurement, comparing a battery and a resistor. 61

4.15 Comparison of noise values of measurements using 20-bit $\Delta - \Sigma$, Multi Sample (Turbo), SR = 182 SPS, Buf. Gain = 1, 5.000 Samples per Measurement, comparing the and a resistor. 62

Listings

A.1 Code for Inicial MUX and ADC Experiments 77
D.1 MATLAB Script 97

Acronyms

$\Delta - \Sigma$	Delta-Sigma.
μC	Microcontroller.
R_{ON}	ON Resistance.
AC	Alternating Current.
ADC	Analog to Digital Converter.
AFE	Analog Front-End.
ALU	Arithmetic Logic Unit.
ARM	Advanced RISC Machine.
ASIC	Application Specific Integrated Circuit.
BGA	Ball Grid Array.
BLE	Bluetooth Low Energy.
CAB	Computational Analog Block.
CI	Confidence Interval.
CO	Carbon Monoxide.
CO_2	Carbon Dioxide.
DAC	Digital to Analog Converter.
EDA	Electronic Design Automation.
FPAA	Field Programmable Analog Array.
FPGA	Field Programmable Gate Array.
FPU	Floating Point Unit.
GPIO	General Purpose I/O.

I_2C	Inter-Integrated Circuit.
I/O	Input/Output.
IC	Integrated Circuit.
IDE	Integrated Design Environment.
IoT	Internet of Things.
ITU-T	International Telecommunication Union – Telecommunication Standardization Sector.
LoRa	Long Range.
LSB	Least Significant Bit.
LTE	Long-Term Evolution.
MSB	Most Significant Bit.
MUX	Multiplexer.
NB-IoT	Narrowband Internet of Things.
NO_2	Nitrogen Dioxide.
O_3	Ozone.
PCB	Printer Circuit Board.
PLB	Programmable Logic Block.
$PM_{2.5}$	Particulate Matter.
PSoC	Programmable System-on-Chip.
QFN	Quad Flat No-Leads.
QFP	Quad Flat Package.
RFID	Radio-frequency identification.
RMS	Root Mean Square.
RTD	Resistance Temperature Detector.
SAR	Successive Approximation Register.
SNR	Signal to Noise Ratio.
SO_2	Sulfur Dioxide.
SoC	System-on-Chip.
SPI	Serial Peripheral Interface.

TDS	Total Dissolved Solids.
TIA	Transimpedance Amplifier.
UART	Universal Asynchronous Receiver/Transmitter.
USB	Universal Serial Bus.
VCO	Volatile Organic Compounds.
WSN	Wireless Sensor Network.

Chapter 1

Introduction

1.1 Motivation

Over the last few years, the Internet of Things has been growing at an incredibly fast rate, bringing together human controlled devices and independent "things"in the same network. These independent devices come in all shapes and forms, and in innumerous contexts.

In consumer applications, it's possible to find a plethora of smart home devices, from lamps, to speakers, to voice assistants, to smart outlets, or even network connected appliances such as fridges and washing machines, or even doorbells and smart thermostats.

In industrial applications, IoT is making an enormous breakthrough, with the denominated Industry 4.0, where even manufacturing equipment is network connected, enabling features like process control, where sensors can monitor the status of an assembly line and relay it in real time to a central hub. In the agricultural sector, IoT is enabling the collection of vasts amount of data, from soil sensors like moisture or pH to air quality and crop growth, helping farmers optimize their production.

In commercial applications, it's easy to find many IoT devices in the transportation industry, from simple electronic toll collection systems to fleet vehicle locators and even devices to remotely disable a vehicle in case of theft. But also in the medical industry, where IoT devices can permanently monitor a patient's vitals and warn them, or even call the emergency services, in case of need.

In infrastructures, IoT makes possible the implementation of city wide smart controlled traffic lights, with the help of sensors and cameras, in order to optimize the flow of traffic.

IoT devices are becoming ubiquitous, numbering in the tens of billions, yet they all need to be connected to the network, congesting access points due to the need for an individual connection to each one, which is exactly one of the problems where WiFi 6 tries to improve upon its predecessor.

1.2 Objectives

With the amount and variety of specialized connected IoT devices, and specially the amount of different sensor interfacing nodes, the need for a unified platform where all types of sensors, from all the different areas where IoT is deployed, can be connected, read and processed, becomes very apparent.

This is exactly the problem this thesis intends to help solve, by creating a general purpose sensor interface node, with high precision and processing capabilities, as well as the ability to interface with a significant number and variety of sensors at once.

To achieve this, a highly reconfigurable architecture must be designed and optimized, such that the same IoT node can be as adaptable to the connected sensors as possible, while maintaining high performance in as many areas as possible.

1.3 Contributions

The present dissertation made several important contributions related to the development of an advanced IoT sensor node, such as:

- Design of a system architecture for a high precision IoT capable of reading data from multiple sensors, process it, and transmit it;
- Implementation of the designed system architecture in KiCad, a first use of this software, through the creation of a schematic and its layout;
- Physical production of the proposed and implemented IoT node through JLCPCB, the first use of this PCB manufacturer;
- Creation of a first generation prototype of the high precision IoT sensor node;
- Extensive testing of the Programmable System-on-Chip (PSoC) microcontroller, with focus on its signal acquisition capabilities, which found some incredibly good but also unexpected and insightful results;
- First contact with the AD5941 Analog Front End Integrated Circuit (IC), which increased knowledge about its operational principles and control library.

1.4 Organization

This dissertation starts with Chapter 1: Introduction, where there is an overview of the factors that led to the development of this work, and the problems it intends to solve.

The second chapter, named Research and Concept Work, tries to compile some of the previous developments in the area being studied, as a way to bring the reader up to speed with the subjects being researched and discussed, then proceeds to introduce some of the planning work done in the early development.

Chapter 3 is where the brunt of the development work is explained, starting with the Hardware side of the problem, there is a description of the challenges faces when creating the IoT node, as well as some of the design considerations around both the Analog and the RF sections, which are both highly sensitive and intolerant of each other. There is then a summary of the software side of the IoT node which explains some of the core functions and functionalities that had to be implemented in order to make this node work.

The fourth chapter centers itself around the testing of the IoT node. The described tests feature only resistances as a simulation of the sensor's output, but are very good at achieving their purpose, which is to characterize the capabilities of the developed sensor node in terms of high precision measurement.

Finally, the Conclusion makes a brief summary of the work developed and possible future developments.

Chapter 2

Research and Concept Work

This chapter intends to present an overview into the work previously developed on the subject of this thesis, so as to better understand the main issues that arise when attempting to design an IoT Node for Environmental Multiparameter Sensing.

It starts with a general overview of the Internet of Things, as well as its building blocks, the IoT Nodes. Then proceeds to give more in depth information about the components that constitute an IoT Node, focusing on the Microcontroller, Communication methods and Data Acquisition systems.

The second section refers to the different types of sensors available for environmental sensing, focusing on three types of possible mediums: Air, Water and Soil. Multiple sensors are briefly presented, in an attempt to characterize the most relevant ones and understand their mode of operation.

In the third section, various methods for data acquisition are investigated, as a means to interface with the researched sensors.

Following this, in the fourth section, a short overview is given about reconfigurable hardware, namely the Field Programmable Gate Array (FPGA) and the Field Programmable Analog Array (FPAA).

In the fifth section, the subject of edge computing is introduced and discussed.

To end this chapter, there is a small section with the concept work done before finally deciding on a definitive architecture for the IoT Node.

2.1 IoT: Internet of Things

The concept of Internet of Things is intertwined with that of Wireless Sensor Network (WSN). It can be very widely defined, for example, in [1] the IoT is said to be "a paradigm of connecting heterogeneous devices around the world", and in [2] it's defined as "the convergence of Internet with Radio-frequency identification (RFID), Sensor and smart objects". However, in 2012, the International Telecommunication Union – Telecommunication Standardization Sector (ITU-T) published a Recommendation [3], where it defines the IoT as "a global infrastructure for the information society, enabling advanced services by interconnecting (physical and virtual) things based on existing and evolving interoperable information and communication technologies". However the gist of it is that the IoT can simply be defined as a group of computing devices that are provided with unique identifiers and are able to transfer data over a network without human intervention.

The Internet of Things has been enabled by somewhat recent advancements in sensor and communication technology, such as the development of faster and more energy efficient means of communication like Bluetooth Low Energy (BLE), ZigBee or Long Range (LoRa) [4], as well as the increasing efficiency and data processing capabilities of current microcontrollers due to more advanced architectures, more efficient instruction sets and smaller fabrication nodes, as well as purpose-built microcontrollers for IoT devices [5].

2.1.1 IoT Node

An IoT Node represents the remote device on an IoT Network and, as such, each IoT Node must be fully capable of data acquisition and transmission.

According to [6], an IoT Node architecture consists of 6 main components:

- Power Management,
- Microcontroller,
- Data Storage,
- Communication,
- Data Acquisition and Conversion,
- Sensors.

Considering these main components, a block diagram of a typical IoT Node is shown in Figure 2.1.

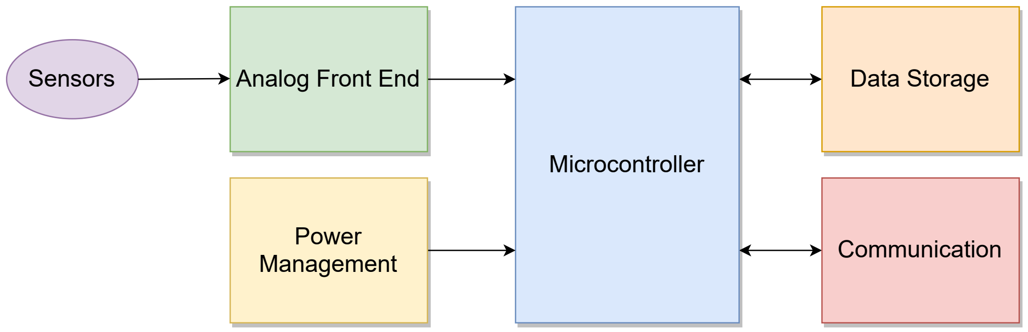

Figure 2.1: IoT Node Architecture Block Diagram.

2.1.2 Microcontroller

One of the primary components of an IoT Node is its microcontroller. This component is responsible for the implementation of communication protocols, reconfigurable systems, if present, smart control of power usage and local processing of data. Classically, the microcontroller of an IoT Node is of the “fixed function” type, however new architectures have started to use reconfigurable hardware, such as FPGAs. This section will focus only on “fixed function” microcontroller, while reconfigurable architectures will be discussed in Section 2.4.

Advancements in technology have brought about immense gains in processing power and efficiency over the years, not only through improvements in the technology node of processors, but also through the development of more energy efficient instruction sets like Advanced RISC Machine (ARM), as compared to x86 [7, 8]. This means that ever smaller devices can be built, while maintaining very high local processing power, which is necessary for most IoT devices.

With current technology it’s possible to have an IoT Node consuming only a few mW of power, while having an equivalent processing capability to that of a desktop computer from a few years ago, enabling better data processing at the node, without a need to transmit the acquired data to be processed elsewhere.

One of the contributors to this increase in efficiency comes from the ability to combine different types of interconnected cores inside of a single package. One example of this is ARM’s Big.LITTLE technology, where two different processing cores are combined, one of which has a smaller number of pipeline stages, resulting in better energy efficiency at the cost of reduced performance, while the other has a longer pipeline, resulting in higher performance and energy consumption. This leads to a processor that manages to achieve both high performance and low power consumption at low load conditions [9].

An example of how a system like this might work can be found below, in Figures 2.2 and 2.3, based on a similar diagram by [10].

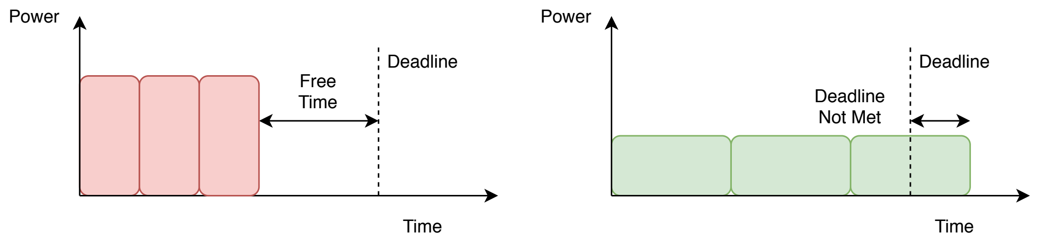

(a) High Performance Core (b) High Efficiency Core

Figure 2.2: Sub-optimal power usage when using a single core architecture.

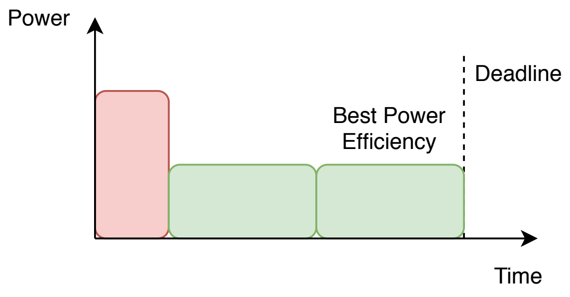

Figure 2.3: Optimized power usage when using multiple core architectures.

A more recent contribution to the advancement in processing capability for IoT has been processor specialization, with architectures developed specifically for IoT platforms, focused on energy efficiency, like ARM's Cortex-M line of Microcontroller Processors, which have a very small die area and thus low cost, while retaining high energy efficiency and considerable processing power [11]. Another example is Cypress' PSoC series of microcontrollers, which can contain up to a pair of ARM Cortex-M series cores, using a similar principle to that of Big.LITTLE stated above, where one of the cores is the M4 model, designed for higher computational performance, and the other core is the M0+ model, designed for higher energy efficiency, while at the same time containing resources like communication modules, Digital to Analog Converter (DAC), Analog to Digital Converter (ADC) and memory systems on the same package, forming a complete SoC [5].

2.1.3 Communication

Another primary component of an IoT Node is a block responsible for the communications. Mainly acting as data acquisition modules, IoT Nodes have to relay the information they obtained to central processing, where it can displayed or processed. The IoT node can use many different forms of wired and wireless communication [4].

2.1.3.1 Wired Communication

The large majority of wired communication methods are based on either Serial or Universal Asynchronous Receiver/Transmitter (UART) technology, with the most common ones being Universal Serial Bus (USB), Serial Peripheral Interface (SPI) or Inter-Integrated Circuit (I_2C).

For the purpose of the IoT, one of the main advantages of wired communication is the reduced power consumption, with some interfaces, like USB, even having the ability to deliver power to the node through the same connector [12].

The main disadvantage of wired communication is obvious, in the fact that it is necessary to directly connect to the IoT Node, severely reducing the range at which it can be placed from the host computer. This is especially true given that the highest range achievable with the above listed wired communication methods is 100 meters, when using SPI.

2.1.3.2 Wireless Communication

Wirelessly is, without a doubt, the main form of communication for an IoT Node. However, this bring forward its own set of limitations, like reduced transmission rate and higher power consumption, so it's fundamental to compare these metrics between different wireless communication options, in order to optimize the performance of the Node. Making a comparison between:

- WiFi,
- BLE,
- ZigBee,
- LoRa,
- Narrowband Internet of Things (NB-IoT).

Using data from [4, 13–15], it's possible to synthesize the metrics for data rate, range and transmission power, as shown in Table 2.1.

Table 2.1: Comparison of metrics on wireless communication protocols.

Wireless Protocol	WiFi	BLE	ZigBee	LoRa	NB-IoT
Data Rate [Mbps]	11	1	0.25	0.11	0.23
Max. Range [m]	100	100	100	2000+	"Infinite"
Max. Transmission Power [mW]	1000+	100	35	35	840

With this data it's possible to assert that the best combination for an “all-purpose” IoT Node is to have 3 different forms of communication: WiFi, due to its vast support and high data rate, at the expense of power consumption; LoRa, which has a very reduced power consumption while maintaining a long range, albeit at the expense of data rate; and NB-IoT due to its ability to use one Resource Block on an existing Long-Term Evolution (LTE) network for communication, meaning that a Node with this communication system could be deployed wherever there is access to a cellular LTE network that supports NB-IoT.

2.2 Sensors for Environmental monitoring

Air Monitoring: Air pollution is one of the rising causes of death in recent times, with urban air pollution being responsible for 1.6 Million deaths every year in China alone, accounting for around 17% of all yearly deaths [16].

This is especially true in developing countries due, not only, to the rapid development of the industrial sector and the proliferation of person transport vehicles, but also to the very lax emission controls due to the local government's concerns of how pollution control may affect the country's economy, as it happens, for example, with China [17].

Air quality can be monitored by innumerous parameters, some of the most important ones being the concentrations of Carbon Monoxide (CO), Carbon Dioxide (CO_2), Nitrogen Dioxide (NO_2), Sulfur Dioxide (SO_2), Ozone (O_3), Volatile Organic Compounds (VCO) and Particulate Matter ($PM_{2.5}$). Besides air quality, there is also a possibility to measure general air parameters, like temperature, wind speed and noise.

With an IoT platform, it's possible to deploy a large number of air monitoring stations that can read the attached sensors and transmit the obtained data, as a way to replace or supplement pre-existing tools.

Water Monitoring: Water is an absolutely fundamental component for human survival and clean water is an ever more valuable resource, not only for drinking, but also for the industrial and agricultural sectors [18].

Water quality has a huge impact on human health and environmental conditions, as it can be one of the main methods of spreading disease. Contamination in water can be measured through several parameters, namely, pH, temperature, conductivity, turbidity and Total Dissolved Solids (TDS). These parameters provide a good overview about the quality and drink-ability of the water in question. Additionally several other parameters can be measured like water pressure and flow rate [19, 20].

Conventional water analysis methods consist of physically acquiring a water sample and examining in a lab. This process is expensive, time consuming, infrequent, and the water is usually tested at the source, meaning that, if there are pollutants in the pipes, those will not be detected [20, 21].

This means there is a need to put in place mechanisms to ensure the quality of drinking water in real time, and IoT is the perfect platform for implementing such a system due to the ability to develop a low cost, wireless, real time system that achieves all the necessary requirements.

Soil Monitoring: Knowing the quality of the soil can be fundamental for industries like agriculture and agronomy, where a high quality soil can lead to plentiful crops and a low quality soil can lead to a complete lack of growth.

Furthermore, monitoring plant health can help to make a better usage of fertilizing agents, be it by increasing or reducing usage, or by leading to a redistribution of fertilizer among a field [22].

The most important parameters to measure regarding soil quality are pH, moisture, temperature and electrical conductivity. This means that most sensors used to assert soil quality, apart from the moisture sensor, are also used for monitoring air and water parameters[23, 24].

2.2.1 Temperature Sensors

There are several types of temperature sensors, but the main three are Thermocouples, Thermistors and Resistance Temperature Detector (RTD)s.

Thermocouples are based on 2 different conductive material forming a junction. On this junction, due to the Seebeck effect, there will be a potential difference between the hot conductor and the cold one, thus enabling the measurement of temperature based on the potential difference observed. Different combinations of materials enable different working ranges for the thermocouples, with the possibility to measure from -200 °C (Type E Thermocouple) up to 1700 °C (Type B Thermocouple).

Thermistors are 2 wire semiconductor devices with a junction between materials that changes resistance with a change of temperature. These types or temperature sensors are very widely used due to their small size, reliability and relatively low cost.

Resistance Temperature Detectors are based on the change of resistance of materials due to temperature. One example of this is how a nickel based RTD with a nominal resistance of 1000 Ω will change approximately 5 Ω per °C [25].

2.2.2 Conductivity Sensors

Conductivity, measured in S/cm (siemens per centimeter) measures how well a solution conducts electricity, and pure water is a very poor conductor. This happens because the conductivity in water comes mostly from acids, bases, salts, and certain gases such as carbon dioxide, hydrogen chloride, and ammonia that dissolve into positive and negative ions, while pure water itself only conducts electricity due to its ability to dissociate into the hydrogen ion (H^+) and the hydroxyl ion (OH^-). As such, measuring conductivity in water is a very good indicator of ionic contaminants [26].

Electrode-based conductivity sensors are usually constituted by 1 or 2 pairs of electrodes. In 2 pair systems, an Alternating Current (AC) is forced through one of the pairs. Then, both current and voltage are read by analog channels, in order to calculate the conductivity [27, 28].

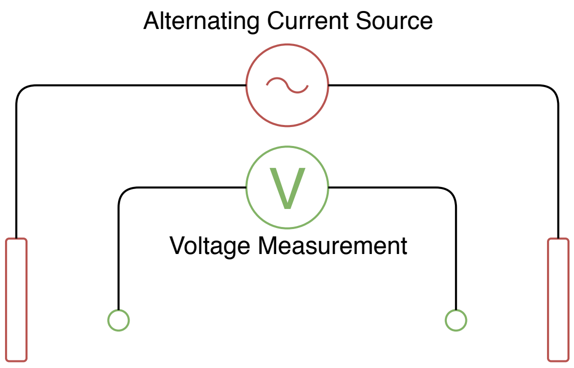

Figure 2.4: Representation of a conductivity sensor, adapted from [26].

There are also toroidal conductivity sensors that work in a similar way to their electrode counterparts. They are constituted by a pair or toroidal coils. When an AC voltage is applied to one of the coils, a current is induced on the second one, such that the amount of coupling between the coils is proportional to the conductivity of the solution [26].

2.2.2.1 Electronics for measuring conductivity sensors

Impedance measurement can be used for the conductivity sensor, as conductivity is directly proportional to the cell constant and inversely proportional to the measured resistance, leaving us with the equation:

$$\sigma = K_C \frac{1}{R}. \tag{2.1}$$

Meaning that, for this sensor, both the current flowing through it and the voltage at its terminals need to be known.

Furthermore, conductivity sensors also suffer from temperature drift, which means that a temperature sensor is needed to compensate this phenomenon, creating the need for an additional analog channel [26].

2.2.2.2 Temperature compensation of Conductivity Sensors

The conductivity of a solution increases with temperature, due to the higher mobility of the ions carrying the electrical current.

This means that any conductivity measurement also needs a temperature measurement, in order to compensate for this effect, however, the amount of compensation required depends on the solution being tested and the value of conductivity itself.

The most used type of compensation, that can be used for solutions above 10 µS/cm is the simple linear compensation, described by the equation:

$$\sigma_t = \sigma_{ref}[1 + \alpha(t - t_{ref})]. \tag{2.2}$$

In this equation, σ_t represents the conductivity at temperature t, σ_{ref} represents the measured sigma, α represents the temperature coefficient of the solution at temperature t_{ref} [27].

2.2.2.3 Total Dissolved Solids

TDS in water can be calculated as a function of conductivity, by multiplying the measured electrical conductivity of the water sample in question by a constant Ke, called the correlation factor, normally varying between 0.55 and 0.8 [29].

2.2.3 pH Sensors

pH is an indicator of how acidic or basic a solution is. In this scale, from 0 to 14, a lower value indicates that the measured solution is acidic, while a higher value indicates a basic or alkaline solution. In turn, acidity or alkalinity is determined by the relative concentrations of hydrogen ions (H^+) and hydroxyl ions (OH^-), respectively [30].

Its measurement is based on a pH-sensing electrode (made of a specially formulated glass), which develops a voltage potential depending on the pH of the solution and a reference electrode to which the voltage of the pH sensing electrode is compared.

2.2.3.1 Temperature compensation of pH Sensors

Similarly to what happens with conductivity, the pH of a solution increases with temperature. This means that any pH measurement also needs a temperature measurement, in order to compensate for this effect.

The change in pH with temperature follows a linear trend centering on pH 7, varying positively for values below 7 and negatively for values above, as can be seen in Figure 2.5, and described by the equation:

$$E = E^0 + \frac{dE^0}{dT}(T - 298.15K) - \frac{RT}{F}(2.303)\log pH. \tag{2.3}$$

In this equation, E represents the potential read between the pH and reference electrode, E^0 the standard potential of the pair, $\frac{dE^0}{dT}$ represents the standard change in potential with temperature, T the absolute temperature, R the universal gas constant, and F Faraday's constant.

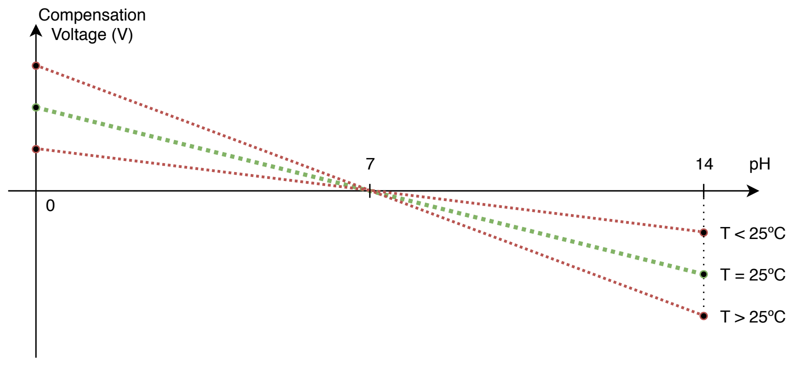

Figure 2.5: Compensation Voltage in relation to pH of the measured solution, adapted from [30].

2.3 Data Acquisition and Conversion

From Section 2.2, we can see that different types of sensors output their measured parameters differently. This means that, for an IoT Node to have the capability to read multiple sensors, it must also be able to have multiple ways of acquiring the data from those sensors.

This means that, for sensors in Section 2.2, at least 2 types of analog measurement channels are necessary:

- Voltage Measurement,
- Current Measurement.

2.3.1 Voltage Measurement

Measurement of analog sensors outputting their value in voltage is relatively straight forward, with the use of an ADC.

Most possible input signals will need a range change, in order to match the output of the sensor with the used ADC. For example, if the used ADC has a 0-5V range, and the output signal by the sensor is in the 0-1V range, a stage with gain 5 will be needed before the signal is sent to the ADC for measurement, in order to maximize the available resolution.

The employed ADC may also vary architecture depending on the requirements of the input signal. If an extremely fast sample rate is required, but outright resolution and power consumption can be compromised, a Pipeline ADC can be used. Alternatively, if a fast sample rate and low power consumption are required, while resolution is not the top priority, a Successive Approximation Register (SAR) ADC may be employed. However, if the sample speed is not the main focus, but resolution is essential, a Delta-Sigma ($\Delta - \Sigma$) ADC is the best choice [31].

2.3.2 Current Measurement

Current sensing involves a bit more work than measuring voltage. For starters, the same sort of voltage sensing ADC as was used for voltage measurement, must be used for current measurement, so a way to convert current to voltage is required. This is done mainly in 2 ways, through a shunt resistor, or a Transimpedance Amplifier (TIA).

A shunt resistor is a very low value resistor put in the current path in order to develop a low voltage at its terminals while causing minimal influence to the signal to be measured. However, for very small signals, a shunt can have a big impact on the signal to measure, and thus a TIA must be used.

A transimpedance amplifier is a type of amplifier that converts a current input to a voltage output while putting a near zero load on the signal. This type of amplifier is widely used to measure sensors when a very high accuracy is necessary [32].

2.3.3 Successive Approximation Register ADC

The SAR ADC is a relatively simple type of analog to digital converter that relies on the trivial flowchart shown in Figure 2.6 to function.

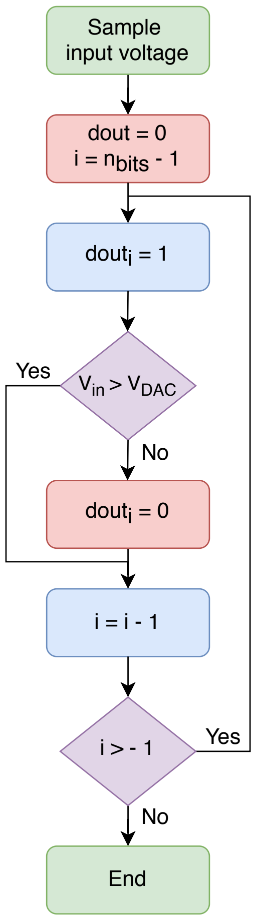

Figure 2.6: Flowchart of the functioning principle of SAR ADCs, adapted from [33].

What this means in practice, is that the converter successively halves the conversion scale in each iteration of the process and compares it to the signal, until it converges on the value of the analog input. For each halving, an additional bit is calculated, so, for a 0.6 V signal, in a 1 V scale, the process would be as follows: Halve the initial scale, splitting it in a 0 - 0.5 V range and a 0.5 - 1 V range. Comparing these halves to the analog signal, we realize that the input is in the larger division, thus our Most Significant Bit (MSB) will be 1. On the second iteration, the 0.5 - 1 V scale would be separated into 0.5 - 0.75 V and 0.75 - 1 V ranges, where the signal would be in the smallest of the ranges, thus the second bit would be zero. This processed would be repeated until a suitable resolution is achieved, or the noise overpowers the signal and no more information can be extracted. This is described in the flowchart on Figure 2.6, and a graphical representation of the process can be seen in 2.7 [34].

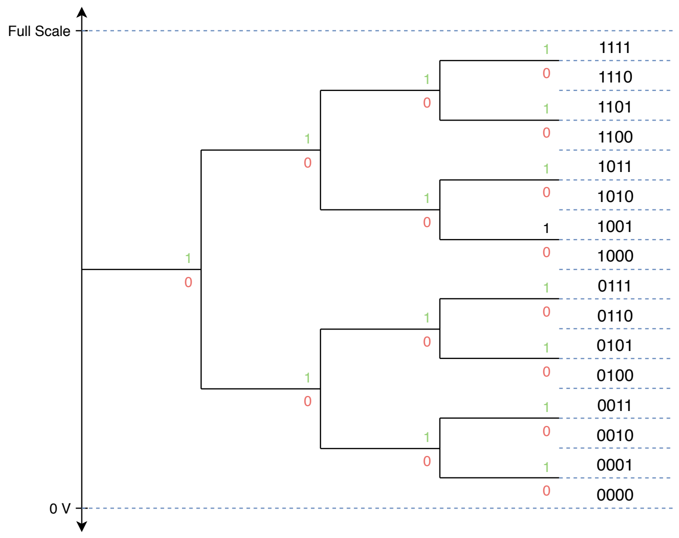

Figure 2.7: Graphical representation of the possible paths in a SAR ADC, adapted from [34].

2.3.4 Delta-Sigma ADC

A Delta-Sigma or Sigma-Delta ADC, used interchangeably in this thesis, are cleverly based around an "oversampling"architecture in order to simplify the input low pass filter, shifting the noise spectrum beyond the passband. This means they can provide very good performance, both in the form of resolution and accuracy.

The "oversampling"characteristic comes from the fact that, unlike standard converters that operate at sampling frequencies close to the Nyquist frequency, the sampling in a $\Delta - \Sigma$ ADC is much higher than Nyquist, enabling a trade between conversion time and resolution, which allows this type of converter to reach very high resolutions when driven with a very high frequency clock [34].

The basic block architecture of the $\Delta - \Sigma$ ADC can be seen in Figure 2.8.

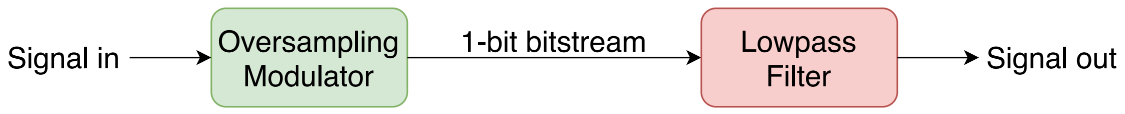

Figure 2.8: Basic architecture of a Delta - Sigma DAC, adapted from [34].

In principle, this seems like a simple concept, however different architectures of oversampling modulator and different types of Lowpass filters severely dictate the performance of the ADC. Because of this, in order to achieve good performance, a high order modulator and good filtering is a must to achieve the necessary resolution for high bit conversion, such as 20 or 24-bits.

2.4 Reconfigurable Hardware

2.4.1 Reconfigurable Digital Systems

The most common type of reconfigurable digital system to find in an IoT Node is a FPGA.

FPGAs offer the capability of designing digital circuits in an Electronic Design Automation (EDA) software and implement them in hardware, through an array of Programmable Logic Block (PLB) (Red blocks in Figure 2.9) linked together through a programmable interconnect network (Green interconnectors in Figure 2.9) to Input/Output (I/O) blocks (Blue blocks in Figure 2.9), which can drastically decrease the development time of a circuit for a specific application.

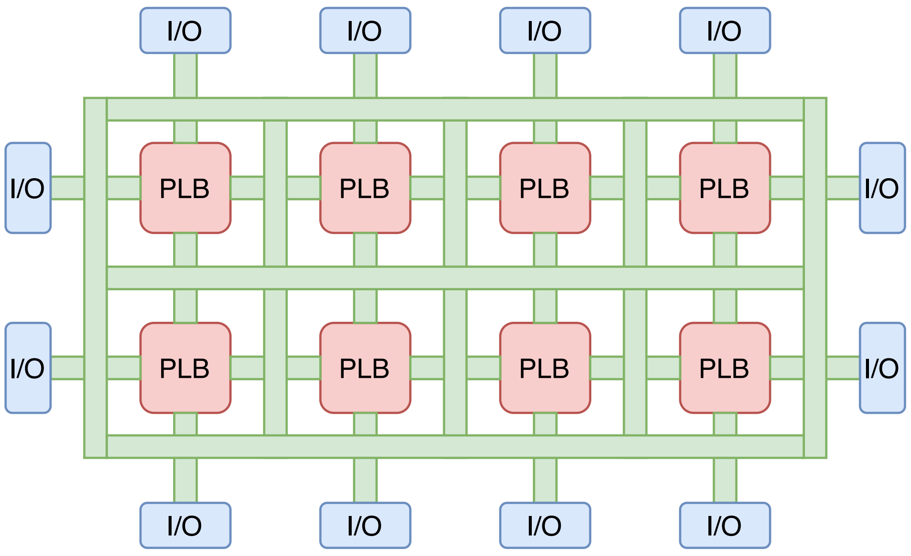

Figure 2.9: Basic architecture of an FPGA, adapted from [35].

However, the trade-off for their programmability in relation to Application Specific Integrated Circuit (ASIC)s is that FPGAs normally have a higher power consumption and occupy a larger silicon area, while at the same time being slower, and even though recent developments have brought the gap between ASICs and FPGAs closer, it still exists [35, 36].

Where FPGAs excel is in tasks where ASICs are uncommon, such as Image Processing or Deep Neural Networks. Compared to a regular microcontroller, an FPGA programmed to run a specific task can improve performance by orders of magnitude [37].

2.4.2 Reconfigurable Analog Systems

The most common type of reconfigurable analog system to find in an IoT Node is a FPAA.

FPAA architectures are varied, but the most basic ones rely on analog components being clustered together, so as to minimize the amount of routing switches used. These clusters are then connected to a Computational Analog Block (CAB) [38, 39].

The routing switches used in an FPAA are usually in a floating-gate configuration, as this improves the linearity of the switch's resistance over the usable voltage range and allows them to function as pure resistors or even current sources. These same floating-gate transistors can be built in a smaller area than their pFET or transmission gate counterparts, which helps with scalability [38, 40, 41].

Each one of the CABs hosts a variety of primitive analog functions such as filters, DACs or matrix multipliers. It is common to find multiple types of CABs in a single FPAA, each designed to implement a specific task, similarly to how a processor implements an Arithmetic Logic Unit (ALU) and and Floating Point Unit (FPU), calling upon them depending on the mathematical operations that have to be realized [42, 43].

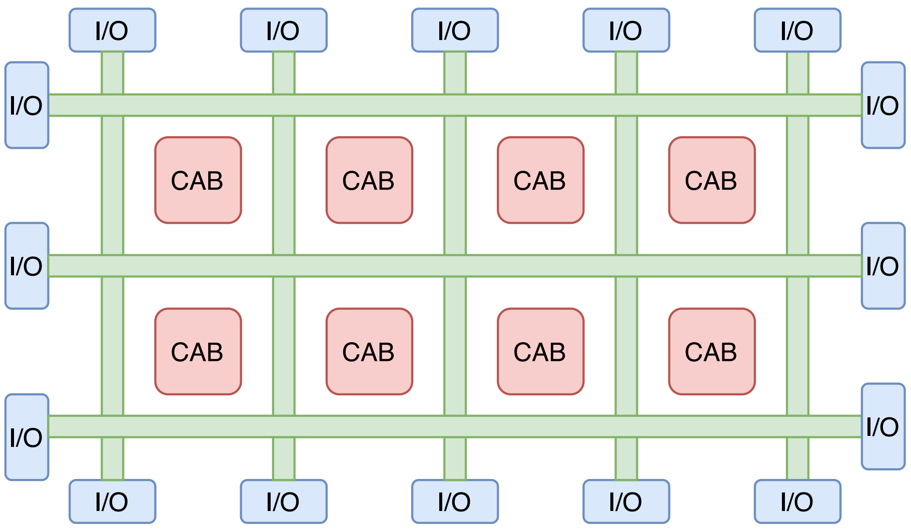

Figure 2.10: Basic architecture of an FPAA, adapted from [41].

Considering this, it's possible to understand that the basic layout of an FPAA will be similar to that of an FPGA, where the PLBs will be replaced with CABs, as can be seen in Figure 2.10.

In Figure 2.10, the Red Blocks represent CABs, the Green interconnectors represent the routing switches, are the Blue Blocks represent the I/O connectors.

2.5 Edge Computing

Edge computing refers to a paradigm of distributed computing, where processing of data is done at the "Edge" of the network, that is, away from a centralized server or cloud node, and closer, or even at, the IoT node itself.

This concept of Edge Computing is becoming increasingly important as the computing capabilities of small, low power IoT nodes grow, enabling a decentralized processing of gathered data.

More advanced implementations of the Edge Computing paradigm can even enable inter-node communication in order to leverage computing resources from other idle nodes in the network to process the data, reducing the amount of bandwidth needed to transmit outside of the local network.

There are, of course, also trade-offs. Some of the main issues come from the decentralization of processing itself, meaning that, with the addition of nodes to the local network, they will not only have to communicate with a central controller, but also amongst themselves, leading to an increase in local network traffic, and added network infrastructure and architecture complexity.

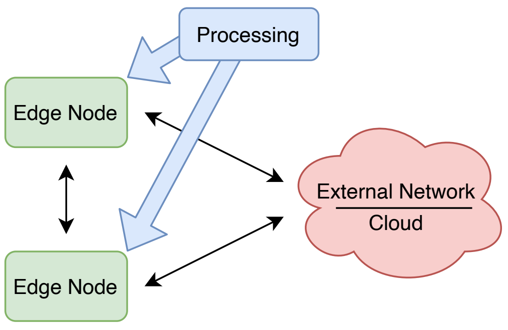

(a) Edge Computing

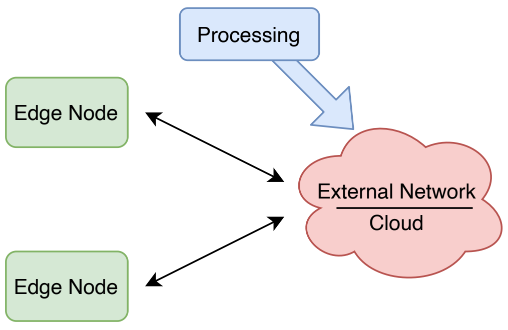

(b) Cloud Computing

Figure 2.11: Edge vs Cloud Computing, adapted from [44].

Instinctively it is also easy to understand that, in the case of a battery or solar powered IoT node, data processing on the device may not be necessarily desired due to the energy penalty that it brings associated with it.

Alternatively, it may also be more energy efficient to process the data locally and transmit the processed data over the network, if this means that the communications module would be active for a smaller amount of time. This is a case by case situation, and must be weighed when designing the IoT Node.

Another obvious trade-off is that, even with many nodes in a network, and the ability to use idle nodes to process certain data, the computing power may not be enough for a specific task, as such Edge Computing alone may not be able to fully fulfill the processing requirements of the IoT system.

Because of this, it becomes apparent that Edge and Cloud Computing must definitely coexist, and the choice of one over the other, or even a combination of both, depends on the specific application at hand [44, 45].

2.6 Concept Work

The objective of this thesis work is to design and develop an advanced IoT Node, for environmental sensing of several physical, chemical and biological parameters through various sensors, with a high level of flexibility and reconfigurability, in order to accommodate the ability to digitize signals from each different sensor, in order to prepare them for digital processing.

To achieve this with a very high level of precision, it is necessary to research, design, implement and test an IoT Node based on a state-of-the-art SoC and Analog Front-End (AFE), which can acquire the sensor signal and use advanced signal processing to extract additional information from the acquired signals.

This, of course, always while holding under consideration the power requirements of the system, as it may be deployed as a battery powered solution.

2.6.1 Design and Architecture

The architecture of the IoT Node is to be based around a PSoC 5LP or PSoC 6 reprogrammable Microcontroller (μC) by Cypress.

Both μC options have their merits. The PSoC 5LP is based on a single Cortex®-M3 core, with a maximum clock speed of 80 MHz, and contains up to two 12-bit SAR ADC and one 20-bit $\Delta - \Sigma$ ADC, 62 General Purpose I/O (GPIO) pins, with no built-in wireless communication options.

However, the PSoC 6 uses a totally different dual-core architecture, based on the combination of a Cortex®-M4 core and a Cortex®-M0+ core, with a clock of up to 150 MHz on the former and 100 MHz on the latter, providing much higher computing power than the PSoC 5LP, however, it has only a single 12-bit SAR ADC, greatly reducing the analog to digital conversion capabilities, on the other hand, it can have up to 102 GPIO pins, allowing for more connected devices, and can also have built-in BLE wireless communication.

Aside from the main microcontroller, the IoT Node can, if necessary, contain a high precision dedicated AFE module. The preliminary candidates are the ADuCM355 and

AD5941 by Analog Devices.

Both of these AFE modules contain high sampling rate 16-bit SAR ADCs, with the ability to measure voltage, current and impedance, as well as having internal and external current and voltage channels, ultralow leakage switch matrix, input Multiplexer (MUX), input buffer and programmable gain amplifier. This means that in the analog input section both these AFE modules are very similar, with the main difference being the digital to analog conversion section, where the ADuCM355 has more capabilities, and in the peripheral communication protocols, where the ADuCM355 can communicate using I_2C, UART and SPI while the AD5941 can only communicate using SPI.

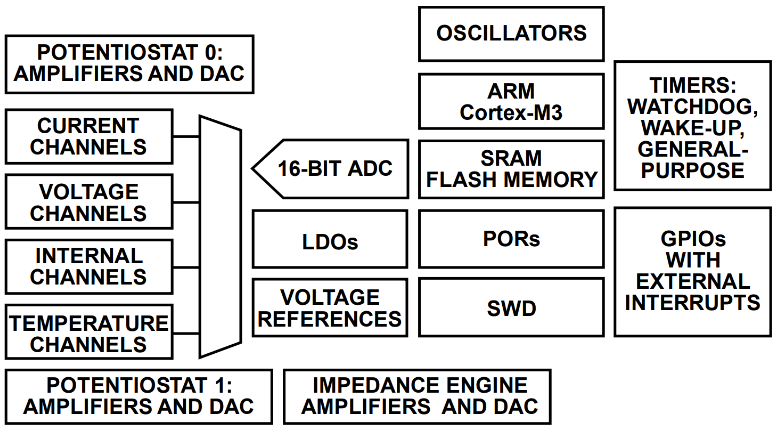
POTENTIOSTAT 0: AMPLIFIERS AND DAC
CURRENT CHANNELS
VOLTAGE CHANNELS
INTERNAL CHANNELS
TEMPERATURE CHANNELS
POTENTIOSTAT 1: AMPLIFIERS AND DAC
IMPEDANCE ENGINE AMPLIFIERS AND DAC
16-BIT ADC
LDOs
VOLTAGE REFERENCES
OSCILLATORS
ARM Cortex-M3
SRAM FLASH MEMORY
PORs
SWD
TIMERS: WATCHDOG, WAKE-UP, GENERAL-PURPOSE
GPIOs WITH EXTERNAL INTERRUPTS

(a) ADuCM355 Simplified Block Diagram

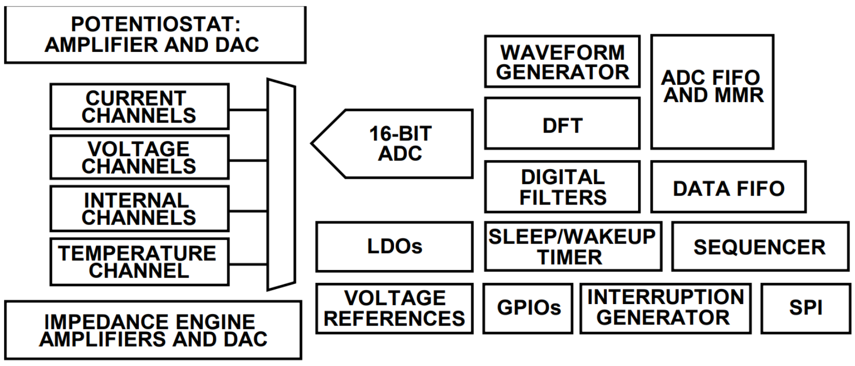

(b) AD5941 Simplified Block Diagram

Figure 2.12: Comparison of the simplified block diagram of the ADuCM355 and the AD5941 Analog Front-End (AFE) modules, obtained from the respective product data sheets, [46] and [47], respectively.

As a way to interface with several sensors, the analog inputs of either the PSoC microcontroller or the AFE module must be multiplexed. Multiplexing allows a single analog input to read multiple independent sensors, one at a time, through the control of the multiplexing device.

The optimal characteristics to look for in a multiplexer are a large number of I/O ports, to allow the interface of as many sensors as possible and a low ON Resistance (R_{ON}), so as to alter the input signal as little as possible. Because of this, the primary multiplexer being considered is the MAX14661 from Maxim [48]. This is a 16 input and 2 output multiplexer, with a typical R_{ON} of 5.5 Ω. When controlled though an I_2C interface, up to 4 of these multiplexers can be used in a system, allowing for up to 32 independent sensors to be connected, when using a 2-wire sensor. However, when controlled through SPI, a virtually infinite number of multiplexers can be used, limited only by the number of available SPI Slave Select pins which can be driven my the microcontroller.

2.6.2 Block Diagram for the Proposed Architecture

Using what we have previously researched in Section 2.1.1 and Section 2.6.1, we can sketch up a preliminary block diagram for the architecture of the proposed IoT Node, with the selected components. This can be seen in Figure 2.13, and contains some details which are yet to be fully defined, such as the use of I_2C or SPI communication to interface with the multiplexers, as well as the number of multiplexers used.

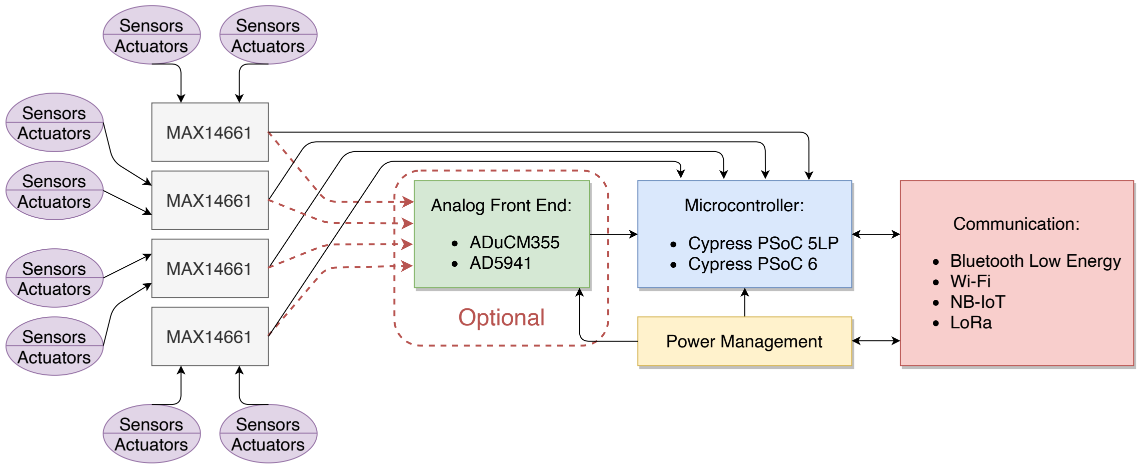

Figure 2.13: Block diagram of the proposed IoT Node.

Here we can see that the proposed IoT Node will allow the connection of a large number of sensors through the cluster of multiplexers. These multiplexers are 16 input, 2 output MAX14661, enabling the ability to connect the sensors to either the AFE or to the PSoC microcontroller directly, which means that the AFE module can be removed when the application doesn't demand a very high precision measurement.

2.6.3 Preliminary Testing

As a proof of concept for the proposed architecture in Section 2.6.2, a similar system was tested in PSoC Creator, the Integrated Design Environment (IDE) Software used to program Cyress' PSoC microcontrollers. The tested system is very simple, and consists of using a MUX with eight analog inputs and one analog output, connected to the $\Delta - \Sigma$ ADC, which is configured for a 16-bit resolution. The signal read by the ADC is then sent to the host computer through a UART Interface. A simple switch on the CY8CKIT-059 PSoC Prototyping Kit, which is being used for this testing, controls the switching of the MUX's channels.

The block diagram of the implemented test system can be seen below, in Figure 2.14, and the code used to control this system can be found in Appendix A.

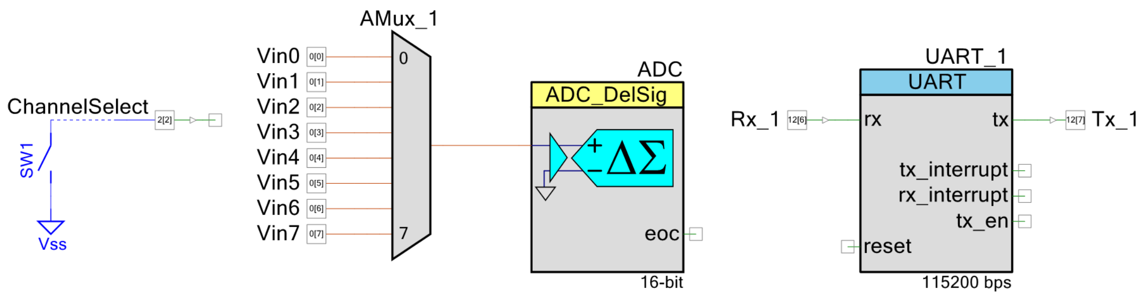

Figure 2.14: System implemented in PSoC Creator for testing.

This basic system tests the operating principles of the underlying proposal for the final work. It uses the $\Delta - \Sigma$ ADC to read signals from eight inputs connected to a MUX, and transmits the readings over a communication interface. The final work will function in a similar fashion, with added complexity, of course, however the success in this test proves that the concept work is sound.

Chapter 3

Board Development

The third chapter of this thesis work deals with the process surrounding the development of the IoT node's Printer Circuit Board (PCB), first from a perspective of hardware development and then from a perspective of software development, given that both components are fundamental to the proper functioning of the noise, and will have to work together in order to achieve the desired result.

Initially there is a description of the steps taken to develop the PCB in KiCad [49], both in terms of the schematic design, as well as the circuit board layout itself, while also including a brief description of finalized component selection and some of the decisions that led to these choices. There is then a explanation of some of the considerations that were had in the design of the PCB with regard to noise isolation and a brief summary of the used ICs and their functions, followed by the experience when assembling all the components on the board.

The software section describes how problems were tackled relating to the software side of the IoT node, starting with the selection of analog sensor channels, then discussing wired data transmission through the USBUART interface and some of the challenges faced when reading sensor data from both the PSoC 5 LP microcontroller as well as the AD5941 AFE, specially as the latter one includes a very extensive library which needed to be ported to the PSoC microcontroller, including some very good examples for the intended use case of this IoT node as well.

3.1 Hardware Development

The primary goal in terms of hardware development is to create a printed circuit board with the components proposed in Section 3.1.1. This PCB must contain all the described components, PSoC microprocessor, wireless communications, High Precision Analog Front End and MAX14661 multiplexers, while providing adequate, clean power to all of them, including some special care in terms of circuit grounding, in an attempt to reduce noise in the sensor measurements.

The PCB was developed in KiCad, a free software suite that facilitates the design of schematics for electronic circuits and their conversion into printed circuit boards, as well as provide a 3D Viewer and the ability to export production oriented documents like Bills of Materials and Gerber files.

Due to the relatively accessible pricing, a 4-layer type of PCB was chosen, this means the circuit board has 4 independent copper layers in which tracks can be laid. This is something that not only helps with layout of the traces and components due to more available space, but also helps with grounding, as one or more of these layers can be used as a dedicated ground plane.

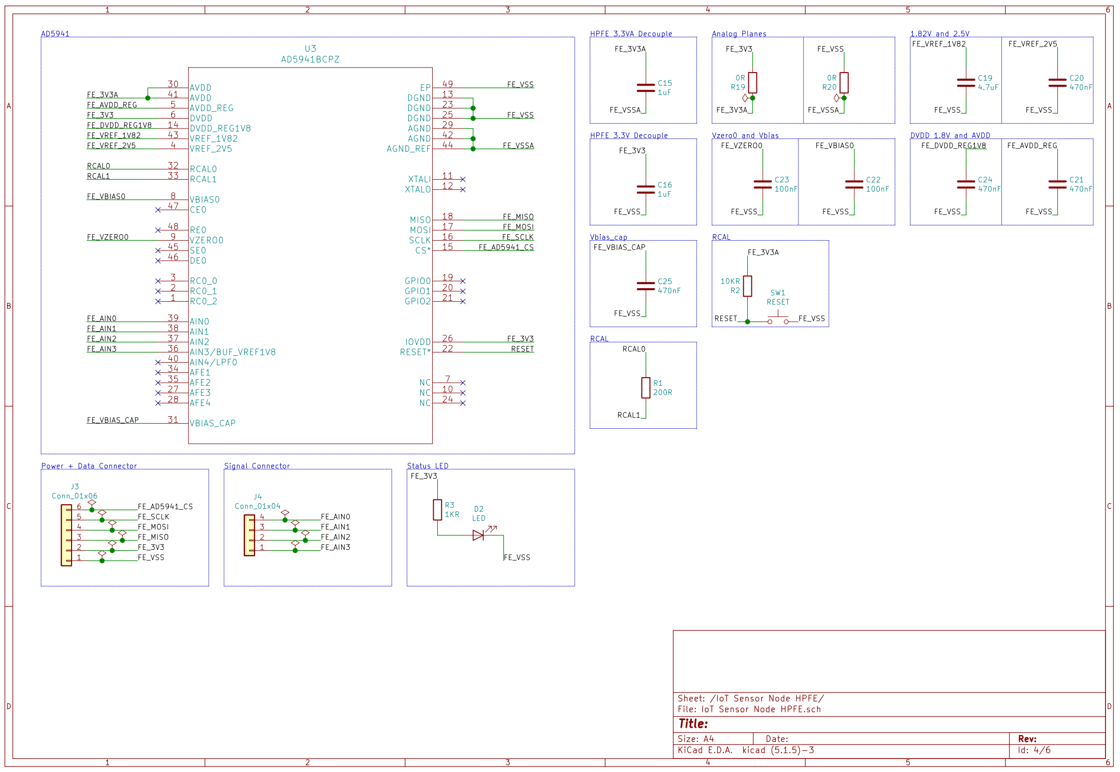

Figure 3.1: High Precision Analog Front End Daughter Board Schematic.

The first step of the PCB development is to create a schematic with the chosen components and make the signal and power connections between them. This consists in having a representation of the inputs and outputs of all the individual ICs and carefully choosing which ports should be connected to which. Using the small AFE daughter board as an example, a circuit schematic looks similar to what is represented in Figure 3.1. The full circuit schematic and board layout for the developed node are available in Appendix B.

3.1.1 Final Component Selection

When it came to the final component selection, the choice for the main microcontroller was to use the PSoC 5LP, for three main reasons:

Firstly, the PSoC 6 microcontroller uses a Ball Grid Array (BGA) style package, making it extremely difficult to solder on the PCB with the available soldering techniques, while the PSoC 5LP uses a relatively simple Quad Flat Package (QFP) with 100 leads.

Secondly, the PSoC 5LP contains an internal 20-bit $\Delta - \Sigma$ ADC and two 12-bit SAR ADC, while the PSoC 6 contains a single 12-bit SAR ADC, meaning that board performance without the external AFE module should be higher with the PSoC 5LP.

Lastly, the QFP package of the PSoC 5LP allows for the separation of digital and analog ground signals, something very important in order to reduce overall analog signal noise, specially due to noise coming from digital interfaces, while the package on the PSoC 6 wouldn't allow such separation.

Another important decision was to use the AD5941 AFE module. This decision was also mostly based on the IC package type, as the ADuCM355 uses the same BGA package as the PSoC 6, which makes it virtually impossible to solder by hand or with conventional reflow methods.

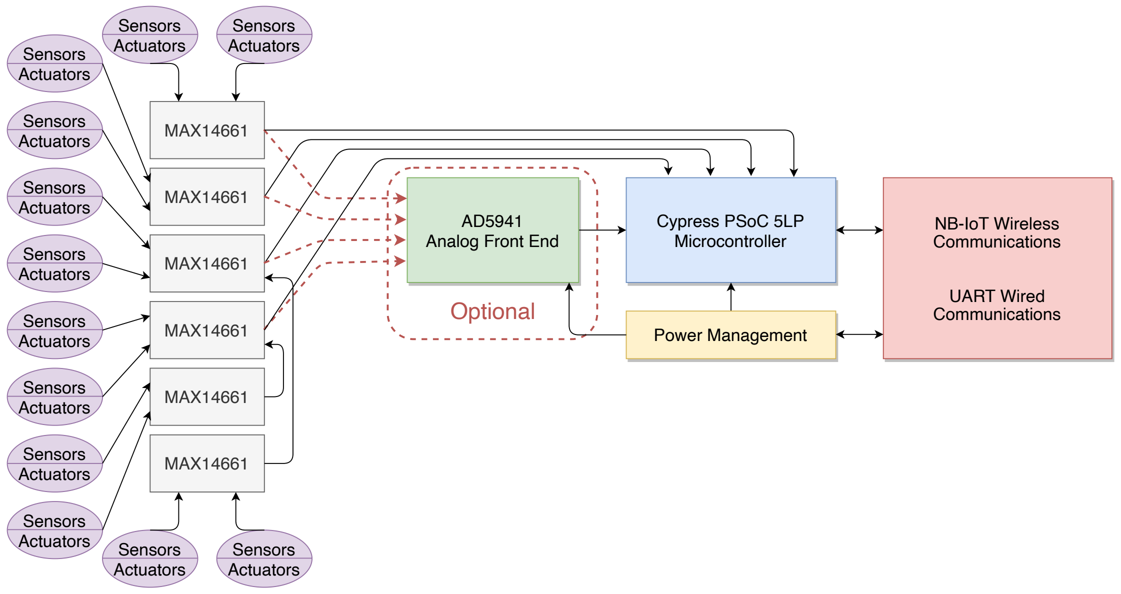
Sensors Actuators
MAX14661
AD5941 Analog Front End
Optional
Cypress PSoC 5LP Microcontroller
Power Management
NB-IoT Wireless Communications
UART Wired Communications

Figure 3.2: Finalized block diagram of the proposed IoT Node.

Wireless communications will make use of NB-IoT technology, as this communication standard appears to provide several advantages over most other considered options, namely in range and power consumption, but compromising on data rate, as can be seen in 2.1. For the actual IC handling NB-IoT, the u-blox SARA-N2 series of NB-IoT modules was chosen due to its relatively affordable price and ready availability.

Wired communications will be assured by a UART interface, running over a USB interface, which assures very high data rate transfers. These two solutions provide a choice between short range wired connectivity with high data rates and long range communication with low data rates.

It was also decided to use six MAX14661 multiplexers, which means the communication with these chips will have to be done via an SPI interface, as only four can be controlled with an I_2C interface, due to only having 4 available I_2C addresses.

These changes mean that the final block diagram of the IoT node will be slightly different from what was originally considered, as is represented in Figure 3.2.

3.1.2 Noise Considerations

One of the most important aspects in the developed PCB is noise isolation. When measuring a sensor at very low voltage levels (in the μV level) like those expected from the sensors, it's of the utmost importance to have a stable, noiseless ground floor. This means some special considerations around good grounding practices, and avoiding ground loops have to be taken.

An important source for this section was [50], according to which there are four main types of signals to consider when designing a PCB:

- **Low Frequency Analog Signals:** In the case of the developed PCB these will be mostly the very low voltage signals (in the level of μV coming from the sensors). These are extremely sensitive signals in terms of return path and should be completely isolated from higher voltage noisy signals, such as digital signals;

- **High Frequency Analog Signals:** The most obvious high frequency analog signals on the IoT node are those in the RF communications section. These signals are in the Volt order of magnitude and can reach multiple GHz in frequency, meaning that they have to be very well isolated from the low frequency analog signals;

- **Digital Signals:** Digital signals are typically multiple Volts in amplitude, high frequency and are especially noisy due to their square nature. These digital signals usually have sharp voltage transitions between levels (with a high slew rate), which creates very high frequency harmonic noise;

- **Powerful Load Signals:** This type of signal is usually associated with high power devices such as motors or actuators and is not present in the IoT node.

Only three of these four types of signals are present in the IoT node, which already slightly simplifies the design process, however, mixing low frequency analog signals with digital and high frequency analog signals still requires careful design considerations around the ground return path and the routing of the low frequency, and low voltage analog signals.

To achieve this, two separate ground planes were created, one for low frequency analog signals (denominated Analog Ground), and one for digital and high frequency ones (denominated Digital Ground). The digital ground plane was then virtually divided in a pure digital section and a high speed analog section for RF signals.

Ultimately, the developed PCB had 2 separate ground planes, and 3 signal regions. At the left is the Radio Frequency section, with the NB-IoT radio, antenna and SIM card slot. In the center is the digital section with the PSoC microcontroller, power supply, wired communications and the AD5941 AFE, and at the far right is the analog section, with the 6 multiplexers and all the analog sensor inputs.

The two ground planes are tied in a star ground configuration, with both planes connected to the power supply ground in a single point, through a 0 Ω resistor. This is the simplest way to isolate ground planes, however if this proves ineffective or insufficient, a high frequency inductive filter such as a ferrite bead can be added.

Equally important to keep sensor noise as low as possible is the analog signal routing. Even the best ground plane separation cannot help if the signals are routed poorly. To achieve the best possible routing, all analog signals were routed only though the section containing the analog ground plane for the trace running from the multiplexers into the PSoC microcontroller and the AD5941 analog front end IC. These traces were also made as wide as possible with the available space, in order to reduce signal loss to trace resistance.

3.1.3 Radio Frequency Section

The radio frequency section is comprised of a u-blox SARA-N2 NB-IoT module. This module provides NB-IoT communications in a relatively small, easy to integrate package which is also priced reasonably, while only needing 3.3 V power, an antenna and a SIM card to operate, but also offering some additional interfaces like UART and I_2C in order to control the sent and received data. This simplifies the integration of the module over others that may need external 1.8 V power, or even external crystals or oscillators, as these components are already integrated into the SARA-N2 module, as can be observed in Figure 3.3.

The NB-IoT communication protocol is specifically designed for IoT applications, in particular those which are battery operated, and thus conscious of energy consumption. This translates to a communication standard which uses an extremely low amount of energy and can communicate over large distances through the cellular network.

The specific variation of the SARA-N2 module used was the SARA-N210, which provides support for NB-IoT Band 20 used throughout Europe, meaning that, as long as there is a cellular signal in the NB-IoT Band 20 and a compatible SIM card is installed, the module should be able to communicate with a host device.

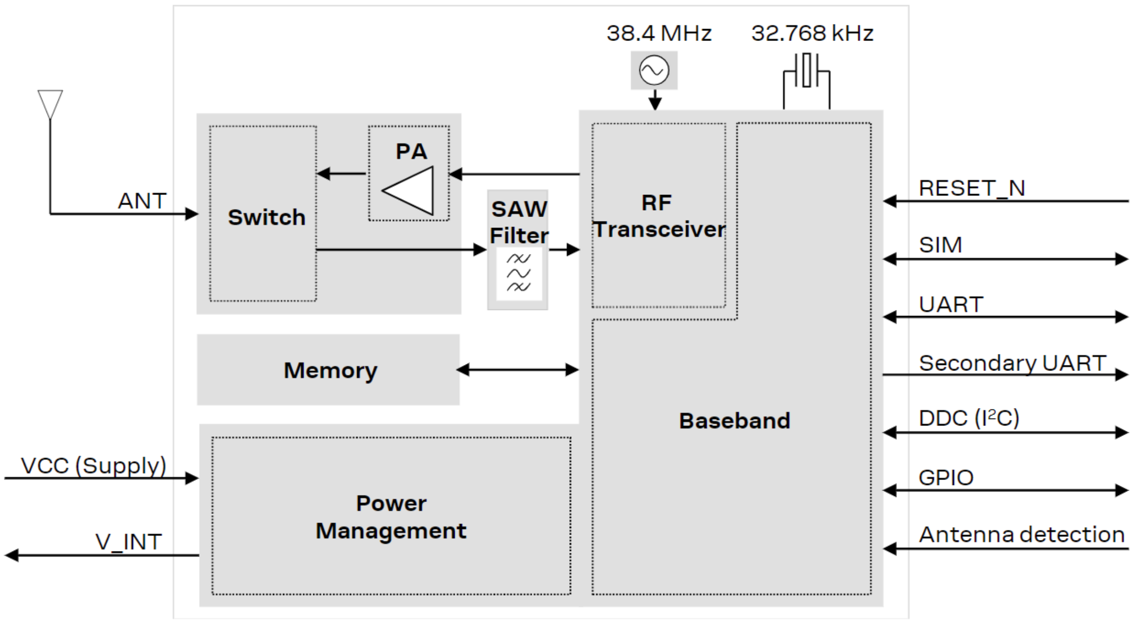

Figure 3.3: SARA-N2 block diagram, obtained from the module's data sheet [51].

Even with the relative ease of integration, some design guidelines have to be taken into consideration. Fortunately, u-blox provides an "Integration Manual" which details some of the steps necessary to a successful integration of the SARA-N2 module.

Module Supply: u-blox recommends that all supply pins must be connected to an external supply in order to minimize power trace impedance, and all ground pins must be connected to a solid ground plane in order to improve RF and thermal performance.

As the module, in our application, is powered via a switching regulator, there are some special considerations to be taken into account, such as ensuring the regulator has enough power capability to support a transmission at maximum power, low output ripple and good decoupling. To achieve this, a network of capacitors of differing sizes will be used between the regulator output and the module input in order to achieve both a good size energy buffer for larger loads, as well as a good transient response for fast peaks.

Antenna Connection: The antenna connection will directly affect RF performance of the module, so it's extremely important to make sure it works as intended.

The first basic requirement is to use a 50 Ω transmission line between the SARA-N2 antenna pin and the antenna connector itself, a 50 Ω connector and an appropriate antenna with optimal radiation performance in the NB-IoT Bands.

In terms of the PCB design itself, a ground keep-out zone is advised, and no digital signals should be routed near the RF connection as these can cause interference. The 50 Ω transmission line should be as short as possible in order to minimize insertion loss, and it should have no stubs or cross with any other signals, so its placement is extremely sensitive.

SIM Interface: SIM Card Interfacing is one of the least sensitive aspects of the PCB design, from an RF perspective, however some mild considerations must still be taken into account to prevent phenomena like RF coupling and electrostatic discharges.

To achieve this, the SIM Card connection lines must have ESD protection, as well as small decoupling capacitors, specially as the SIM Card can be inserted and removed during use. The SIM Card holder will also be placed near the SARA-N2 module just as a general good design practice, in order to keep the data lines as short as possible and board layout tidy.

System Functions: System functions are things such as Power On and Reset signals. These signals must present adequate voltage levels to the SARA-N2 module and not have any sorts of transient noise, which could compromise power up or reset the module during operation.

Other Interfaces: Additional interfaces such as UART and I_2C are essential to the operation of the module, as they provide the data and control connection between the SARA-N2 and the main microcontroller, which needs to receive and transmit information through the NB-IoT wireless network. The SARA-N2 module in particular communicates over UART with a 3.3V logic level, meaning that there is no need to do any sort of voltage conversion as there is with other modules that operate at 1.8V, which the PSoC microcontroller doesn't support.

3.1.4 High Precision Analog Front End

The module which is designated as the High Precision Analog Front End is a small daughter board that can be connected to the main IoT Node and has an AD5941 Analog Front End IC which provides a DAC and ADC with a significantly higher resolution and sample rate, while hopefully having a lower noise level, than those integrated into the PSoC 5 LP microcontroller.

This additional module can be added to the main board when there is need for additional performance, as, while the ADC on the PSoC can have a higher 20-bit resolution, it can only do so at an extremely low sample rate of 187 samples per second, while the ADC on the AD5941 can achieve 16-bit at up to eight hundred thousand samples per second, which is *slightly* higher.

The AD5941 IC: The AD5940 and AD5941 are a small family of ICs which are high precision, low power analog front ends designed for applications that require high precision electrochemical measurement techniques such as voltammetric, amperometric or impedance measurements, specially those around body and skin impedance or toxic gas sensing. A block diagram of the internal components making up the AD5941 can be seen in Figure 3.4

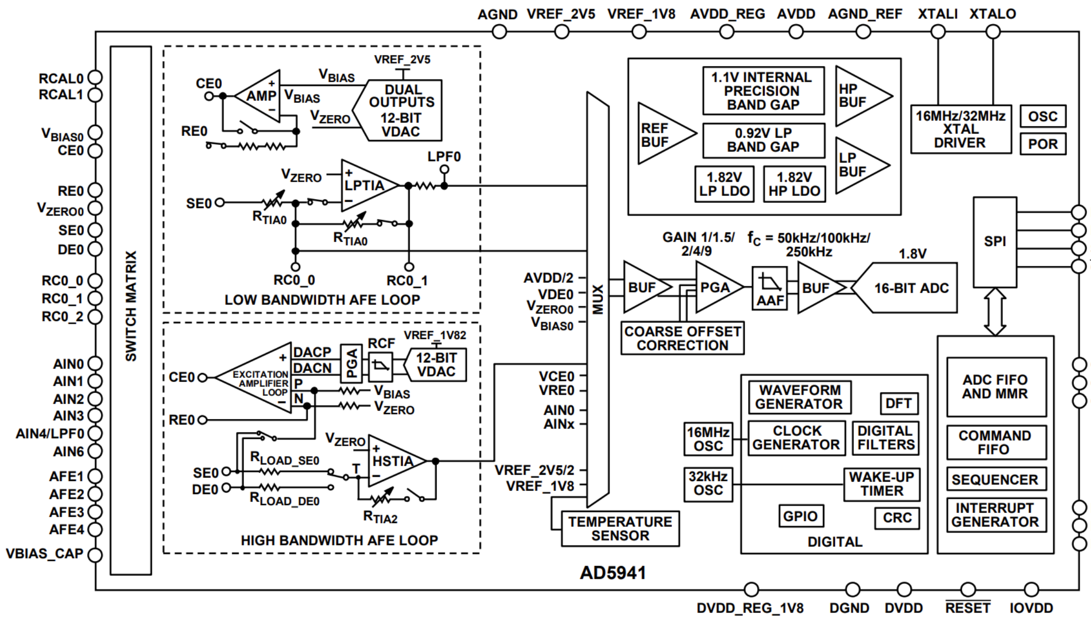

Figure 3.4: AD5941 Block Diagram, obtained from the product's data sheet [47].

These small ICs contain an amazing amount of high precision sensor interfacing capability in a small package, including a high performance, 16-bit resolution ADC with voltage, current and impedance measurement capability, including input buffers and a programmable gain amplifier, two 12-bit DACs, one able to generate signals up to 200 Hz and the other up to 200 kHz, as well as other miscellaneous amplifiers, accelerators and reference voltages. Communication with the AD5941 IC is made via SPI interface, which will also be used to communicate with the channel multiplexers, meaning that all IC communication in the board will be done through the SPI protocol, which theoretically simplifies trace routing. SPI is also a higher speed interface than I_2C, which may be necessary when sampling and transmitting data at up to 800 kSPS.

Daughter Board Design: As with the main board, the smaller daughter board's design had to take into account techniques to reduce overall noise, such as adopting separate analog and digital ground planes, using wide signal tracks to reduce resistive losses, and keeping the analog sensor signals as far away as possible from the high speed digital ones, essentially creating two separate halves on the small PCB. These design techniques can be seen in the final layout for the High Precision Analog Front End, presented in Figure 3.5.

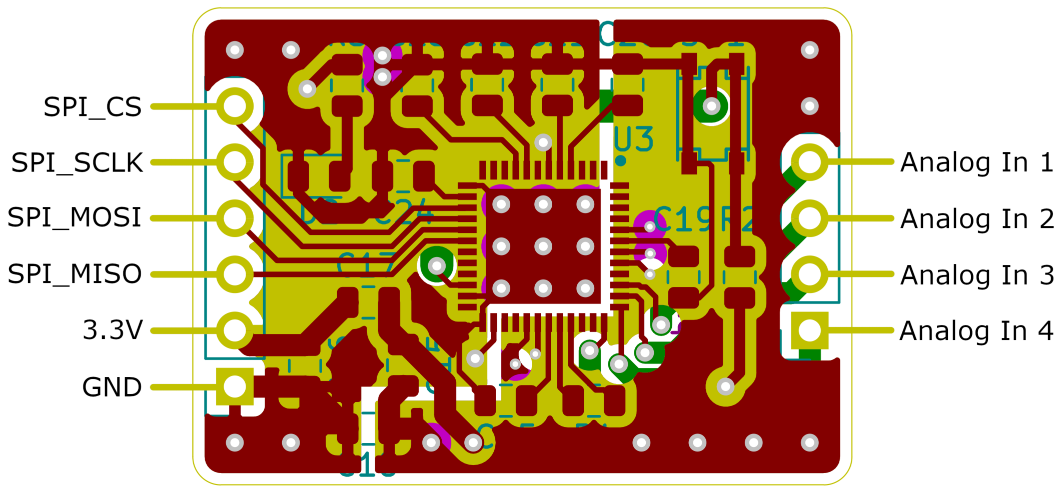

Figure 3.5: High Precision Analog Front End Daughter Board Layout.

3.1.5 Channel Multiplexers

Channel Multiplexing will be be fundamental to the proper working of the node, as both the PSoC microcontroller and the AD5941 AFE provide only 2 pairs of inputs, and thus, without multiplexing, only a maximum of two sensors can be interfaced at any one time. As the intention of the IoT node is to be connected to several sensors at once, the need for signal multiplexing becomes apparently obvious.

Special care has to be taken in the choice of multiplexer to use, as these will be directly in the signal path of very low voltage, and very noise-prone analog signals. It's also important to chose multiplexers that have a high enough input/output ratio, choosing a 2:1 or 4:1 multiplexer is not enough for the intended use.

These facts lead to the choice of the MAX14661 multiplexers by Maxim Integrated.

MAX14661 Multiplexers: The MAX14661 is a dual-channel multiplexer with 16 pins that can be connected to either the common pin or to each other simultaneously in any combination. This provides great connection flexibility as there is no strictly defined input or output. A very wide supply range from 1.6 to 5.5 V once again makes this multiplexer very adaptable, as does the serial control through either SPI or I_2C. However the true selling features when it comes to multiplexing low voltage analog signals are the 5.5 Ω R_{ON} and very low crosstalk between channels.

The serial control is very intuitive, with each individual bit of 2 bytes, per channel, being toggled to control each of the sixteen switches for each of the two channels, meaning that toggling channels open or closed is a simple matter of flipping the corresponding bit.

3.1.6 Board Assembly

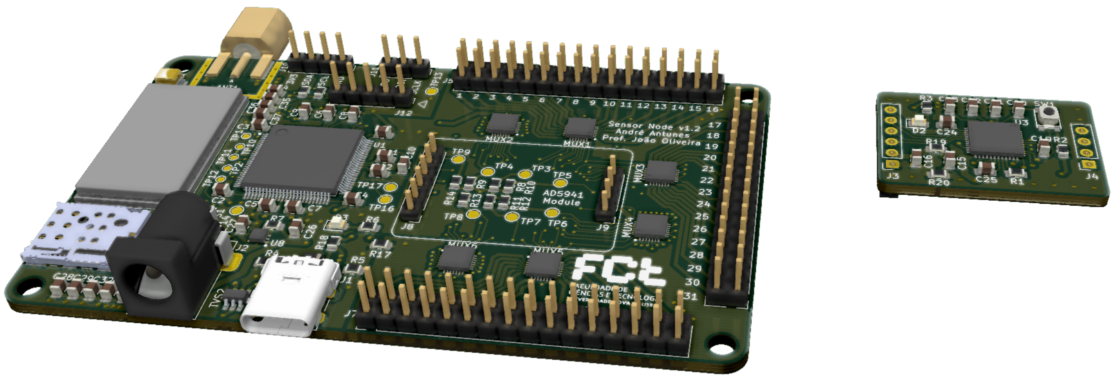

Figure 3.6: 3D Render of the IoT Node's PCB and AD5941 Daughter Board.

The circuit board design itself followed the usual procedures of creating the schematic, assigning footprints to the components, placing them in a layout and laying out traces, with the additional concerns described in Sections 3.1.2 and 3.1.3 being taken into consideration. Not much else can be said about this part of the work other than the full layout being available in Appendix B.

After the whole PCB layout was finished it was looked over to check for mistakes and when none were found, an order for 5 prototypes, as well as an aluminium stencil, was placed. This stencil has cutouts where solder paste should be applied in order to solder the components, and helps immensely with the soldering step of the assembly process.

Some of the chosen components are extremely small, and feature packages such as Quad Flat No-Leads (QFN) which are difficult to solder. With the help of the stencil, a large dose of patience and some surgical hand control, all the components were placed on a prototype PCB for testing. This looked similar to the KiCad render of the PCB in Figure 3.6, with the addition of a few components whose 3D models were unfortunately unavailable.

To solder all the components, a Bismuth based solder paste was used. This type of solder paste has a much lower melting point (~160º C vs ~260º C for regular solder paste) and so it not only reduces the heat on all the components, but is also much easier to touch up if any solder bridges are present. After applying the solder paste with the help of the stencil, the PCB was placed in a reflow oven with a temperature profile appropriate to the solder paste used in order to solder the board.

3.1.7 Power Consumption Considerations

Power consumption in any electronic device merits importance, however, when a device is designed to be mostly battery operated, as is the case with the proposed IoT node, power consumption becomes one of the most important parts of development, as every small efficiency gain translates directly into longer battery life.

While no actual testing was conducted with the proposed node, a fair amount of research was put into gaining a better understanding of the power consumption characteristics of the PSoC 5LP microcontroller, including some power consumption reduction techniques and the working principles of the available low power modes.

Luckily, Cypress provides detailed information into these subjects on Application Note AN77900 [52], including not only extensive documentation about low power modes, but also a spreadsheet which allows the user to estimate the power consumption for a given use case and a PSoC Creator example project implementing some of the described power consumption reduction techniques.

3.1.7.1 Power Modes

The PSoC 5LP has 4 main power modes: Active mode, AltAct mode, Sleep mode and Hibernate mode. These power modes can be split into "active" modes and "low power" modes. The available low power modes differ mainly in power consumption, wake-up time and available wake-up sources, with a lower power consumption obviously leading to a longer wake-up time and less available wake sources.

Active and AltAct modes: These are the main running modes of the PSoC microcontroller, with Active mode being the primary operating mode and AltAct an alternate power configuration for Active mode. AltAct provides a method in which a set of analog or digital blocks can be quickly turned off without the need to toggle each one individually. These are the modes that will be used when the microprocessor is doing any task such as sensor sampling or data transmission.

Sleep mode: Sleep mode is the least severe of the two lower power modes available, with a typical current consumption of 2 μA and a wake-up time of 25 μs, while also providing the largest number of wake-up sources from the two low power modes. Sleep mode can be entered by calling the $CyPmCleep()$ function and the system can be woken up from multiple sources including sleep timers, real-time clock, a button press or an I_2C command, among others.

Hibernate mode: Hibernate mode is the most severe low power mode and reduces current consumption to a measly 300 nA while having a 125 μs wake-up time. Hibernate mode can be entered by calling the *CyPmHibernate*() function and it provides the smallest amount of wake-up sources, being limited only to a button press, an over-temperature event or a reset command.

These low power modes are extremely important in systems that have long pauses between activities, such as the IoT node described in this dissertation, which can be configured to have very long intervals between samples. For example, if the system is configured to sample a sensor for 1 second, send the data, and then repeat the same process a minute later, using the spreadsheet provided by Cypress in [52], the difference between using sleep mode between samples, and running in active mode permanently is a massive 20 to 30x decrease in overall power consumption.

Hibernate mode seems to be too extreme for the intended use, as the only methods of waking the system back are to either physically press a button or to toggle the XRES pin of the PSoC, both of which have to be physically controlled and mean that a person would need to be present at all times to control data sampling, which is completely impractical for the desired application.

There are some more considerations to have when reducing power consumption using low power modes, for instance, by default the PSoC microcontrollers have a "Fast IMO Startup" setting enabled, which starts the IMO with a 48 MHz clock in order to speed up boot time, leading obviously to higher power consumption. Disabling this mode can be useful when the system wakes up from sleep very often, as it reduces power consumption during the wake from sleep phase.

Even so, not every single workload can use these low power modes. If continuous sampling is required, or if PSoC has to be communicating with other devices, sleep mode can't be used, meaning that it's also important to reduce active state power consumption as much as possible.

3.1.7.2 Active Power Consumption Reduction

Reducing active state power consumption can be achieved in some very obvious ways such as powering off unused components or running the microcontroller at a lower clock speed, however, there are also some more obscure ways to achieve this effect and those are the ones that will be explored.

Slowing Down the ADC: The Delta Sigma ADC on the PSoC microcontroller can be configured anywhere from 8 to 20 bits of resolution, as well as a wide range of sampling rates, however all of these factors affect the module's power consumption. According to [52], running the ADC at about half the maximum sample rate, at any resolution, should result in a power consumption of around 0.8 μA, while running the ADC at the maximum sample rate results in about 2.3 μA of power consumption.

Using Slow mode on the Current DAC: The PSoC 5LP has 4 DACs with both a voltage and a current mode. For the drive of resistive sensors, the current mode is normally used and the DACs allow for a "Slow" or "Fast" configuration. This setting basically dictates the slew rate of the current, however, using the fast setting leads to a current consumption which is about 10x higher than when using the slow mode. When driving slowly changing sensors, the slow mode should be used to conserve energy.

Changing Clock Speeds According to Need: As it was stated in the introduction to this section, one of the most obvious ways to reduce power consumption is to reduce the clock speed of the system, however, this may not be possible due to the need for higher clocks when processing data or when using a communications interface such as USB. However, the PSoC microcontroller allows the dynamic change of clocks in code through functions such as $CyIMO\_SetFrequency()$ which means that the clock can be manipulated according to need, being set higher when it needs to be, and much lower when the system is doing more routing tasks such as sampling sensors.

Lowering the Voltage: According to the spreadsheet provided by Cypress to calculate the power consumption of the PSoC microcontrollers, the drawn current doesn't change with the supply voltage, and the PSoC accepts an input from 1.8 to 5 V. By lowering the input voltage and maintaining the current, there is a drop in power consumption directly proportional to the voltage drop.

Additionally there are "Low-Power" modes for several system components such as the external crystal oscillator, GPIO pins, SIO pins, Digital Blocks and VREF Sources. While these don't have a very big impact in overall power consumption, it's important to note that these modes are still available.

3.1.7.3 High Power Consumption Components

From the previously mentioned spreadsheet it's also easy to understand that some components have a severe effect in power consumption, for instance, while the IMO clock can be changed from 3 to 48 MHz while only incurring a 600 μA penalty, doing this same change for the actual CPU clock results in a 20 mA jump to current usage.

Similarly, when using the USB interface, it is important to suspend communications when they are not being used, as simply keeping an open communication line draws 10 mA of current.

3.2 Software Development

As with any project involving a microcontroller, software needs to be developed in order to achieve the designed tasks. This envelops everything from basic things like selecting which internal features of the microcontroller to enable and define which ports are connected, to more complex things like developing libraries to interact with external ICs.

In the case of the chosen PSoC 5 LP microcontroller, this software development is done through the PSoC Creator IDE.

3.2.1 PSoC Creator

PSoC Creator is an integrated development environment designed by Cypress that enables software development, compiling and debugging for the PSoC architecture. The IDE provides a graphical user interface which aids development.

There are essentially 5 main windows which will be used throughout this work.

Top Design: This first window provides an overview of "Components", internal features of the PSoC microcontroller which can be picked from a list and subsequently enabled and configured with the help of a graphical interface. This forms a sort of block diagram of the developed system, where wire connections can be made between the different components, such as connecting pins to ADCs or enabling interrupts and communication interfaces.

This type of programming is extremely beginner friendly and was appreciated in a first contact situation with the PSoC ecosystem.

A screenshot of the "Top Design" page for the developed software architecture can be seen in Figure 3.7

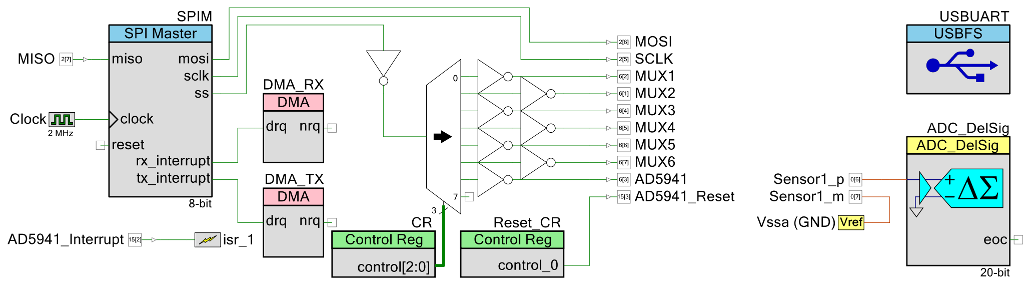

Figure 3.7: Block Diagram on the "Top Design" Window of PSoC Creator.

Pins: The "Pins" window is rather self explanatory. It allows manual definition of where each pin and component defined in the "Top Design" window should be physically connected in the PSoC microcontroller.

This is important because in the PCB design stage of the project, particular pins of the microcontroller were connected to various external ICs, interfaces or analog pins through traces. The graphical interface itself shows a top down view of the specific chosen SKU of PSoC microcontroller, including variations in package type and number of pins, making it easy to personalize the pinout of the PSoC microcontroller for each custom application.

Analog: The "Analog" window allows manual routing of the components and pin connections implemented in the "Top Design" and "Pins" windows.

The need for such a window comes from the fact that the PSoC microcontroller has an internal mesh of routes and switches, which allow an enormous flexibility when connecting devices to the microcontroller, but can become problematic when routing sensitive analog signal through areas where there may be high speed digital signals also present, due to the noise that these digital signals, and their fast slew rates, generate.

Because of this, specially in the developed analog sensor measurement application, special care must be taken when choosing which ports to connect to the DACs and ADCs, as the internal switches have considerable resistance, which can quite severely impact both drive and measurement of analog sensors due to resistive losses. The internal diagram of the PSoC microprocessor as it was used in this application can be seen in Figure C.1, Appendix C and it can be seen that certain ports, such as P0[6], P0[7], P3[1] and P3[0] have a direct connection to the DACs, which reduces losses when driving sensors at higher currents.

Clocks: The "Clocks" window displays an overview of all the internal clocks in the PSoC microcontroller, allowing the user to manually change each of them.

Changing these clocks becomes necessary when using the USBUART module described in Section 3.2.3, as this module needs a 48 MHz clock in order to comply with the USB specification. The 48 MHz clock is not usually active in the PSoC by default, as it's achieved via 2x multiplication from the main internal oscillator, which is usually run at 3 MHz, but needs to be run at 24 MHz specifically, as only this specific clock frequency has a good enough precision to satisfy the needs of the USBUART interface.

Main: "Main" is not a window per se. It's the name of the C programming file used. This window shows the "main.c" file, where the main "hard" code is written. Even with the very good graphical helping tools, the actual programming for the PSoC microcontroller is done through normal programming in C language.

This includes the enabling of all the components placed in the "Top Design" window, as well as coding all the logic that will run on the microcontroller.

The "main.c" file, in this case, is also accompanied by the "ad5940.c" and "ad5940.h" files, whose use will be described in depth in Section 3.2.4.2, as these files implement the interface library with the AD5941 AFE IC.

3.2.2 Analog Channel Selection

To select which analog signal to measure, an SPI command has to be sent to the multiplexers instructing them to enable the specific sensor port to open, and whether to route it to the PSoC microcontroller or the AD5941 AFE.

In the hardware design, the common port A of multiplexers 1, 2, 3 and 4 were connected directly to the PSoC microcontroller in ports P0[6], P0[7], P3[1] and P3[0] as these have a direct connection to the sensor driving DACs. The common port A of multiplexers 5 and 6 were left unconnected, leaving only common port B of each of these connected to port 16 of multiplexers 4 and 3, respectively. Common port B of multiplexers 1 through 4 were connected directly to the input ports of the AD5941 AFE.

This meant that, to simply connect to a specific sensor port, specially those in multiplexers 5 and 6, some juggling of the open ports had to be done, as for instance, a port connected to multiplexer 5 has to then travel to multiplexer 4 and only then to the PSoC microcontroller or the AD5941 AFE.

The MAX14661 multiplexers are controlled either through I_2C or SPI, however in I_2C mode they are limited to four separate addresses, meaning that a maximum of four multiplexers can be used, which is why the developed board uses SPI to communicate with these multiplexers. Port open and close is controlled through a series of four byte long registers. In the developed analog channel selection function, each of these four bytes is declared as a variable, with one set of four variables per pair of multiplexers, as these will be controlled in pairs due to the minimum two-wire connection to sensors.

In total the PCB will have 47 analog channels, sixteen from each pair of multiplexers, minus one from multiplexers 3 and 4 which serves as pass-through for multiplexers 5 and 6.

The function developed for easy control of channel opening and closing works through a very simple principle, it takes three input variables: channel; output; state. Channel corresponds to what analog channel is being addressed, output refers to the common pin A or B, one connected to the PSoC, the other to the AD5941 and finally state indicates if the intended action is to open or close the specific channel. There are 12 integer variables which correspond to each of the bytes on the three pairs of multiplexers, when an open command is called, the corresponding byte in these variables is changed and is transmitted through SPI to the corresponding multiplexer. The same happens when a close command is given.

3.2.3 USBUART Transmit and Receive

UART is the main wired communication method used. The PSoC microcontroller offers two distinct methods of implementing UART interfaces, the first one is as a standalone interface, with the usual TX and RX lines, which will then connect to any other

UART device. The second method is through a USBUART, that is, a UART interface running through the USB communication protocol. The PSoC Creator IDE has a template for the USBFS (USB Full Speed) interface with all the descriptors implemented in order to enumerate a simple serial port device. This second method is the one that will be used, as the node is already powered via USB from a computer, and to transmit the UART data to USB manually, an additional UART to USB converter IC would be needed, which would add additional unnecessary complexity.

Two UART related functions were developed, one of them is a simple initialization which configures the USBUART device with the setting of an incoming connection, making it possible for the connected computer to use any Baud Rate, Parity or Polarity settings and the PSoC will adapt to the settings used. The second one is a "bounce back" function which simply reads what the connected computer wrote in the serial port and returns it. This was done as a way to test two way communication functionality, even tho only one way communication, from the PSoC to the serial port, was then used. A function for the actual data transmission wasn't developed, as there is already a function of the USBUART module which implements the transmission of a string in a single command, after the initialization process is done, making an extra function for this situation unnecessary.

3.2.4 Sensor Data Acquisition

As the ultimate purpose of the developed IoT node is to measure sensor data, this is probably the most important part of the software development. Sensor data can be acquired from two separate sources, either from the internal ADC on the PSoC microcontroller or from the external AD5941 AFE.

3.2.4.1 Sensor Data Acquisition from PSoC

The PSoC microcontroller has two types of internal ADC. The first type is a 12-bit resolution, SAR ADC with an extremely fast sample rate of 1 million samples per second. The advantage of this type of ADC is obvious, it has an extremely fast sample rate, which is fundamental for fast changing signals, however it also has a relatively limited 12-bit resolution which is not the perfect fit for high precision measurements. The second type of internal ADC is a 20-bit resolution Delta Sigma converter, which, at full 20-bit resolution has a sampling rate up to 187 samples per second, a far cry away from the 1 million samples of the SAR ADC.

For the intended application, however, the $\Delta - \Sigma$ ADC is clearly better suited, as there can be a trade-off between sampling rate and resolution, whose optimal point will be searched for in Section 4.2.

A large part of the software configuration of the $\Delta - \Sigma$ ADC is done through the "Top Design" component, with an easy to use graphical interface that allows the user to selecting things like Conversion Mode, Resolution, Conversion rate, Single Ended or

Differential modes, Reference voltage and Input Range. This configuration window is shown in Figure 3.8.

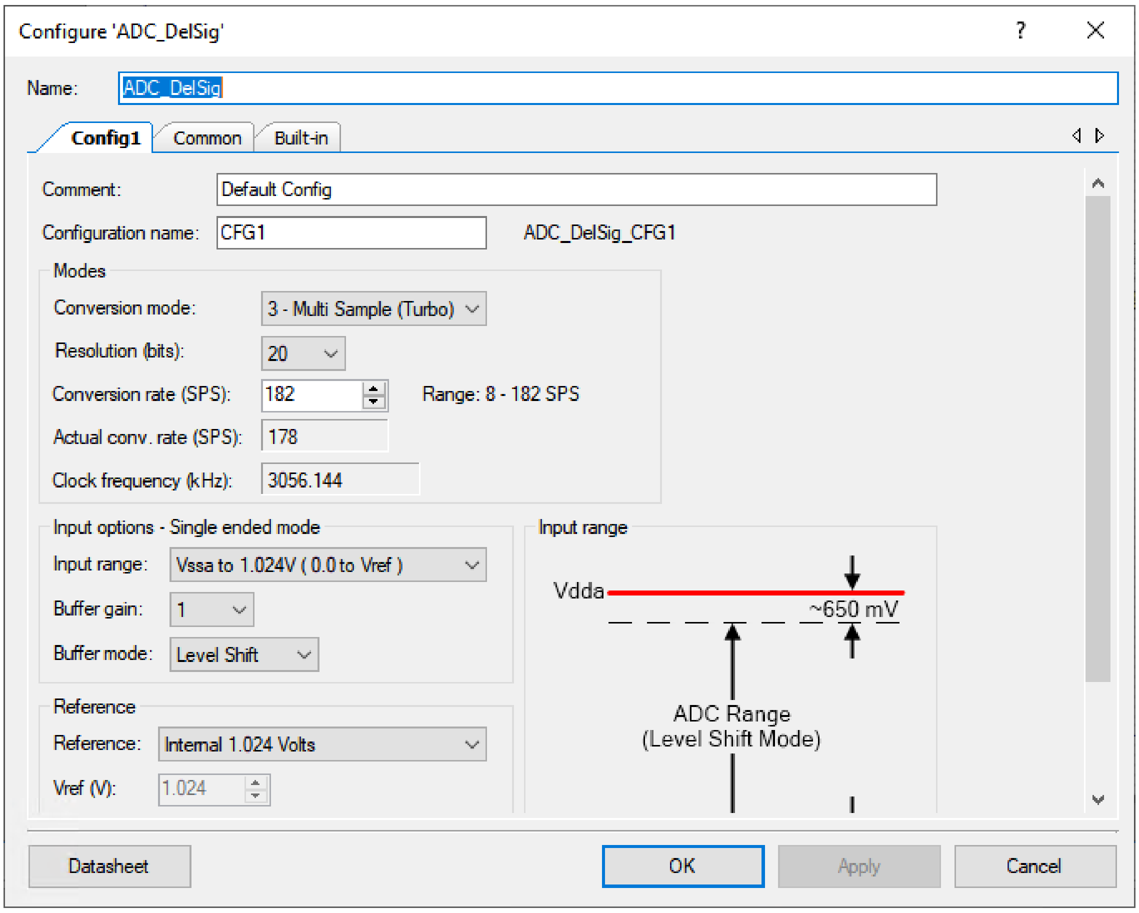
Configure 'ADC_DelSig'

Name: ADC_DelSig

Config1 | Common | Built-in

Comment: Default Config

Configuration name: CFG1 ADC_DelSig_CFG1

Modes

Conversion mode: 3 - Multi Sample (Turbo)

Resolution (bits): 20

Conversion rate (SPS): 182 Range: 8 - 182 SPS

Actual conv. rate (SPS): 178

Clock frequency (kHz): 3056.144

Input options - Single ended mode

Input range: Vssa to 1.024V (0.0 to Vref)

Buffer gain: 1

Buffer mode: Level Shift

Reference

Reference: Internal 1.024 Volts

Vref (V): 1.024

Figure 3.8: Configuration Page of the Delta-Sigma ADC in PSoC Creator.

As far as actual programming is concerned, very little has to be done apart from enabling the module through a single line of code and starting and stopping the conversion when desired. Additionally, the PSoC Creator IDE makes available to the user preconfigured functions which convert the ADC's output code directly into volts, millivolts or microvolts, which makes measurements extremely convenient.

3.2.4.2 Sensor Data Acquisition from AD5941

Communication with the AD5941 Analog Front End IC is made through an SPI connection. This IC has an extremely extensive feature set and very powerful capabilities, looking at the datasheet of these devices, we can attest that they have over 180 control registers, which means that developing a library to control all their functionality every time someone had the intention to integrate it into a custom design would be quite complicated. Exactly because of this, Analog Devices provides an extensive firmware library for the AD5940, AD5941 and ADuCM355 ICs. These are state-of-the-art SoC for electrochemical and biosensors, exactly the use case of the developed IoT node.

Porting this library is also made very simple by Analog Devices, as only six functions have to be implemented: CS Set, CS Clear, RESET Set, RESET Clear, Delay 10 μs) and SPI Read/Write N Bytes. Even tho they are simple, they present an issue, as the RESET pin of the AD5941 is a push button control, luckily this function is only used as a hardware reset of the AD5941 before the library is started, to ensure that the AD5941 is in a default state when communication starts, which shouldn't be an issue if the library is loaded right after the IoT node is powered up. For a future version of the IoT node, however, AD5941 RESET functionality should be implemented.

Another peculiarity of the PSoC microcontroller is that it doesn't allow manual control of the CS pin, this is instead done automatically by the SPI Transmit and Receive functions, however the control of CS pin implemented by these functions matches what is done in the AD5941 library, so this shouldn't present an issue either.

To help guide the user of the AD5941, Analog Devices also provides an extensive repository of example code for specific types of sensor measurement such as Amperometric, Impedance, Body Impedance, Temperature, etc. As well as some examples of sensor polarization techniques such as square wave voltammetry. All in all, both the library and the example files are extremely powerful in helping the user of the AD5941 get familiar with the device.

In these examples, there is also an SPI Debug function which tests the SPI Writes and Reads to the AD5941 which will be used in Chapter 4.4.

Chapter 4

Board Testing

As with any sort of work, and especially development work, proper testing has to be done in order to ensure the correct working order of all the different components, be they hardware or software.

To that extent, several functional blocks of the developed PCB will be tested, starting with the six MAX14661 Multiplexers, then moving on to the PSoC's internal $\Delta - \Sigma$ ADC, which also includes the PSoC's internal current DAC, used to drive the device under test.

Finally, there is a small section about the tests made to the AD5941 AFE IC.

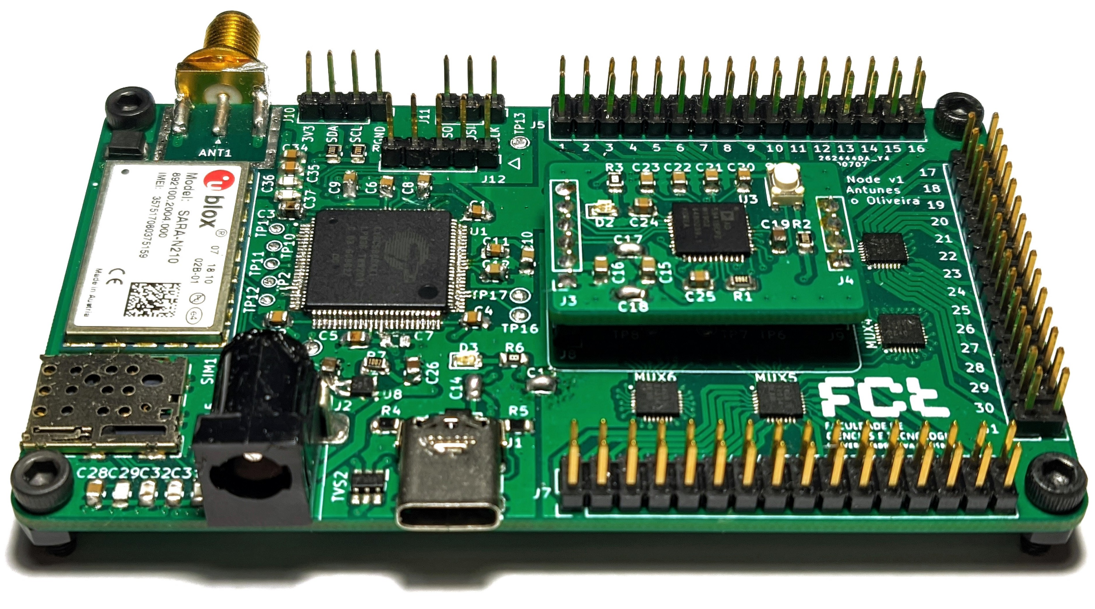

Figure 4.1: Picture of the assembled IoT Node and AD5941 Daughter Board.

Figure 4.1 shows a picture of the fully assembled circuit board in working order. This is the prototype board where all tests were made, with the AD5941 Daughter Board placed in its respective location between the six multiplexers.

4.1 Testing of the Multiplexers

The developed PCB contains six individual MUXs. All six are the MAX14661 IC, with sixteen input and two output channels. They work by connecting each of the sixteen input channels to either of the two output channels through very low impedance switches, nominally 5.5 Ω. The internal switch layout of these multiplexers can be seen in Figure 4.2

This configuration provides immense versatility as it enables multiple input channels to be connected to each other, multiple input channels to be connected to a single output channel or even both output channels to be connected to one another. This interconnecting ability is used in MUXs 5 and 6, which are connected to MUXs 3 and 4, which are themselves then connected to the PSoC μC or to the AD5941 AFE.

In order to test the MAX14661 MUXs' channel selection software, all the switches on every single MUX were commanded to open, and the SPI data was recorded on a Logic Analyzer.

This data was analyzed channel by channel, and when it was confirmed to be working as expected, the hardware side of the multiplexers was tested, by using a multimeter in continuity mode.

The theoretical principle behind this test is that, as all the switches were open, this means that all channels would read continuity between them if they were functioning properly. All six MUXs passed this test with flying colors.

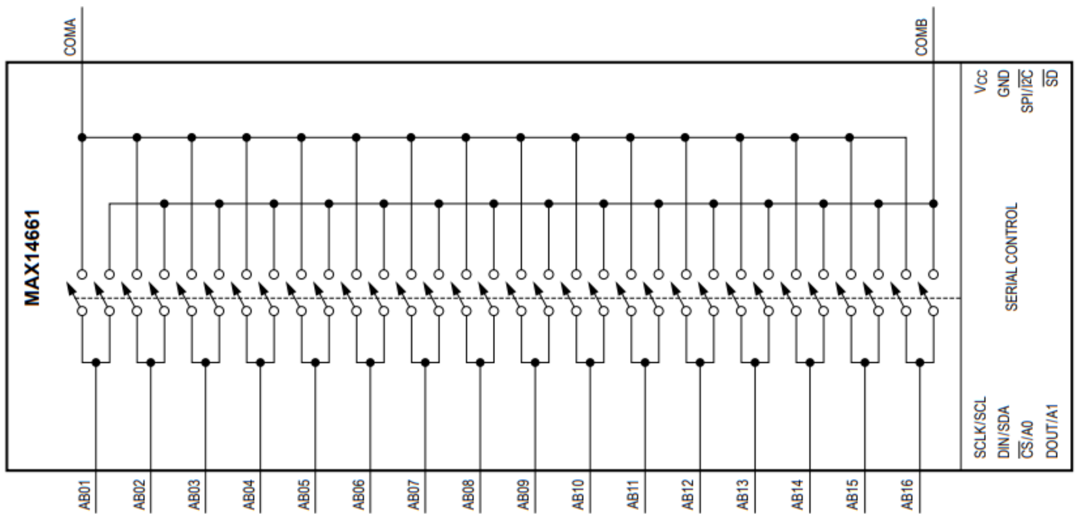

Figure 4.2: Internal Configuration of the MAX14661 Multiplexers.

4.2 Testing the Internal Delta-Sigma ADC with Low Value Resistors

Testing the PSoC's internal $\Delta - \Sigma$ ADC will be more difficult than the simple testing done with the MUXs, as the ADC features many settings which can greatly affect the output result.

In this testing we are looking at obtaining high accuracy measurements with the lowest possible noise while keeping a reasonable sample rate. Unfortunately, as with all things a trade-off has to be made between accuracy and sample rate. Higher resolution modes result in a higher measurement accuracy and lower noise, however that also means a lower sample rate, which may become a problem with fast changing signals or impact the ability to apply certain filters.

Four different resolutions will be tested: 20, 18, 16 and 14 Bits. For each of these resolutions there will be two test settings, one with a unitary input buffer gain, and one with a buffer gain of 2. This brings the total to 8 test configurations. All tests will be made in "Multi Sample (Turbo)" mode, with a 0 to VREF scale. This mode provides a higher sample rate than the regular "Multi Sample" mode, although not quite reaching the rate of "Continuous" mode.

For each configuration there are two main things to look at: measured value accuracy and measurement noise.

The measured value will be represented by a bar graph with a 95% Confidence Interval (CI) error bar. Each resolution and buffer gain combination will test three different sensor polarization currents (1, 10 and 100 μA) and three different resistor values: 22 Ω (measured with a multimeter as 21.7 Ω), 470 Ω (measured as 465 Ω) and finally 1 kΩ (measured as 992 Ω).

The measurement noise will be displayed in table form for all the same scenarios, three currents and three resistances, and the noise will be displayed in four different forms:

- Peak to Peak Noise: Simple peak to peak determined by subtracting the lowest measured value from the highest one.
- 99.7% Noise: Equivalent to 6σ or 6 standard deviations, the measured values closely follow a normal distribution, thus a mean and standard deviation can be calculates.
- Root Mean Square (RMS) Noise: Equivalent to a single standard deviation, as we can assume that the mean noise value is zero.
- RMS Noise (LSB): Regular RMS noise given as a function of least significant bits.

Graphs were generated by exporting the measured ADC value, already converted to μV, through a UART interface running on USB. For each test, 5000 to 20000 measurements were made. This data was then processed with a MATLAB script available in Appendix D, noise values were calculated, and the shown graphs were plotted.

4.2.1 20-Bit Mode

Starting with the highest resolution mode available in the $\Delta - \Sigma$ ADC, 20-bit.

20-Bit, Buffer Gain = 2: The first test with a buffer gain of 2 and a sample rate of 92 samples per second exemplifies the most extreme end of the accuracy - sample rate spectrum and represents a Least Significant Bit (LSB) value of 0.5 μA. Measurement accuracy data is presented in Figure 4.3.

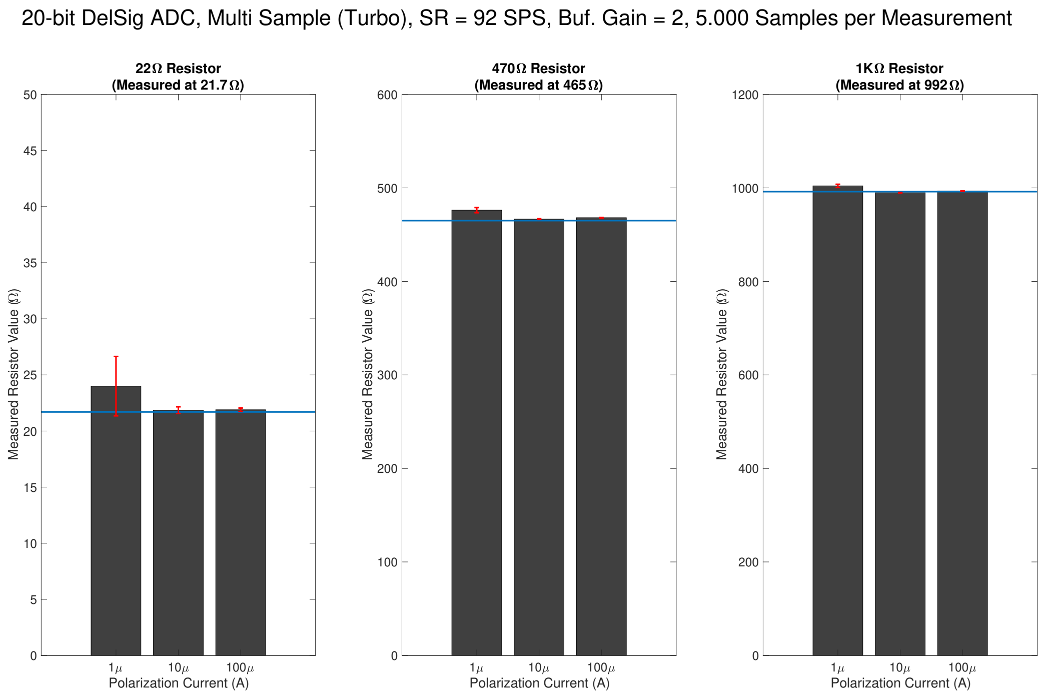

Figure 4.3: Results of measurements using 20-bit $\Delta - \Sigma$, Multi Sample (Turbo), SR = 92 SPS, Buf. Gain = 2, 5.000 Samples per Measurement.

For these test parameters, measurement noise data is shown below, in Table 4.1, using the four metrics described in Section 4.2.

Table 4.1: Noise values of measurements using 20-bit $\Delta - \Sigma$, Multi Sample (Turbo), SR = 92 SPS, Buf. Gain = 2, 5.000 Samples per Measurement.

Pol. Current (μA)		**1**			**10**			**100**	
Resistor Value(Ω)	22	465	992	22	465	992	22	465	992
Noise pk-pk (μV)	9	9	11	10	14	17	55	106	140
Noise 99.7% (μV)	7.94	8.27	10.2	9.0	11.8	14.3	46.2	85.0	108
RMS Noise (μV)	1.32	1.38	1.70	1.50	1.96	2.37	7.71	14.2	18.0
RMS Noise (LSB)	2.71	2.82	3.49	3.08	4.02	4.86	15.8	29.0	36.8

20-Bit, Buffer Gain = 1: The second test was conducted with a unitary buffer gain a sample rate of 182 samples per second, with an LSB of 1 μA. Measurement accuracy data is presented in Figure 4.4.

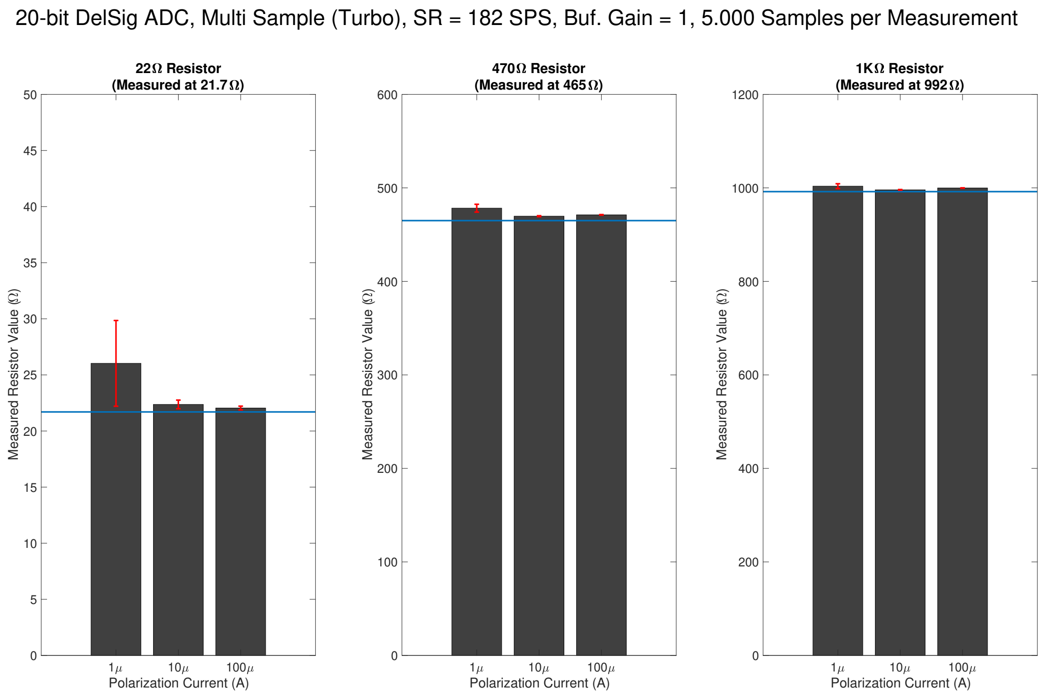

Figure 4.4: Results of measurements using 20-bit $\Delta - \Sigma$, Multi Sample (Turbo), SR = 182 SPS, Buf. Gain = 1, 5.000 Samples per Measurement.

For these test parameters, measurement noise data is shown below, in Table 4.2, using the four metrics described in Section 4.2.

Table 4.2: Noise values of measurements using 20-bit $\Delta - \Sigma$, Multi Sample (Turbo), SR = 182 SPS, Buf. Gain = 1, 5.000 Samples per Measurement.

Pol. Current (μA)		**1**			**10**			**100**	
Resistor Value(Ω)	22	465	992	22	465	992	22	465	992
Noise pk-pk (μV)	14	14	15	13	17	21	59	95	141
Noise 99.7% (μV)	11.5	12.5	15.7	11.6	15.5	20.0	49.6	83.1	120
RMS Noise (μV)	1.91	2.09	2.62	1.93	2.58	3.33	8.26	13.9	19.9
RMS Noise (LSB)	1.96	2.14	2.69	1.97	2.64	3.41	8.46	14.2	20.4

4.2.2 18-Bit Mode

Stepping down 2 bits of resolution, this series of tests was done at 18 bits.

18-Bit, Buffer Gain = 2: This third test shows a buffer gain of 2 and 1238 samples per second, resulting in 2 μA of LSB. Measurement accuracy data is presented in Figure 4.5.

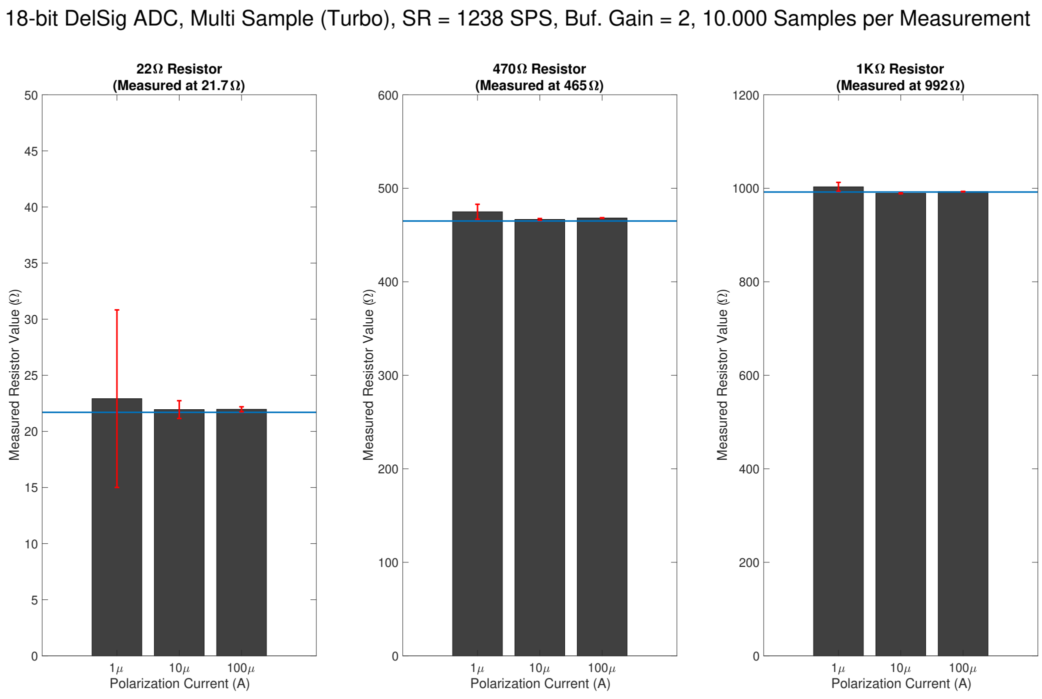

Figure 4.5: Results of measurements using 18-bit $\Delta - \Sigma$, Multi Sample (Turbo), SR = 1238 SPS, Buf. Gain = 2, 10.000 Samples per Measurement.

For these test parameters, measurement noise data is shown below, in Table 4.3, using the four metrics described in Section 4.2.

Table 4.3: Noise values of measurements using 18-bit $\Delta - \Sigma$, Multi Sample (Turbo), SR = 1238 SPS, Buf. Gain = 2, 10.000 Samples per Measurement.

Pol. Current (μA)		**1**			**10**			**100**	
Resistor Value(Ω)	22	465	992	22	465	992	22	465	992
Noise pk-pk (μV)	29	31	37	31	37	43	80	121	177
Noise 99.7% (μV)	23.7	24.0	28.2	23.7	28.7	31.3	67.2	96.5	151
RMS Noise (μV)	3.96	3.99	4.71	3.95	4.78	5.22	11.2	16.1	25.1
RMS Noise (LSB)	2.03	2.05	2.41	2.02	2.45	2.67	5.74	8.23	12.9

18-Bit, Buffer Gain = 1: The fourth test was configured with a buffer gain of 1 and 2477 samples per second, which corresponds to an LSB of 4 μA. Measurement accuracy data is presented in Figure 4.6.

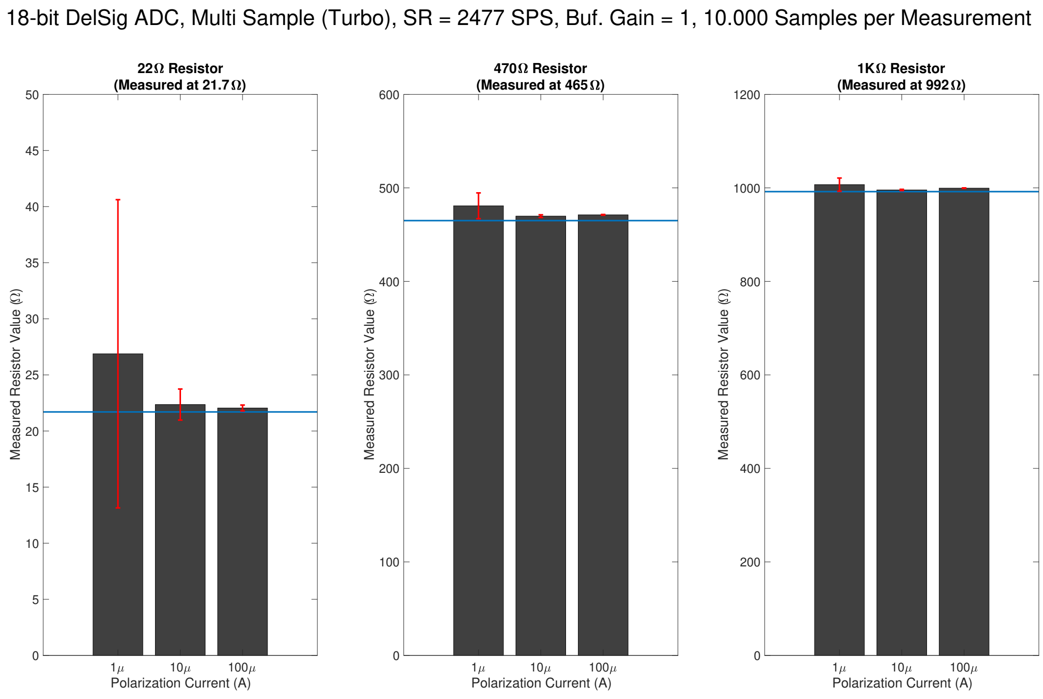

Figure 4.6: Results of measurements using 18-bit $\Delta - \Sigma$, Multi Sample (Turbo), SR = 2477 SPS, Buf. Gain = 1, 10.000 Samples per Measurement.

For these test parameters, measurement noise data is shown below, in Table 4.4, using the four metrics described in Section 4.2.

Table 4.4: Noise values of measurements using 18-bit $\Delta - \Sigma$, Multi Sample (Turbo), SR = 2477 SPS, Buf. Gain = 1, 10.000 Samples per Measurement.

Pol. Current (μA)		**1**			**10**			**100**	
Resistor Value(Ω)	22	465	992	22	465	992	22	465	992
Noise pk-pk (μV)	54	59	55	51	59	51	93	141	203
Noise 99.7% (μV)	41.2	41.4	42.2	41.5	43.1	43.3	78.7	117	170
RMS Noise (μV)	6.87	6.90	7.04	6.92	7.18	7.20	13.1	19.5	28.4
RMS Noise (LSB)	1.76	1.77	1.80	1.77	1.84	1.84	3.36	5.00	7.26

4.2.3 16-Bit Mode

Stepping down another 2 bits from the previous series of tests, this series was done at a 16 bit resolution. Measurement accuracy data is presented in Figure 4.7.

16-Bit, Buffer Gain = 2: The fifth test had a buffer gain of 2 and 5505 samples per second, resulting in 8 μA of LSB.

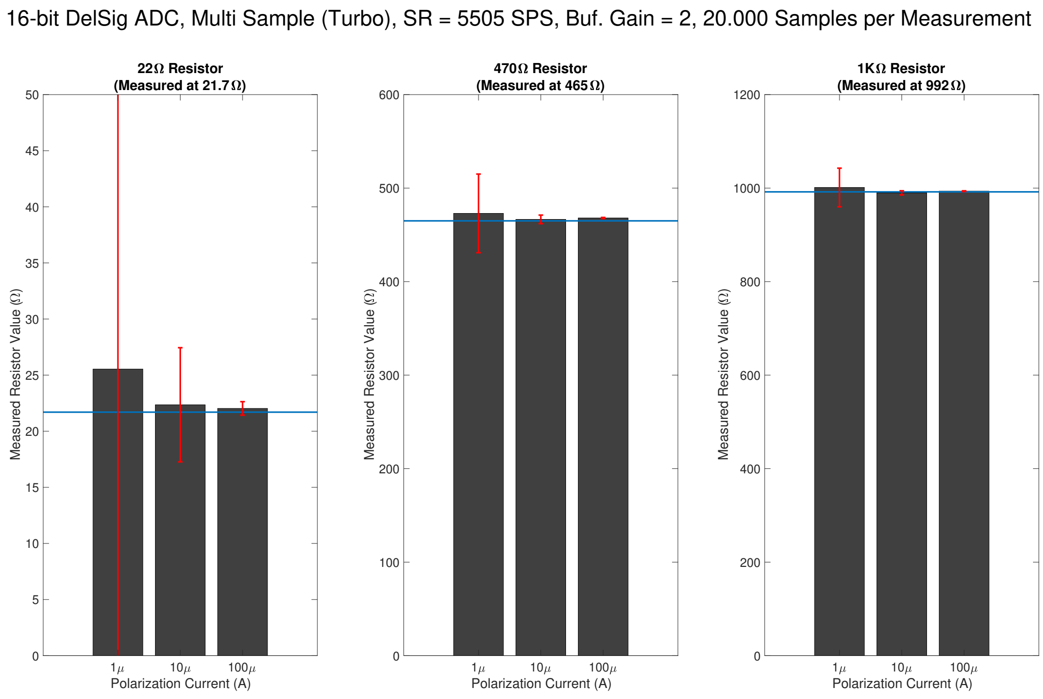

Figure 4.7: Results of measurements using 16-bit $\Delta - \Sigma$, Multi Sample (Turbo), SR = 5505 SPS, Buf. Gain = 2, 20.000 Samples per Measurement.

For these test parameters, measurement noise data is shown below, in Table 4.5, using the four metrics described in Section 4.2.

Table 4.5: Noise values of measurements using 16-bit $\Delta - \Sigma$, Multi Sample (Turbo), SR = 5505 SPS, Buf. Gain = 2, 20.000 Samples per Measurement.

Pol. Current (μA)		**1**			**10**			**100**	
Resistor Value(Ω)	22	465	992	22	465	992	22	465	992
Noise pk-pk (μV)	156	149	157	172	164	171	195	227	297
Noise 99.7% (μV)	135	126	124	153	138	134	180	189	241
RMS Noise (μV)	22.5	21.0	20.7	25.4	22.9	22.3	30.0	31.6	40.2
RMS Noise (LSB)	2.88	2.69	2.65	3.26	2.93	2.85	3.85	4.04	5.15

16-Bit, Buffer Gain = 1: This sixth test returns to unitary buffer gain and uses a sample rate of 11010 samples per second, with an LSB of 16 μA. Measurement accuracy data is presented in Figure 4.8.

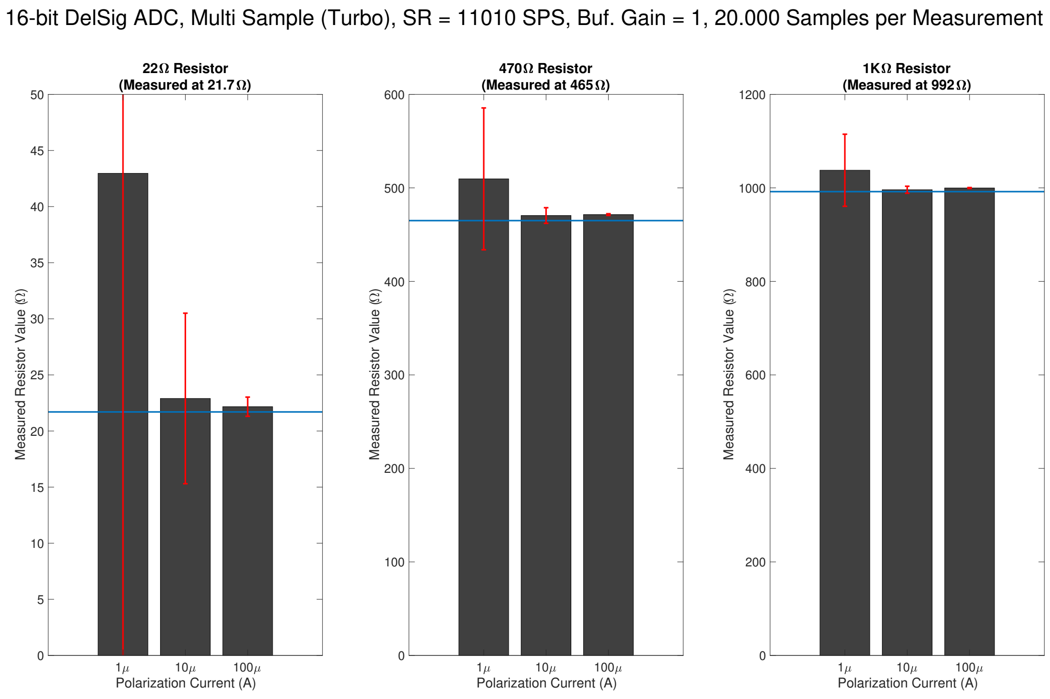

Figure 4.8: Results of measurements using 16-bit $\Delta - \Sigma$, Multi Sample (Turbo), SR = 11010 SPS, Buf. Gain = 1, 20.000 Samples per Measurement.

For these test parameters, measurement noise data is shown below, in Table 4.6, using the four metrics described in Section 4.2.

Table 4.6: Noise values of measurements using 16-bit $\Delta - \Sigma$, Multi Sample (Turbo), SR = 11010 SPS, Buf. Gain = 1, 20.000 Samples per Measurement.

Pol. Current (μA)		**1**			**10**			**100**	
Resistor Value(Ω)	22	465	992	22	465	992	22	465	992
Noise pk-pk (μV)	235	281	297	281	312	266	344	375	422
Noise 99.7% (μV)	203	228	231	228	251	224	256	278	317
RMS Noise (μV)	33.8	37.9	38.5	38.0	41.8	37.3	42.7	46.3	52.8
RMS Noise (LSB)	2.16	2.43	2.47	2.43	2.68	2.38	2.73	2.96	3.38

4.2.4 14-Bit Mode

For the last resolution setting we step down another 2 bits, thus this testing is done at 14 bits. Measurement accuracy data is presented in Figure 4.9.

14-Bit, Buffer Gain = 2: The seventh series of tests is done with a buffer gain of 2 and 14840 samples per second, which results in 32 μA of LSB.

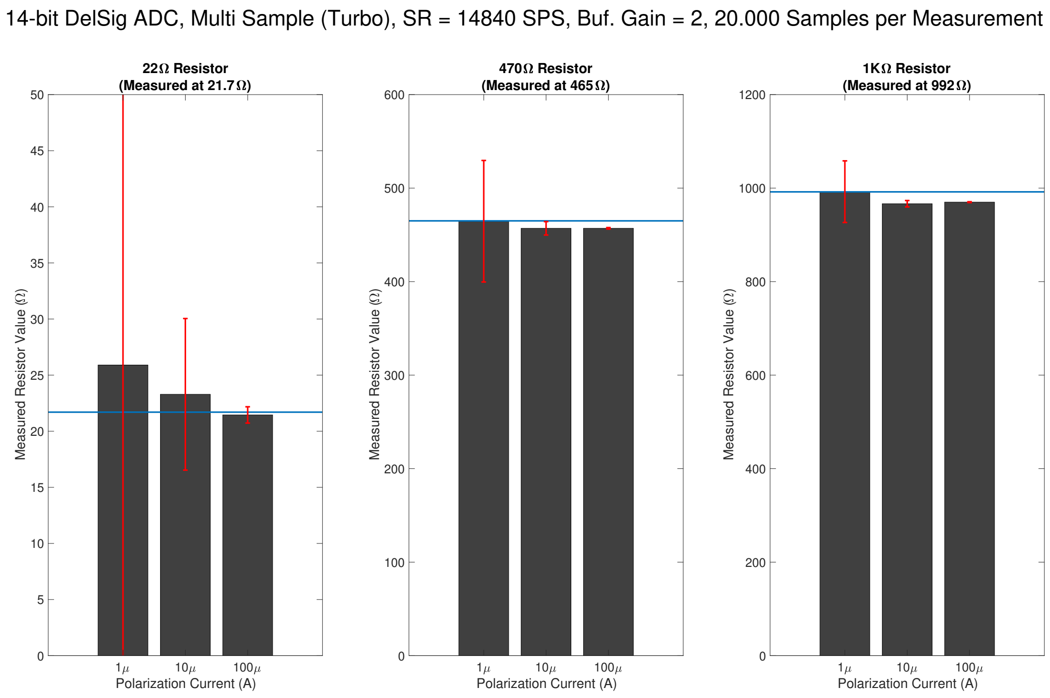

Figure 4.9: Results of measurements using 14-bit $\Delta-\Sigma$, Multi Sample (Turbo), SR = 14840 SPS, Buf. Gain = 2, 20.000 Samples per Measurement.

For these test parameters, measurement noise data is shown below, in Table 4.7, using the four metrics described in Section 4.2.

Table 4.7: Noise values of measurements using 14-bit $\Delta-\Sigma$, Multi Sample (Turbo), SR = 14840 SPS, Buf. Gain = 2, 20.000 Samples per Measurement.

Pol. Current (μA)		**1**			**10**			**100**	
Resistor Value(Ω)	22	465	992	22	465	992	22	465	992
Noise pk-pk (μV)	250	250	250	250	282	282	282	313	343
Noise 99.7% (μV)	177	195	198	203	215	205	218	238	275
RMS Noise (μV)	29.4	32.5	33.0	33.8	35.8	34.2	36.3	39.7	45.9
RMS Noise (LSB)	0.94	1.04	1.05	1.08	1.15	1.10	1.16	1.27	1.47

14-Bit, Buffer Gain = 1: The eighth and final test uses a buffer gain of 1 and samples the signal at 29681 samples per second, corresponding to an LSB of 64μA. Measurement accuracy data is presented in Figure 4.10.

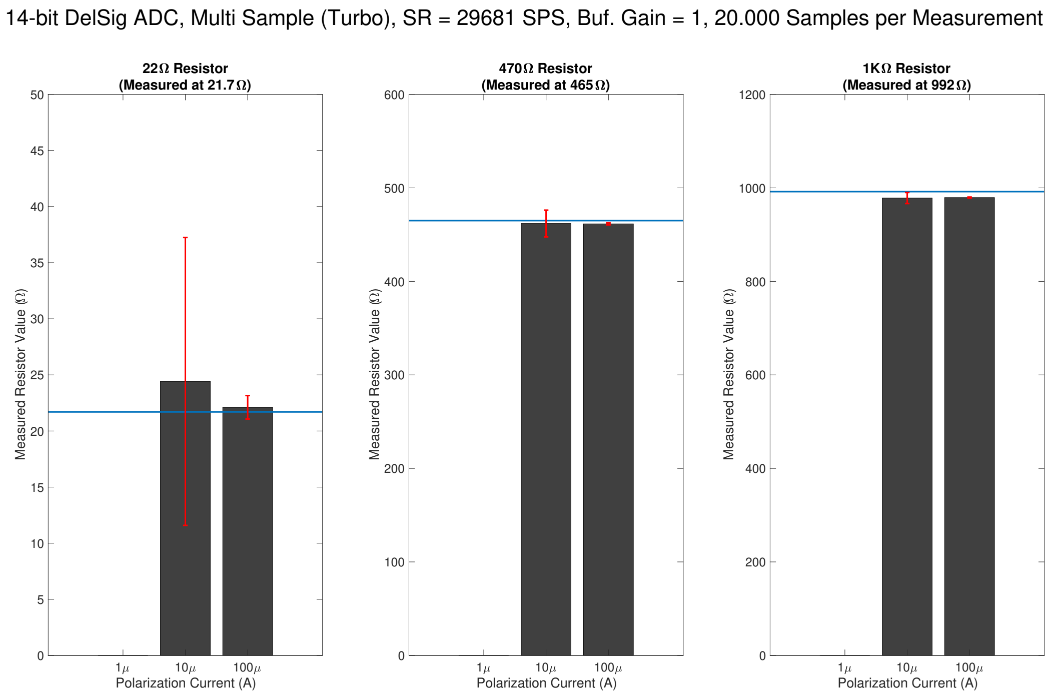

Figure 4.10: Results of measurements using 14-bit $\Delta - \Sigma$, Multi Sample (Turbo), SR = 29861 SPS, Buf. Gain = 1, 20.000 Samples per Measurement.

For these test parameters, measurement noise data is shown below, in Table 4.8, using the four metrics described in Section 4.2.

Table 4.8: Noise values of measurements using 14-bit $\Delta - \Sigma$, Multi Sample (Turbo), SR = 29861 SPS, Buf. Gain = 1, 20.000 Samples per Measurement.

Pol. Current (μA)		**1**			**10**			**100**	
Resistor Value(Ω)	22	465	992	22	465	992	22	465	992
Noise pk-pk (μV)	500	562	437	562	562	500	375	437	500
Noise 99.7% (μV)	366	363	362	385	429	355	313	319	366
RMS Noise (μV)	61.1	60.5	60.4	64.2	71.6	59.1	52.2	53.2	60.9
RMS Noise (LSB)	0.98	0.97	0.97	1.03	1.14	0.95	0.84	0.85	0.97

4.2.5 Drawing Conclusions From the Data

There are some clear observations that can be made from the acquired data, and educated guesses can be made for other observed phenomena.

Firstly, in terms of measurement accuracy value, it's quite obvious that there is a benefit in increasing the drive current of the measured resistor. While this current increase mostly results in higher noise, the effective signal to noise ratio improves immensely. This can be seen particularly well when looking at the 22 Ω resistor, due to its very low value. The 1 μA drive current results in a big disparity between the measured value and the real one, as even in the best possible resolution the peak to peak noise is in the order of 10 μV, which is just shy of half of the expected measured voltage across the resistor, that is, the signal to noise ratio is approximately 6 dB. With a 10 μA current, the noise level is similarly in the 10 μV range, while the expected measured voltage is now around 220 μV, resulting in a 22:1 signal to noise ratio, which corresponds to approximately 26.8 dB. With 100 μA of current, noise is anywhere from 50 to 120 μV, which once again increases signal to noise ratio. The conclusion here is simple then, a higher drive current is beneficial to measurement accuracy, as it increases signal to noise ratio (the voltage level of the signal increases faster than the voltage level of noise).

According to [53], it is possible to extrapolate the theoretical effective number of bits (ENOB) on the full scale of the ADC from the measurements made using equation 4.1.

$$ENOB = \frac{SINAD_{measured} - 1.76 + 20 \cdot log(\frac{FullScaleAmplitude}{InputAmplitude})}{6.02} \tag{4.1}$$

Where SINAD is the signal-to-noise-and-distortion ratio, in dB, Full Scale Amplitude and Input Amplitude in Volts.

Also according to [53], the value for SINAD can be approximated with a high confidence by the signal-to-noise ratio (SNR). This means that by calculating the SNR of the measurements, a good picture can be drawn regarding the effective number of bits on the Delta-Sigma ADC. Using the 20-bit resolution measurements, as these represent the measurements with the lowest noise values, the SNR values can be calculated for the three current levels, using Equation 4.2.

$$SNR = \frac{\mu}{\sigma} \tag{4.2}$$

Where μ is the mean value of the measurement and σ is the standard deviation, which corresponds to the RMS Noise.

The RMS values for all 20-bit measurements were calculated and are presented in Table 4.9.

Table 4.9: Signal-to-Noise Ratio of measurements using 20-bit $\Delta - \Sigma$, Multi Sample (Turbo), SR = 182 SPS, Buf. Gain = 1, 5.000 Samples per Measurement.

Pol. Current (μA)	**1**			**10**			**100**		
Resistor Value(Ω)	22	465	992	22	465	992	22	465	992
Signal (μV)	22	465	992	220	4650	9920	2200	46500	99200
RMS Noise (μV)	1.91	2.09	2.62	1.93	2.58	3.33	8.26	13.9	19.9
SN Ratio (dB)	21.2	46.9	51.6	41.5	65.1	69.5	48.5	70.5	73.9

Using Equation 4.1, we can take the SNR and calculate the ENOB for all the values:

Table 4.10: Signal-to-Noise Ratio of measurements using 20-bit $\Delta - \Sigma$, Multi Sample (Turbo), SR = 182 SPS, Buf. Gain = 1, 5.000 Samples per Measurement.

Pol. Current (μA)	**1**			**10**			**100**		
Resistor Value(Ω)	22	465	992	22	465	992	22	465	992
SN Ratio (dB)	21.2	46.9	51.6	41.5	65.1	69.5	48.5	70.5	73.9
ENOB	18.7	18.6	18.3	18.8	18.3	17.9	16.6	15.9	15.4

It is also important to mention that the ADC is using its Internal Reference, and measurements are being made in Single Ended mode. Referring to the datasheet for the $\Delta - \Sigma$ ADC Component of the PSoC [54], we can find some clues at what noise performance to expect when testing in these conditions.

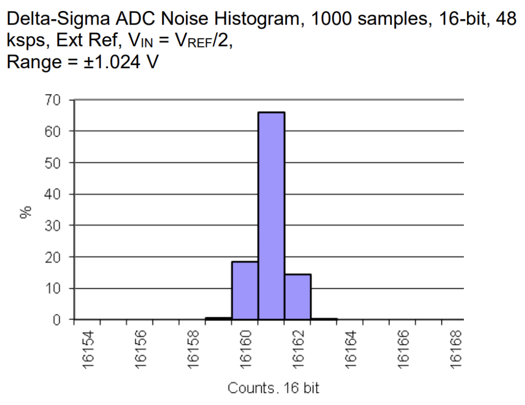

(a) External Reference

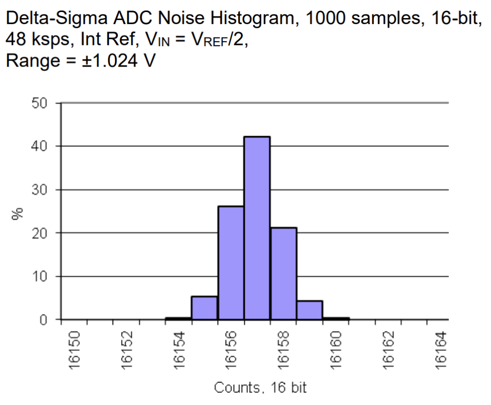

(b) Internal Reference

Figure 4.11: Comparison of Internal and External Reference Noise Performance, from [54].

From 4.11 it's clear to see that using a high precision external reference provides advantages when it comes to noise performance of the ADC. With an external reference, the measurements have a much smaller deviation from the mean value, which is especially noticeable when looking at the amount of measurements falling 2 or even 3 LSB to each side of the mean. Additionally, we can extract some data from Figure 4.12, obtained from [54], which show a comparison of the expected noise levels for single ended and differential measurements.

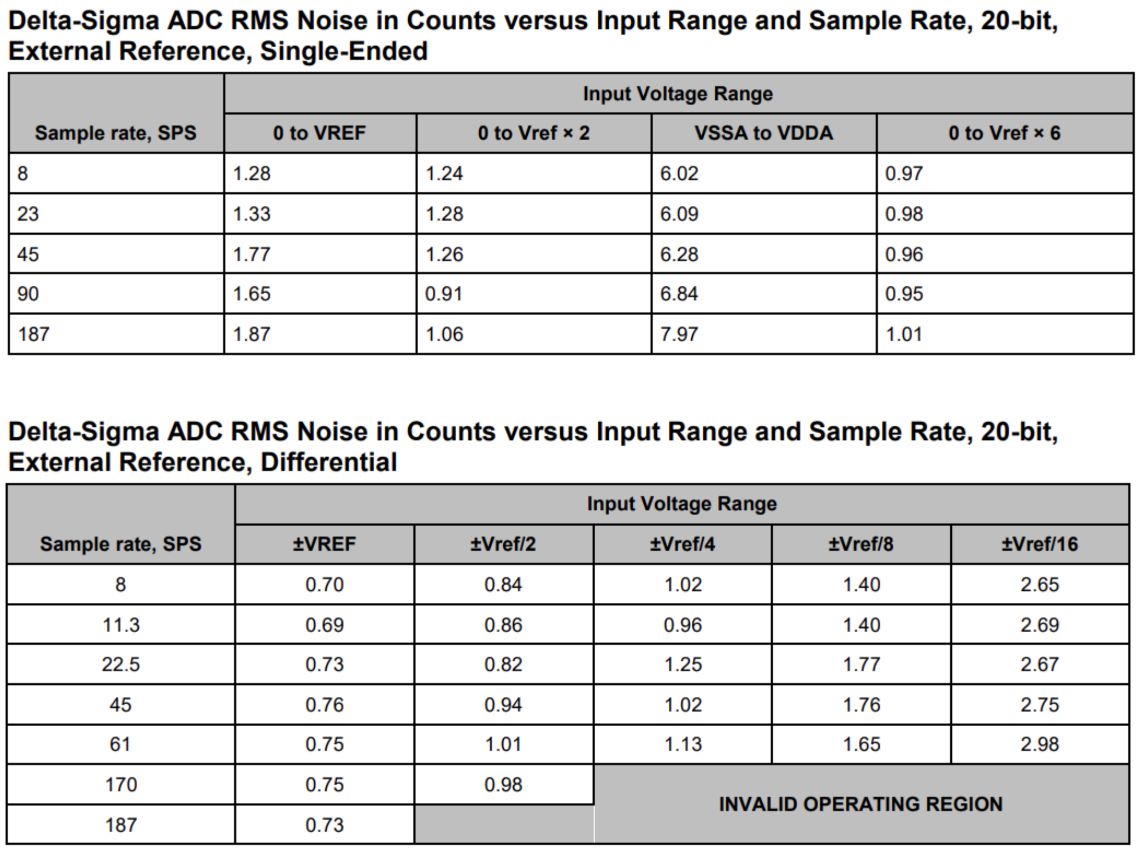

Delta-Sigma ADC RMS Noise in Counts versus Input Range and Sample Rate, 20-bit, External Reference, Single-Ended

Sample rate, SPS	Input Voltage Range			
	0 to VREF	0 to Vref × 2	VSSA to VDDA	0 to Vref × 6
8	1.28	1.24	6.02	0.97
23	1.33	1.28	6.09	0.98
45	1.77	1.26	6.28	0.96
90	1.65	0.91	6.84	0.95
187	1.87	1.06	7.97	1.01

Delta-Sigma ADC RMS Noise in Counts versus Input Range and Sample Rate, 20-bit, External Reference, Differential

Sample rate, SPS	Input Voltage Range				
	±VREF	±Vref/2	±Vref/4	±Vref/8	±Vref/16
8	0.70	0.84	1.02	1.40	2.65
11.3	0.69	0.86	0.96	1.40	2.69
22.5	0.73	0.82	1.25	1.77	2.67
45	0.76	0.94	1.02	1.76	2.75
61	0.75	1.01	1.13	1.65	2.98
170	0.75	0.98	INVALID OPERATING REGION		
187	0.73				

Figure 4.12: Comparison between single ended and differential noise performance, from [54]

Looking at the first column of both tables, it would seem like the differential measurement improves noise performance significantly, however it's important to notice that the measurement scale changes. In single ended mode, the measurements occur between 0 V and VREF, while in differential mode they occur between -VREF and +VREF, which effectively doubles the measurement scale and thus the value of the LSB.

This means that, in reality we should compare the first column of the single ended measurements with the second column of the differential measurements, as this provides the same LSB value for both measurement methods. Looking at the single ended mode, at 20 bits and at the highest sample speed possible, the expected RMS noise is 1.87 LSB. For a differential measurement with similar characteristics, albeit a slightly lower sample rate, the expected RMS noise is 0.98 LSB.

Considering the fact that these measurements were made with an external reference, at the highest resolution mode the $\Delta - \Sigma$ ADC can handle, 0.98 LSB of RMS noise is the absolute best case scenario. This value is around half the noise of that obtained in testing, both due to the differential nature of the measurements, and the use of an external reference. This means that future work should seriously consider both of these options in order to improve the noise performance of the ADC.

4.3 Testing the Internal Delta-Sigma ADC with High Value Resistors and Investigation into the Current DAC

From the testing with low values resistors, one interesting phenomenon can be observed, especially for the measurements with 100 μA of drive current, and that is that noise increases as the resistor value increases. This is something that should not be happening, as noise, both in the resistor and the ADC should be relatively constant. This increase in noise is especially noticeable with higher resolution settings, where the measurement noise is very low. When using 16 bits of resolution the effect practically disappears, and when using 14 bits it is completely unnoticeable, most likely due to the LSB noise overshadowing the strange noise detected.

Because the noise rises with resistor value, and mostly with 100 μA drive current, it is theorized that this noise is coming from the Current DAC, as the drawn power increases linearly with resistor value.

To test this hypotheses, 3 tests will be done, with a similar setup to those in Section 4.2, using 20, 18 and 16 bits of resolution with a unitary buffer gain, and the maximum sample rate possible for each resolution in Multi Sample (Turbo) mode.

If the noise being measured is coming from the Current DAC, this test should see a significant increase in noise compared to those in the last Section due to the increase in current draw being directly proportional to the measured resistor. However, the noise increase may not be linearly proportional to the drawn current, as there is no way of knowing what, inside the Current DAC, is the culprit of said noise.

Even if the expected noise increase is measured though, there can still be doubts if it is coming from the Current DAC or from the ADC itself, so there will be the need to compare the ADC noise for a high value resistor driven by the Current DAC with another voltage source that is known to be of very low noise. For this, a simple installation will be used with a lithium ion battery, which has a voltage of around 4 V, connected to a resistive divider.

The resistive divider is needed in order to bring the 4 V output from the battery into the 0 - 1.024 V measurement range of the ADC, however this testing setup will inevitably introduce some noise due to not only the resistive divider itself, but also the cables and connections used to interface the battery with the ADC. As such, this test should only be used to compare the Current DAC with an external voltage source and should not be used as a de facto baseline for the amount of noise that is to expect from an external sensor.

4.3.1 20-Bit Mode

Starting the testing for the high value resistors, 20 bits of resolution will be used. This testing doesn't intend to evaluate the measured value accuracy, only the measurement noise, so the bar graphs won't be shown, leaving only the noise tables for each of the resolutions.

Table 4.11: Noise values of measurements using 20-bit $\Delta - \Sigma$, Multi Sample (Turbo), SR = 182 SPS, Buf. Gain = 1, 5.000 Samples per Measurement.

Pol. Current (μA)		**1**			**10**			**100**	
Resistor Value(Ω)	3.3K	6.8K	10K	3.3K	6.8K	10K	3.3K	6.8K	10K
Noise 99.7% (μV)	17.0	27.4	39.4	36.4	69.3	98.0	303	592	842
RMS Noise (μV)	2.84	4.57	6.57	6.06	11.6	16.3	50.6	98.6	140
RMS Noise (LSB)	2.90	4.68	6.73	6.20	11.8	16.7	51.8	101	144
ENOB	18.2	17.5	17.0	17.1	16.1	15.6	14.0	13.1	12.6

4.3.2 18-Bit Mode

Next, we have the noise measurements for high value resistors using 18 bits of resolution.

Table 4.12: Noise values of measurements using 18-bit $\Delta - \Sigma$, Multi Sample (Turbo), SR = 2477 SPS, Buf. Gain = 1, 10.000 Samples per Measurement.

Pol. Current (μA)		**1**			**10**			**100**	
Resistor Value(Ω)	3.3K	6.8K	10K	3.3K	6.8K	10K	3.3K	6.8K	10K
Noise 99.7% (μV)	51.2	59.3	74.5	64.7	103	136	411	734	1162
RMS Noise (μV)	8.53	9.89	12.4	10.8	17.1	22.6	68.5	122	194
RMS Noise (LSB)	2.18	2.53	3.18	2.76	4.38	5.79	17.5	31.3	49.6
ENOB	16.6	16.4	16.0	16.2	15.6	15.2	13.6	12.7	12.1

4.3.3 16-Bit Mode

Lastly, we have the noise measurements for high value resistors using 16 bits of resolution.

Table 4.13: Noise values of measurements using 16-bit $\Delta - \Sigma$, Multi Sample (Turbo), SR = 11010 SPS, Buf. Gain = 1, 20.000 Samples per Measurement.

Pol. Current (μA)		**1**			**10**			**100**	
Resistor Value(Ω)	3.3K	6.8K	10K	3.3K	6.8K	10K	3.3K	6.8K	10K
Noise 99.7% (μV)	173	182	204	170	198	225	513	931	1339
RMS Noise (μV)	28.8	30.3	34.0	28.3	33.0	37.5	85.4	155	223
RMS Noise (LSB)	1.84	1.94	2.18	1.81	2.12	2.40	5.47	9.93	14.3
ENOB	14.8	14.8	14.6	14.9	14.6	14.4	13.3	12.4	11.9

4.3.4 Measuring the Voltage of an External Battery

A battery is a very stable voltage source, which should provide a good indication if the measured noise is coming from the $\Delta - \Sigma$ ADC or the Current DAC. If, for a similar voltage value, the noise in the measurement is significantly smaller when testing the battery, then we can have even more evidence that the Current DAC is causing the noise observed.

For this test, a Lithium-Ion battery will be used. This type of battery provides a voltage between 3 and 4.2 Volts which is incompatible with the 0-1.024 V measurement range of the $\Delta - \Sigma$ ADC, which means a resistive divider has to be used to lower this voltage. This resistive divider consists of a 220 Ω and a 1 KΩ resistor, which are relatively low values in order to keep the thermal noise from the resistive divider to the minimum. Even then, the resistive divider is placed on a breadboard which means some additional noise will sure be generated by the battery connections to the breadboard, and from the breadboard to the PSoC, which means the noise value won't be the absolute best achievable, and should only be used to compare with the noise obtained in previous tests.

With the resistive divider in place, and a measured battery voltage of 4.06 V, the voltage at the terminals of the ADC should be around 0.73V. This is similarly comparable to the 6.8 KΩ resistor with a 100 μA drive current, which is the comparison we can see in Table 4.14.

Table 4.14: Noise values of measurements using 20-bit $\Delta - \Sigma$, Multi Sample (Turbo), SR = 182 SPS, Buf. Gain = 1, 5.000 Samples per Measurement, comparing a battery and a resistor.

Pol. Current (μA)	-	100
Resistor Value(Ω)	-	6.8K
Battery Voltage (V)	0.73	-
Noise 99.7% (μV)	96.0	592
RMS Noise (μV)	16.4	98.6
RMS Noise (LSB)	16.0	101
ENOB	15.2	13.1

The absolute measured average voltage on the resistive divider is 0.7277 V which is very close to the expected value, confirming that the measurement was successful. It's also easy to observe that the battery measurement has a drastically lower noise level than the measurement with the 6.8 KΩ resistor with a 100μA drive current. This leads to the conclusion that this noise is coming from the Current DAC, however it's unknown if this is the normal operation of the PSoC μC or a problem with the developed PCB, which means some additional tests will be needed to compare the developed PCB with a Prototyping Kit developed by Cypress.

4.3.5 Comparing the Developed PCB with a Prototyping Kit

As a final test, the performance of the developed PCB was tested against the CY8CKIT-059 Prototyping Kit as a way to ensure the odd results were not due to incorrect PCB design, and were, in fact, a characteristic of the PSoC 5LP microcontroller. A single 10 KΩ resistor was measured at 100 μA of drive current, which was causing the highest amount of noise in the previous tests. The noise results of these tests, compared to the developed board, can be seen in Table 4.15.

Table 4.15: Comparison of noise values of measurements using 20-bit $\Delta - \Sigma$, Multi Sample (Turbo), SR = 182 SPS, Buf. Gain = 1, 5.000 Samples per Measurement, comparing the and a resistor.

Pol. Current (μA)	100	
Resistor Value(Ω)	10K	
Device Under Test	Dev. Node	CY8CKIT-059
Noise 99.7% (μV)	842	693
RMS Noise (μV)	140	116
RMS Noise (LSB)	144	118
ENOB	12.6	12.8

Some of the differences in the results can be attributed to the connection of the resistor to the PCB. In the CY8CKIT-059, the resistor can be introduced directly into the female pin headers, while on the developed board, male pin headers were used, which means the resistor has to use a small female to female cable. Additionally, the developed board has multiplexer chips in the signal path, which may introduce some more measurement noise. Even with these differences, the measurements on both boards seem to display a pattern of additional noise as the drive current increases for these relatively high value resistor measurements.

Either way, the order of magnitude of the sampled noise is the same in both cases, and that is enough to prove that the issue at hand comes from the PSoC 5LP microcontroller and not from any design errors, as even tho the noise is slightly lower on the CY8CKIT-059, it is still a whole two orders of magnitude higher than what would be expected, and from what is actually observed for low value resistors with a smaller drive current. This makes the PSoC 5LP completely unsuited for these types of measurements, because even tho it has a very high precision ADC, the DAC cannot keep up.

4.4 Testing the AD5941 Analog Front End and u-blox SARA-N2 NB-IoT Module

AD5941: The AD5941 uses direct register manipulation to control the chip's functions. Fortunately, a software library, as well as some example functions are provided by Analog Devices to the users of this IC. The implementation of this library was described in Section 3.2.4.2.

In this test, one of the example functions provided by Analog Digital was used to test the reading and writing to the AD5941's registers through the SPI interface. This example is called "AD5940_SPI" and executes ten thousand consecutive writes and consecutive reads from a specific register. The objective is to write a determined value to a register and be able to read back this same value. If the read value corresponds to the written value, then a successful SPI connection has been established. Repeating this test a large number of times helps to detect some kind of instability that may be occurring with the data transmission.

Unfortunately, this test proved unsuccessful. The writing sequence did not present an issue, however when the register value was read back, there would be no data transmission coming from the AD5941. This is a somewhat inconclusive issue, as it doesn't provide enough data to truly evaluate if the problem occurs when reading or writing the data. One assumption is that the problem may be in the AD5941 itself, as during debugging of some of the initial PCB mistakes described in Section 3.1.6 a 5 V signal may have been accidentally injected in the 3.3 V rail, therefore damaging the IC. This however doesn't appear to be the issue, as both the internal 1.82 V and 2.5 V regulators measure their respective voltages under a multimeter, and show good, constant signals when observed in an oscilloscope, as can be seen from Figures 4.13 and 4.14.

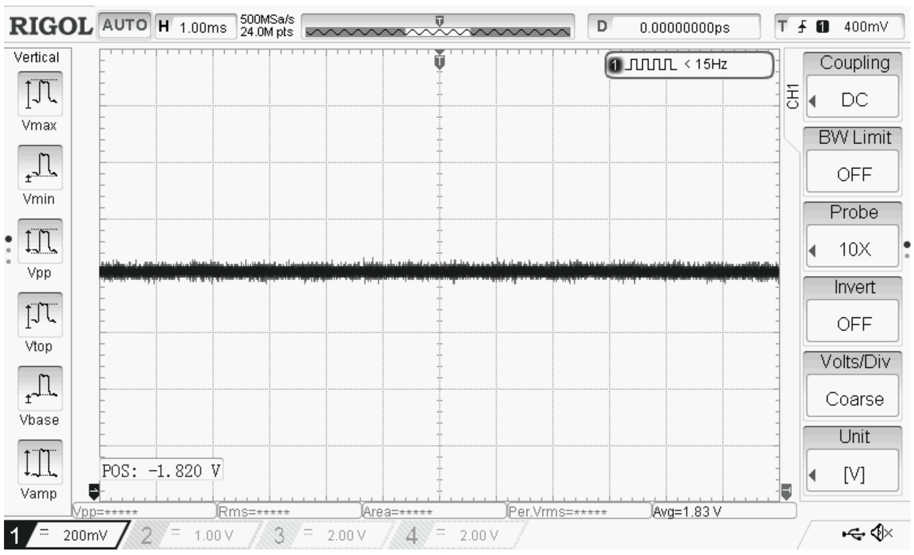

Figure 4.13: Oscilloscope trace of the AD5941's 1.82 V Regulator.

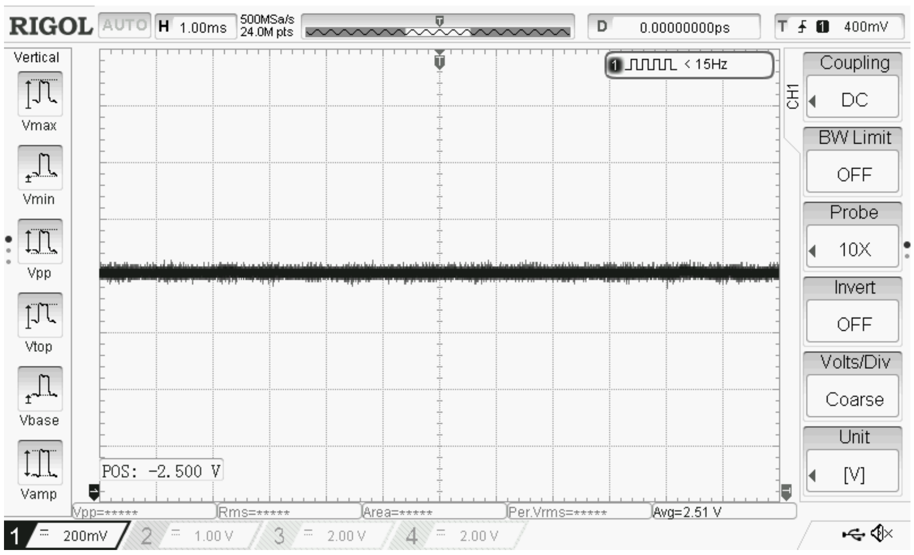

Figure 4.14: Oscilloscope trace of the AD5941's 2.5 V Regulator.

These are very unfortunate results, as even several attempts to solve the problem proved useless. The described issue can also be observed through a Logic Analyzer in Figures 4.15 and 4.16 .

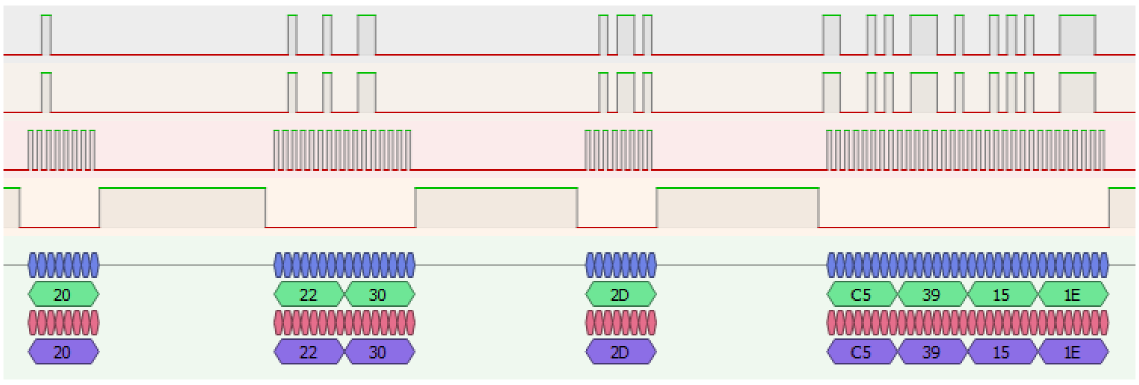

Figure 4.15: Logic Analyzer Data of a SPI Write Command to the AD5941.

Figure 4.15 shows an SPI Write Command. Initially a byte with 0x20 is sent, this is defined in the AD5941's library as "set address", telling the AD5941 that a register address will follow, which in this case is 0x2230. Another byte is then sent with the address 0x2D which is a "write address" command, followed by 0xC539151E, randomly generated data to write into the 0x2230 register.

Similarly to the SPI Write Command, the SPI Read Command shown in Figure 4.16 starts with a 0x20 "set address" command, and the 0x2230 address is sent. Things then start to differ, as this time a 0x6D "read address" command is sent. After this, a dummy read is done, then CS is once again pulled low in order to receive data, however the AD5941 doesn't respond.

The purpose of the dummy read is to generate pulses on the clock line, which the slave device then detects and replies to. This is the implementation provided in the AD5941's library and should be expected to work, but it does not. This means that the problem is most likely hardware related.

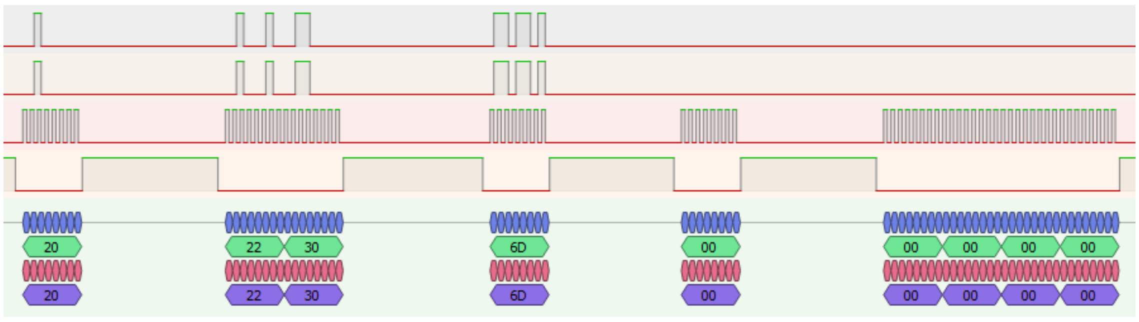

Figure 4.16: Logic Analyzer Data of a SPI Read Command to the AD5941.

u-blox SARA-N2: The u-blox SARA-N2 NB-IoT module was a big bet when designing this sensor board, however it could not be tested in the allotted time. Testing this module would require an NB-IoT enabled SIM card and the development of a significant amount of software which simply there was not enough time for.

Chapter 5

Conclusion

This dissertation work proposed to create the basis for an adaptable and reconfigurable IoT node with the ability to measure data from several environmental sensors with an extremely high level of accuracy.

An IoT architecture was developed with the use of a state of the art PSoC microcontroller with a very high resolution ADC and a additional, optional, analog front end integrated circuit in the form of the Analog Devices AD5941. Multiplexers would tie the sensor inputs to the ADCs in either the PSoC or the AD5941 in order to accommodate a larger number of sensors than either of these devices would allow.

Wireless communications would be assured by the u-blox SARA N210 NB-IoT module, which allows long distance communication at low data rates, with low energy usage, over vast distances.

A 4-layer printed circuit board was developed in KiCad containing all the describe components, while taking into account several layout considerations described in Chapter 3.1. This circuit board was designed in a way that it could form a foundation for future work in this area, with its design files being made available for change and development.

The developed circuit board was then manufactured by JLCPCB, components were ordered from Mouser and Digikey and then reflow soldered in a reflow oven. At this point some unexpected issues arose which delayed development, as the PSoC microcontroller would not initialize. This issue was tracked to a design mistake in the PCB which was luckily a relatively easy fix, however it was extremely time consuming, as it took over a month between diagnosing and ordering new parts.

With the PCB issue remedied, software was developed to test the different components of the board, starting with the simplest which were the MAX14661 multiplexers, then following with the PSoC microcontroller and the AD5941 analog front end module.

All six of the MAX14661 multiplexers were tested and worked with no issues. Moving on to the PSoC microcontroller, tests were made at various ADC resolutions and sample rates, with some unexpected results, both positively and negatively. To start, the 20-bit Delta-Sigma ADC has extremely good noise performance, generating some very impressive results when testing resistors at low drive currents such as 1 and 10 μA, resulting in an effective number of bits (ENOB) which is calculated to be above 18 bits and almost as high as 19 bits for the best case scenario, while also having 15.2 effective bits measured in the battery comparison made in Chapter 4.14, which is a non-ideal scenario as there is a resistive divider and some questionable quality connectors involved.

There were however some negative results at higher currents, and with higher resistor values, which were investigated and tracked to be caused by an extremely noisy output coming from the current DACs. This was extremely unfortunate as it means that the high resolution ADC is almost completely useless in these tests, resulting in an ENOB as low as only 12.6 when measuring at a 20-bit resolution, meaning that the only thing the ADC effectively measures is noise being generated by the DAC. These tests are presented in length in Chapters 4.2 and 4.3.

When it came to AD5941 analog front end module, it was discovered that it was unresponsive to user commands, either through severe user error, which seems unlikely as the library which implements the AD5941 functionality is very simple to import for a given microcontroller architecture, or due to hardware issues which possibly occurred when diagnosing the initial problems with the PSoC microcontroller. Either way, testing of the AD5941 was impossible to realize, which is extremely unfortunate, as this module appears to be very promising, as it contains an extremely good suite of ADCs and DACs specially designed to interface with sensors which need very high precision measurements such as skin and body impedance or electrochemical toxic gas sensing.

5.1 Future Work

There is a relatively high likelihood of future work being developed on top of the developed IoT node, therefore the project was uploaded to GitHub at GitHub - KNoT. This also means that some tips or recommendations will be rather important.

Firstly, it is very important to understand the capabilities of the AD5941, as this module appears to be extremely capable in the application this IoT node is designed to fulfill. Not being able to even run basic tests on this chip is probably one of the biggest disappointments of this dissertation.

Evaluation boards for this module are available, although they are prohibitively expensive, however a simple test setup can be developed by designing a small, custom made "evaluation board"which provides an SPI connection to an external off the shelf microcontroller board such as Arduino or a Raspberry Pi for data communication, and exposes the sensor input ports of the AD5941 to a small sensor connector. This will not only help validate the performance claims of this module, but also develop the required interface software.

If this module does as much as it advertises, it is important to chose a clear direction about whether to integrate it directly into the mainboard, as this can lead to a different strategy regarding the main microcontroller platform, as the choice of PSoC 5LP hinged mainly on its signal acquisition capabilities which were tested and found not to be very satisfactory, meaning that it could then be switched to a more powerful and cheaper one, such as the STM32 family, leading to an improvement in the node's signal capabilities which can help with filtering and processing measured data.

Regarding the NB-IoT module, a lot of work also needs to be put into it regarding software interfacing and general RF testing, specially as NB-IoT is still a somewhat niche communication standard with limited software support. Between the AD5941 and the NB-IoT node, there is easily enough research work for two dissertations, specially as they both require a lot of testing and data gathering, as they are relatively new and unexplored platforms.

Some additional considerations were also discussed in Chapter 3.1.6 regarding developments to the current printed circuit board, namely the placement of additional pins connecting the AD5941's GPIOs and RESET pins to the mainboard.

To summarize, as future work, it is important to:

- Research and test the capabilities of the AD5941.
- Research and test the SARA-N2 NB-IoT module.
- Decide whether to integrate the AD5941 in the mainboard.
- Decide between continuing to use the PSoC microcontroller or switch to an alternative platform.

Bibliography

[1] Z. Xinhua and L. Hong. "A Self-Reconfigurable Sensor Network Constructon Reaseach in the Paradigm of Internet of Things." In: *2012 International Conference on Computer Science and Service System*. Aug. 2012, pp. 311–314. DOI: 10.1109/CSSS.2012.85.

[2] D. Singh, G. Tripathi, and A. J. Jara. "A survey of Internet-of-Things: Future vision, architecture, challenges and services." In: *2014 IEEE World Forum on Internet of Things (WF-IoT)*. Mar. 2014, pp. 287–292. DOI: 10.1109/WF-IoT.2014.6803174.

[3] I. T. Union. *Recommendation ITU-T Y.2060. Overview of the Internet of things*. June 2012. URL: http://handle.itu.int/11.1002/1000/11559-en?locatt=format:pdf&auth.

[4] A. Glória, F. Cercas, and N. Souto. "Comparison of communication protocols for low cost Internet of Things devices." In: *2017 South Eastern European Design Automation, Computer Engineering, Computer Networks and Social Media Conference (SEEDA-CECNSM)*. Sept. 2017, pp. 1–6. DOI: 10.23919/SEEDA-CECNSM.2017.8088226.

[5] Cypress. *Cypress PSoC® 6 Microcontrollers. Purpose-Built for the Internet of Things*. URL: https://www.cypress.com/file/386296/download.

[6] M. Electronics. *Internet of Things. IoT Sensor Node Block Diagram*. URL: https://eu.mouser.com/applications/internet-of-things-block-diagram/.

[7] A. A. Abudaqa, T. M. Al-Kharoubi, M. F. Mudawar, and A. Kobilica. "Simulation of ARM and x86 microprocessors using in-order and out-of-order CPU models with Gem5 simulator." In: *2018 5th International Conference on Electrical and Electronic Engineering (ICEEE)*. May 2018, pp. 317–322. DOI: 10.1109/ICEEE2.2018.8391354.

[8] Z. Ou, B. Pang, Y. Deng, J. K. Nurminen, A. Ylä-Jääski, and P. Hui. "Energy- and Cost-Efficiency Analysis of ARM-Based Clusters." In: *2012 12th IEEE/ACM International Symposium on Cluster, Cloud and Grid Computing (ccgrid 2012)*. May 2012, pp. 115–123. DOI: 10.1109/CCGrid.2012.84.

[9] P. Greenhalgh. *Big.LITTLE Processing with ARM Cortex™-A15 & Cortex-A7. Improving Energy Efficiency in High-Performance Mobile Platforms*. Sept. 2011. URL: https://www.cl.cam.ac.uk/~rdm34/big.LITTLE.pdf.

[10] Z. Wang, Y. Liu, Y. Sun, Y. Li, D. Zhang, and H. Yang. "An energy-efficient heterogeneous dual-core processor for Internet of Things." In: *2015 IEEE International Symposium on Circuits and Systems (ISCAS)*. May 2015, pp. 2301–2304. DOI: 10.1109/ISCAS.2015.7169143.

[11] J. Yiu. *ARM® Cortex®-M for Beginners. An overview of the ARM Cortex-M processor family and comparison*. Sept. 2012. URL: https://community.arm.com/cfs-file/__key/telligent-evolution-components-attachments/01-2142-00-00-00-00-52-96/White-Paper-_2D00_-Cortex_2D00_M-for-Beginners-_2D00_-2016-_2800_final-v3_2900_.pdf.

[12] C. C. Corporation, H.-P. Company, I. Corporation, L. T. Inc, M. Corporation, N. Corporation, and K. P. E. N.V. *Universal Serial Bus Specification*. Apr. 2000. URL: https://www.usb.org/document-library/usb-20-specification.

[13] M. Lauridsen, R. Krigslund, M. Rohr, and G. Madueno. "An Empirical NB-IoT Power Consumption Model for Battery Lifetime Estimation." In: *2018 IEEE 87th Vehicular Technology Conference (VTC Spring)*. June 2018, pp. 1–5. DOI: 10.1109/VTCSpring.2018.8417653.

[14] Y. E. Wang, X. Lin, A. Adhikary, A. Grovlen, Y. Sui, Y. Blankenship, J. Bergman, and H. S. Razaghi. "A Primer on 3GPP Narrowband Internet of Things." In: *IEEE Communications Magazine* 55.3 (Mar. 2017), pp. 117–123. ISSN: 1558-1896. DOI: 10.1109/MCOM.2017.1600510CM.

[15] F. Adelantado, X. Vilajosana, P. Tuset-Peiro, B. Martinez, J. Melia-Segui, and T. Watteyne. "Understanding the Limits of LoRaWAN." In: *IEEE Communications Magazine* 55.9 (Sept. 2017), pp. 34–40. ISSN: 1558-1896. DOI: 10.1109/MCOM.2017.1600613.

[16] B. Rajesh, A. Agarwal, and K. A. Saravanan. "Proficient modus operandi for scrutinize air pollution using wireless sensor network." In: *2014 International Conference on Circuits, Power and Computing Technologies [ICCPCT-2014]*. Mar. 2014, pp. 1312–1316. DOI: 10.1109/ICCPCT.2014.7054852.

[17] T. Liu, Z. Liu, and R. W. Jones. "The Evolution of Air Pollution Monitoring and Modelling in Zhejiang Province." In: *2019 14th IEEE Conference on Industrial Electronics and Applications (ICIEA)*. June 2019, pp. 107–112. DOI: 10.1109/ICIEA.2019.8834054.

[18] M. Mukta, S. Islam, S. D. Barman, A. W. Reza, and M. S. Hossain Khan. "Iot based Smart Water Quality Monitoring System." In: *2019 IEEE 4th International Conference on Computer and Communication Systems (ICCCS)*. Feb. 2019, pp. 669–673. DOI: 10.1109/CCOMS.2019.8821742.

[19] L. Mezzera, M. Carminati, M. Di Mauro, A. Turolla, M. Tizzoni, and M. Antonelli. "A 7-Parameter Platform for Smart and Wireless Networks Monitoring On-Line Water Quality." In: *2018 25th IEEE International Conference on Electronics, Circuits and Systems (ICECS)*. Dec. 2018, pp. 709–712. DOI: 10.1109/ICECS.2018.8618014.

[20] B. Das and P. C. Jain. "Real-time water quality monitoring system using Internet of Things." In: *2017 International Conference on Computer, Communications and Electronics (Comptelix)*. July 2017, pp. 78–82. DOI: 10.1109/COMPTELIX.2017.8003942.

[21] N. Vijayakumar and R. Ramya. "The real time monitoring of water quality in IoT environment." In: *2015 International Conference on Innovations in Information, Embedded and Communication Systems (ICIIECS)*. Mar. 2015, pp. 1–5. DOI: 10.1109/ICIIECS.2015.7193080.

[22] P. Sharma and D. V. Padole. "Design and implementation soil analyser using IoT." In: *2017 International Conference on Innovations in Information, Embedded and Communication Systems (ICIIECS)*. Mar. 2017, pp. 1–5. DOI: 10.1109/ICIIECS.2017.8275947.

[23] P. Rajalakshmi and S. Devi Mahalakshmi. "IOT based crop-field monitoring and irrigation automation." In: *2016 10th International Conference on Intelligent Systems and Control (ISCO)*. Jan. 2016, pp. 1–6. DOI: 10.1109/ISCO.2016.7726900.

[24] O. Pandithurai, S. Aishwarya, B. Aparna, and K. Kavitha. "Agro-tech: A digital model for monitoring soil and crops using internet of things (IOT)." In: *2017 Third International Conference on Science Technology Engineering Management (ICONSTEM)*. Mar. 2017, pp. 342–346. DOI: 10.1109/ICONSTEM.2017.8261306.

[25] R. D. Down. "Temperature Measurement." In: *Environmental Instrumentation and Analysis Handbook*. John Wiley & Sons, Ltd, 2005. Chap. 21, pp. 445–458. ISBN: 9780471473336. DOI: 10.1002/0471473332.ch21. URL: https://onlinelibrary.wiley.com/doi/abs/10.1002/0471473332.ch21.

[26] J. R. Gray. "Conductivity Analyzers and Their Application." In: *Environmental Instrumentation and Analysis Handbook*. John Wiley & Sons, Ltd, 2005. Chap. 23, pp. 491–510. ISBN: 9780471473336. DOI: 10.1002/0471473332.ch23. URL: https://onlinelibrary.wiley.com/doi/abs/10.1002/0471473332.ch23.

[27] P. M. Ramos, J. M. D. Pereira, H. M. G. Ramos, and A. L. Ribeiro. "A Four-Terminal Water-Quality-Monitoring Conductivity Sensor." In: *IEEE Transactions on Instrumentation and Measurement* 57.3 (Mar. 2008), pp. 577–583. ISSN: 1557-9662. DOI: 10.1109/TIM.2007.911703.

[28] A. D. Inc. *ADI Water Analysis Solution for pH Meters and Conductivity Meters*. 2013. URL: https://www.analog.com/media/cn/technical-documentation/apm-pdf/adi-water-analysis-solutions_en.pdf.

[29] E. A. Atekwana, E. A. Atekwana, R. S. Rowe, D. D. Werkema, and F. D. Legall. "The relationship of total dissolved solids measurements to bulk electrical conductivity in an aquifer contaminated with hydrocarbon." In: *Journal of Applied Geophysics* 56.4 (2004), pp. 281 –294. ISSN: 0926-9851. DOI: https://doi.org/10.1016/j.jappgeo.2004.08.003. URL: http://www.sciencedirect.com/science/article/pii/S0926985104000576.

[30] J. R. Gray. "pH Analyzers and Their Application." In: *Environmental Instrumentation and Analysis Handbook*. John Wiley & Sons, Ltd, 2005. Chap. 22, pp. 459–490. ISBN: 9780471473336. DOI: 10.1002/0471473332.ch22. URL: https://onlinelibrary.wiley.com/doi/abs/10.1002/0471473332.ch22.

[31] T. I. Incorporated. *SAR ADCs vs. Delta-Sigma ADCs: Different architectures for different application needs*. 2015. URL: https://training.ti.com/adcwebinar.

[32] G. Castro. *Rarely Asked Questions—Issue 133 Common Sense for Current Sensing*. 2013. URL: https://www.analog.com/media/en/analog-dialogue/raqs/raq-issue-133.pdf.

[33] N. Paulino. *Analog to Digital Converters*. Electrónica III Course Presentation at DEE - FCT/UNL. 2016-2017.

[34] P. Horowitz and W. Hill. *The Art of Electronics*. 3rd. USA: Cambridge University Press, 2015. ISBN: 0521809266.

[35] U. Farooq, Z. Marrakchi, and H. Mehrez. *Tree-based Heterogeneous FPGA Architectures: Application Specific Exploration and Optimization*. SpringerLink : Bücher. Springer New York, 2012. ISBN: 9781461435945. URL: https://books.google.pt/books?id=FGGeSu_txOAC.

[36] S. Dhote, P. Charjan, A. Phansekar, A. Hegde, S. Joshi, and J. Joshi. "Using FPGA-SoC interface for low cost IoT based image processing." In: *2016 International Conference on Advances in Computing, Communications and Informatics (ICACCI)*. Sept. 2016, pp. 1963–1968. DOI: 10.1109/ICACCI.2016.7732339.

[37] X. Zhang, X. Liu, A. Ramachandran, C. Zhuge, S. Tang, P. Ouyang, Z. Cheng, K. Rupnow, and D. Chen. "High-performance video content recognition with long-term recurrent convolutional network for FPGA." In: *2017 27th International Conference on Field Programmable Logic and Applications (FPL)*. Sept. 2017, pp. 1–4. DOI: 10.23919/FPL.2017.8056833.

[38] F. Baskaya, S. Reddy, Sung Kyu Lim, and D. V. Anderson. "Placement for large-scale floating-gate field-programable analog arrays." In: *IEEE Transactions on Very Large Scale Integration (VLSI) Systems* 14.8 (Aug. 2006), pp. 906–910. ISSN: 1557-9999. DOI: 10.1109/TVLSI.2006.878477.

[39] C. M. Twigg and P. Hasler. "A Large-Scale Reconfigurable Analog Signal Processor (RASP) IC." In: *IEEE Custom Integrated Circuits Conference 2006*. Sept. 2006, pp. 5–8. DOI: 10.1109/CICC.2006.320937.

[40] A. Basu, S. Brink, C. Schlottmann, S. Ramakrishnan, C. Petre, S. Koziol, F. Baskaya, C. M. Twigg, and P. Hasler. "A Floating-Gate-Based Field-Programmable Analog Array." In: *IEEE Journal of Solid-State Circuits* 45.9 (Sept. 2010), pp. 1781–1794. ISSN: 1558-173X. DOI: 10.1109/JSSC.2010.2056832.

[41] S. Brink, J. Hasler, and R. Wunderlich. "Adaptive Floating-Gate Circuit Enabled Large-Scale FPAA." In: *IEEE Transactions on Very Large Scale Integration (VLSI) Systems* 22.11 (Nov. 2014), pp. 2307–2315. ISSN: 1557-9999. DOI: 10.1109/TVLSI.2013.2290305.

[42] C. R. Schlottmann, S. Shapero, S. Nease, and P. Hasler. "A Digitally Enhanced Dynamically Reconfigurable Analog Platform for Low-Power Signal Processing." In: *IEEE Journal of Solid-State Circuits* 47.9 (Sept. 2012), pp. 2174–2184. ISSN: 1558-173X. DOI: 10.1109/JSSC.2012.2194847.

[43] A. Malcher and P. Falkowski. "Analog Reconfigurable Circuits." In: *International Journal of Electronics and Telecommunications* 60 (Mar. 2014). DOI: 10.2478/eletel-2014-0002.

[44] J. Mocnej, M. Miškuf, P. Papcun, and I. Zolotová. "Impact of Edge Computing Paradigm on Energy Consumption in IoT." In: *IFAC-PapersOnLine* 51.6 (2018). 15th IFAC Conference on Programmable Devices and Embedded Systems PDeS 2018, pp. 162 –167. ISSN: 2405-8963. DOI: https://doi.org/10.1016/j.ifacol.2018.07.147. URL: http://www.sciencedirect.com/science/article/pii/S2405896318308917.

[45] M. A. López Peña and I. Muñoz Fernández. "SAT-IoT: An Architectural Model for a High-Performance Fog/Edge/Cloud IoT Platform." In: *2019 IEEE 5th World Forum on Internet of Things (WF-IoT)*. Apr. 2019, pp. 633–638. DOI: 10.1109/WF-IoT.2019.8767282.

[46] *ADuCM355 Data Sheet*. Rev. C. Analog Devices. Apr. 2020. URL: https://www.analog.com/media/en/technical-documentation/data-sheets/ADuCM355.pdf.

[47] *AD5940/AD5941 Data Sheet*. Rev. B. Analog Devices. Mar. 2020. URL: https://www.analog.com/media/en/technical-documentation/data-sheets/AD5940-5941.pdf.

[48] *MAX14661 Data Sheet*. Revision 2. Maxim Integrated. Jan. 2015. URL: https://datasheets.maximintegrated.com/en/ds/MAX14661.pdf.

[49] J. Charras and KiCad Developers Team. *KiCad*. Version 5.1.7. Nov. 28, 2020. URL: https://kicad.org/.

[50] "Fundamentals of Grounding Design." In: *Grounds for Grounding*. John Wiley & Sons, Ltd, 2010. Chap. 4, pp. 155–322. ISBN: 9780470529324. DOI: 10.1002/9780470529324.ch4.

[51] *SARA-N2 series Data Sheet*. R18. u-blox. Nov. 2019. URL: https://www.u-blox.com/en/docs/UBX-15025564.

[52] *AN77900 - PSoC 3 and PSoC 5LP Low-Power Modes and Power Reduction Techniques*. Version G. Cypress Semiconductor. May 2020. URL: https://www.cypress.com/documentation/application-notes/an77900-psoc-3-and-psoc-5lp-low-power-modes-and-power-reduction.

[53] W. Kester. *Understand SINAD, ENOB, SNR, THD, THD + N, and SFDR so You Don't Get Lost in the Noise Floor*. Rev. A. Analog Devices. Oct. 2008. URL: https://www.analog.com/media/en/training-seminars/tutorials/MT-003.pdf.

[54] *Delta Sigma Analog to Digital Converter*. Version 3.30. Cypress Semiconductor. Sept. 2020. URL: https://www.cypress.com/file/400466/download.

Appendix A

Code For the Initial MUX and ADC Experiments

```
#include <project.h>
#include "stdio.h"

/* UART Defines */
#define FALSE   0
#define TRUE    1
#define TRANSMIT_BUFFER_SIZE  16

/* There are 8 input channels */
#define NUMCHAN (8u)

int main()
{
    /* Initialize variable that indicates which mux channel
    is displayed on LCD */
    uint8 curChan = 0u, transChan;
    AMux_1_Init();
    AMux_1_FastSelect(curChan);
    /* Variable to store ADC result */
    uint32 Output0 = 0;
    uint32 Output1 = 0;
    /* Variable to store UART received character */
    uint8 Ch;
    /* Flags used to store transmit data commands */
    uint8 ContinuouslySendData;
    uint8 SendSingleByte;
    /* Transmit Buffer */
    char TransmitBuffer[TRANSMIT_BUFFER_SIZE];

    /* Start the UART */
    UART_1_Start();

    /* Initialize Variables */
    ContinuouslySendData = FALSE;
    SendSingleByte = FALSE;

    /* Send message to verify COM port is connected properly */
    UART_1_PutString("COM Port Open");

    ADC_Start();

    for(;;)
    {
        transChan = curChan;
        Output0 = Output1;
        /* If SW is pressed */
        if(!ChannelSelect_Read())
        {
            ADC_StartConvert();
            if(ADC_IsEndConversion(ADC_WAIT_FOR_RESULT))
            {
                Output1 = ADC_CountsTo_mVolts(ADC_GetResult16());
            }

            /* Wait until button is released */
            while(!ChannelSelect_Read())
            {
            }

            /* Increment to next channel for display */
            curChan++;
            AMux_1_FastSelect(curChan);

            /* If we are at channel 8, reset to channel 0 */
            if(curChan == NUMCHAN)
            {
                curChan = 0u;
            }
        }

         /* Non-blocking call to get the latest data recieved  */
        Ch = UART_1_GetChar();

        /* Set flags based on UART command */
        switch(Ch)
        {
            case 0:
                /* No new data was recieved */
                break;
            case 'C':
            case 'c':
                SendSingleByte = TRUE;
                break;
            case 'S':
            case 's':
                ContinuouslySendData = TRUE;
                break;
            case 'X':
            case 'x':
                ContinuouslySendData = FALSE;
                break;
            default:
                break;
        }

        if((SendSingleByte || ContinuouslySendData)
        && (Output0 != Output1 || curChan != transChan))
        {
            /* Format ADC result for transmition */
            sprintf(TransmitBuffer, "Channel number %i
            with the value: %lu mV\r\n", transChan, Output1);
            /* Send out the data */
            UART_1_PutString(TransmitBuffer);
            /* Reset the send once flag */
            SendSingleByte = FALSE;
        }
    }
}
```

Listing A.1: Code for Inicial MUX and ADC Experiments

Appendix B

IoT Node Schematic and Layout

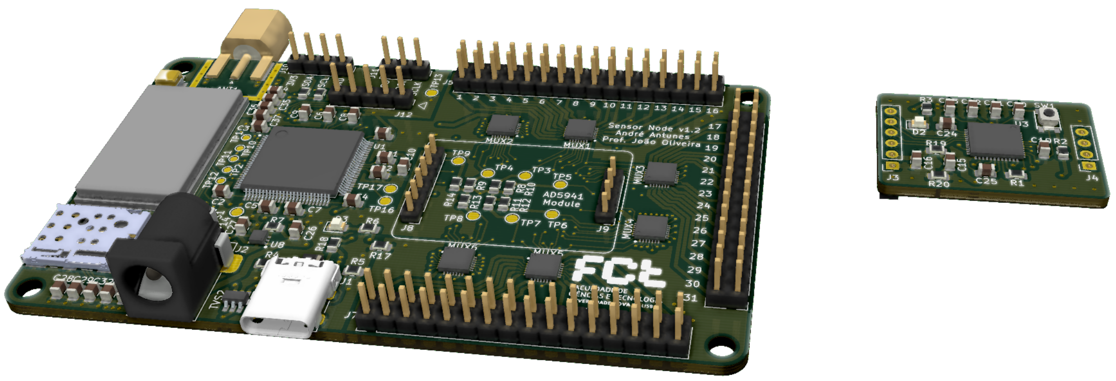

Figure B.1: 3D Render of the IoT Node's PCB and AD5941 Daughter Board.

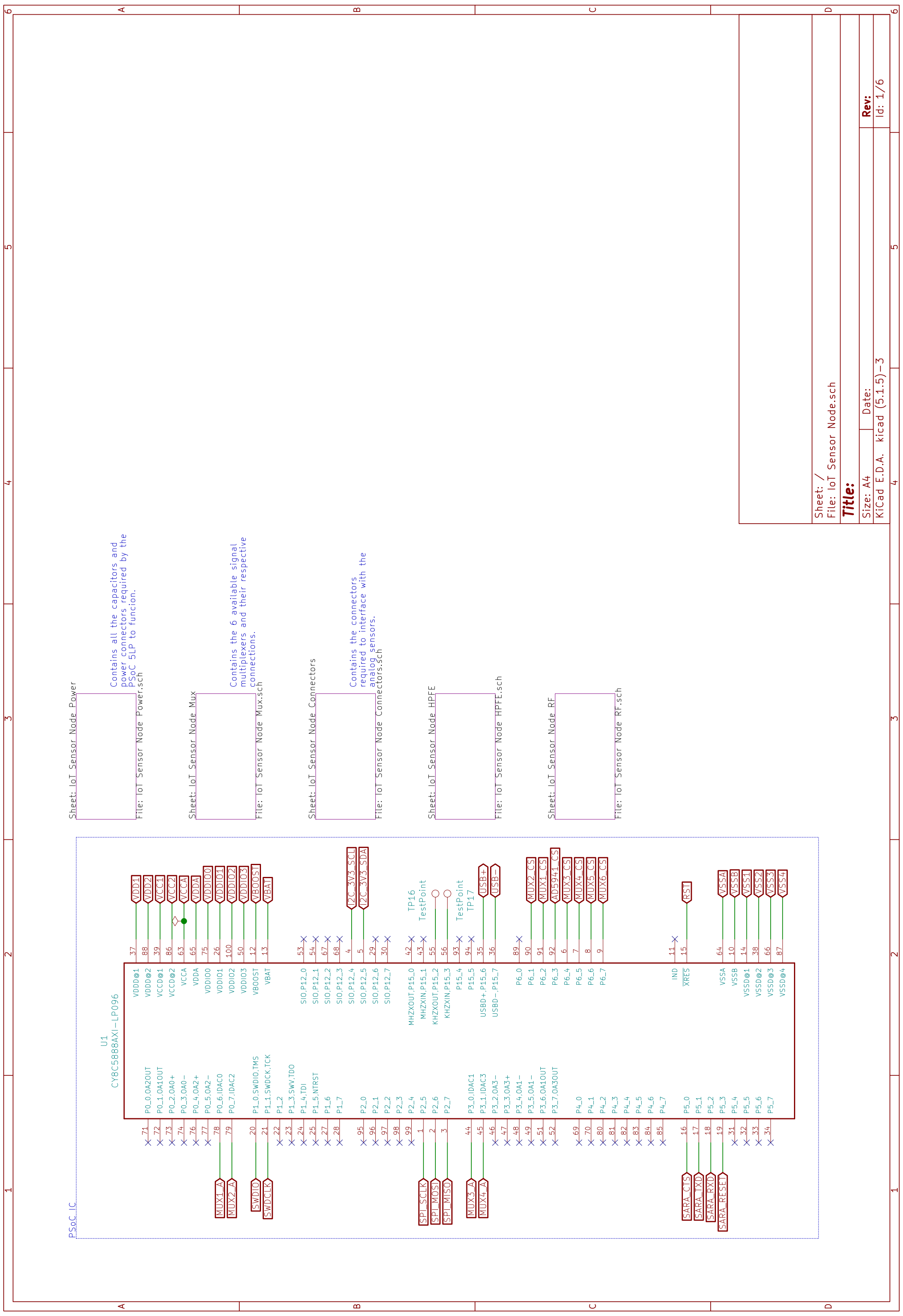
Sheet: IoT Sensor Node Power
File: IoT Sensor Node Power.sch
Contains all the capacitors and power connectors required by the PSoC 5LP to funcion.
Sheet: IoT Sensor Node Mux
File: IoT Sensor Node Mux.sch
Contains the 6 available signal multiplexers and their respective connections.
Sheet: IoT Sensor Node Connectors
File: IoT Sensor Node Connectors.sch
Contains the connectors required to interface with the analog sensors.
Sheet: IoT Sensor Node HPFE
File: IoT Sensor Node HPFE.sch
Sheet: IoT Sensor Node RF
File: IoT Sensor Node RF.sch
U1
CY8C5888AXI-LP096
PSoC IC
TP16 TestPoint
TestPoint TP17
I2C_3V3_SCL
I2C_3V3_SDA
USB+
USB-
RST
MUX1_A
MUX2_A
SWDIO
SWDCLK
SPI_SCLK
SPI_MOSI
SPI_MISO
MUX3_A
MUX4_A
SARA_CTS
SARA_TX
SARA_RX
SARA_RESET
Sheet: /
File: IoT Sensor Node.sch
Title:
Size: A4
Date:
Rev:
KiCad E.D.A. kicad (5.1.5)-3
Id: 1/6

Figure B.2: Sensor Node Schematic, Page 1.

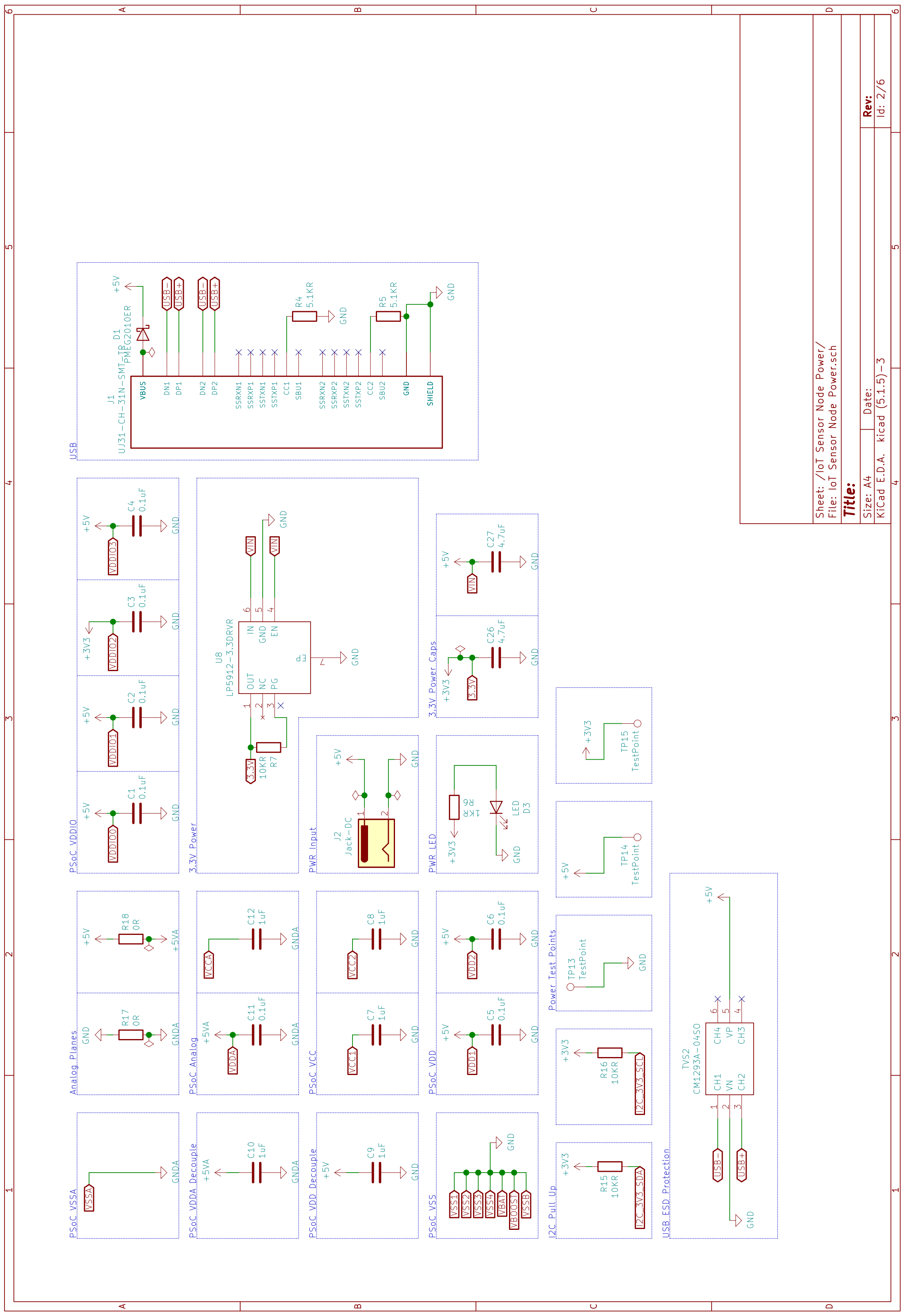

Figure B.3: Sensor Node Schematic, Page 2.

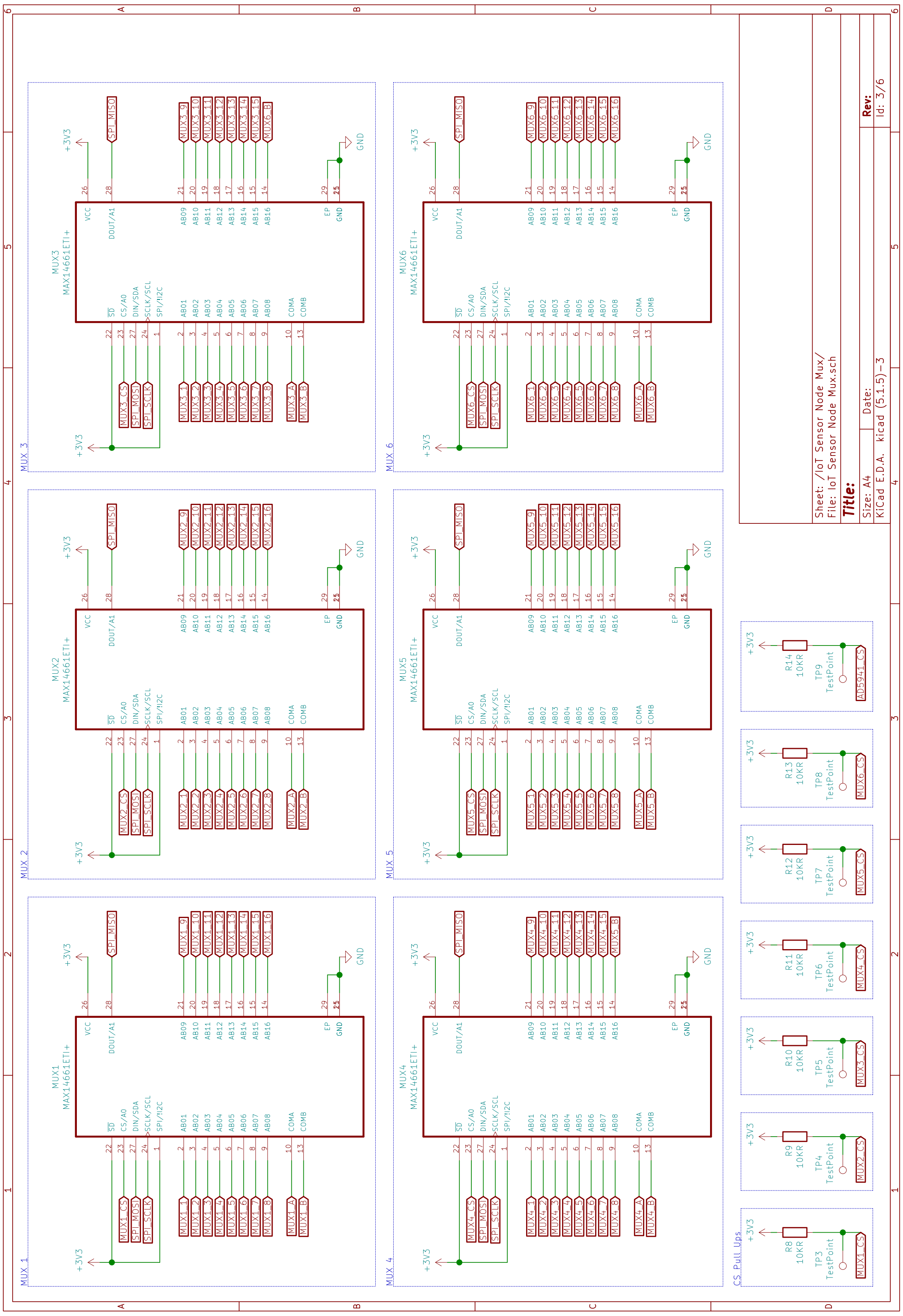

Figure B.4: Sensor Node Schematic, Page 3.

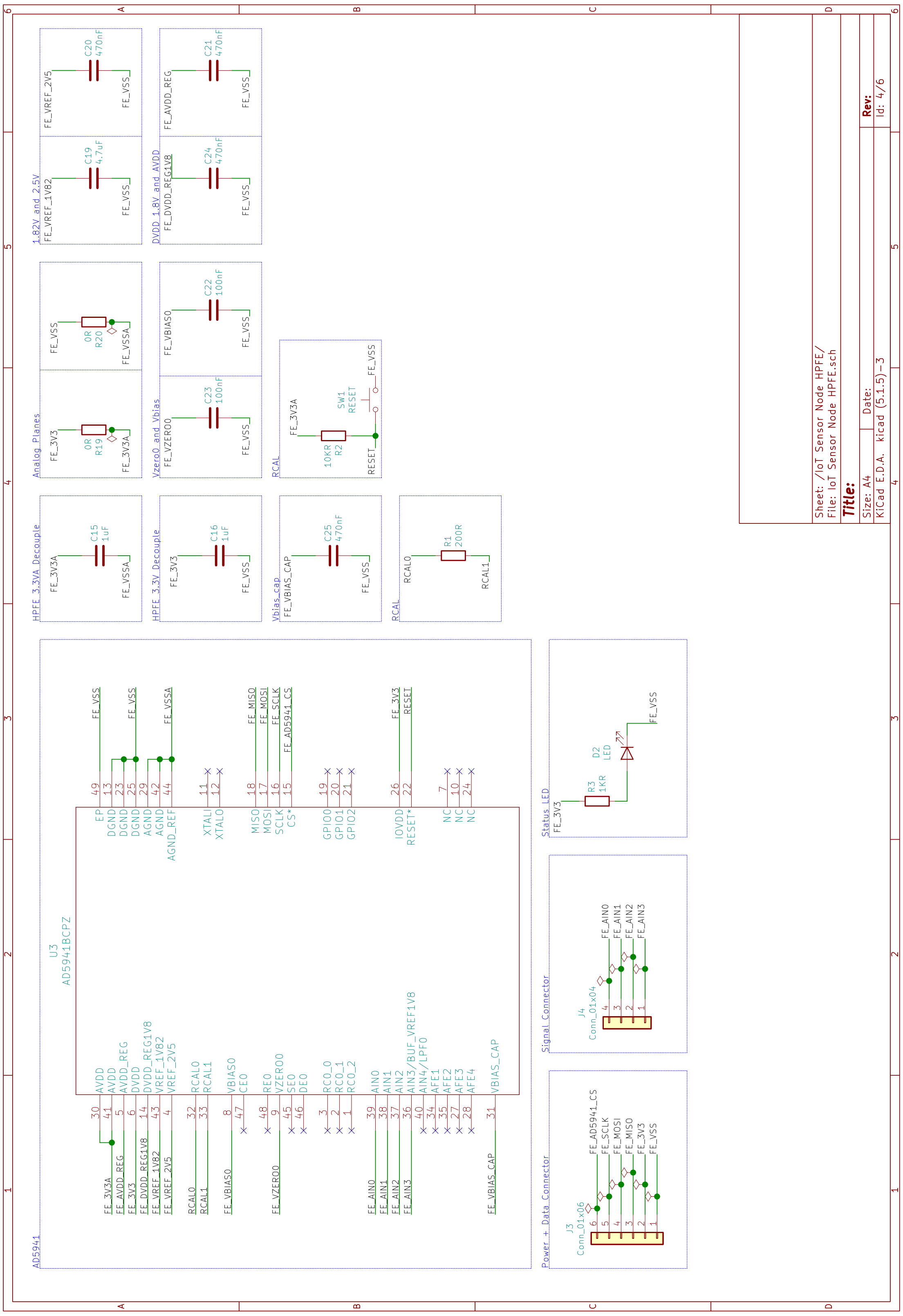

Figure B.5: Sensor Node Schematic, Page 4.

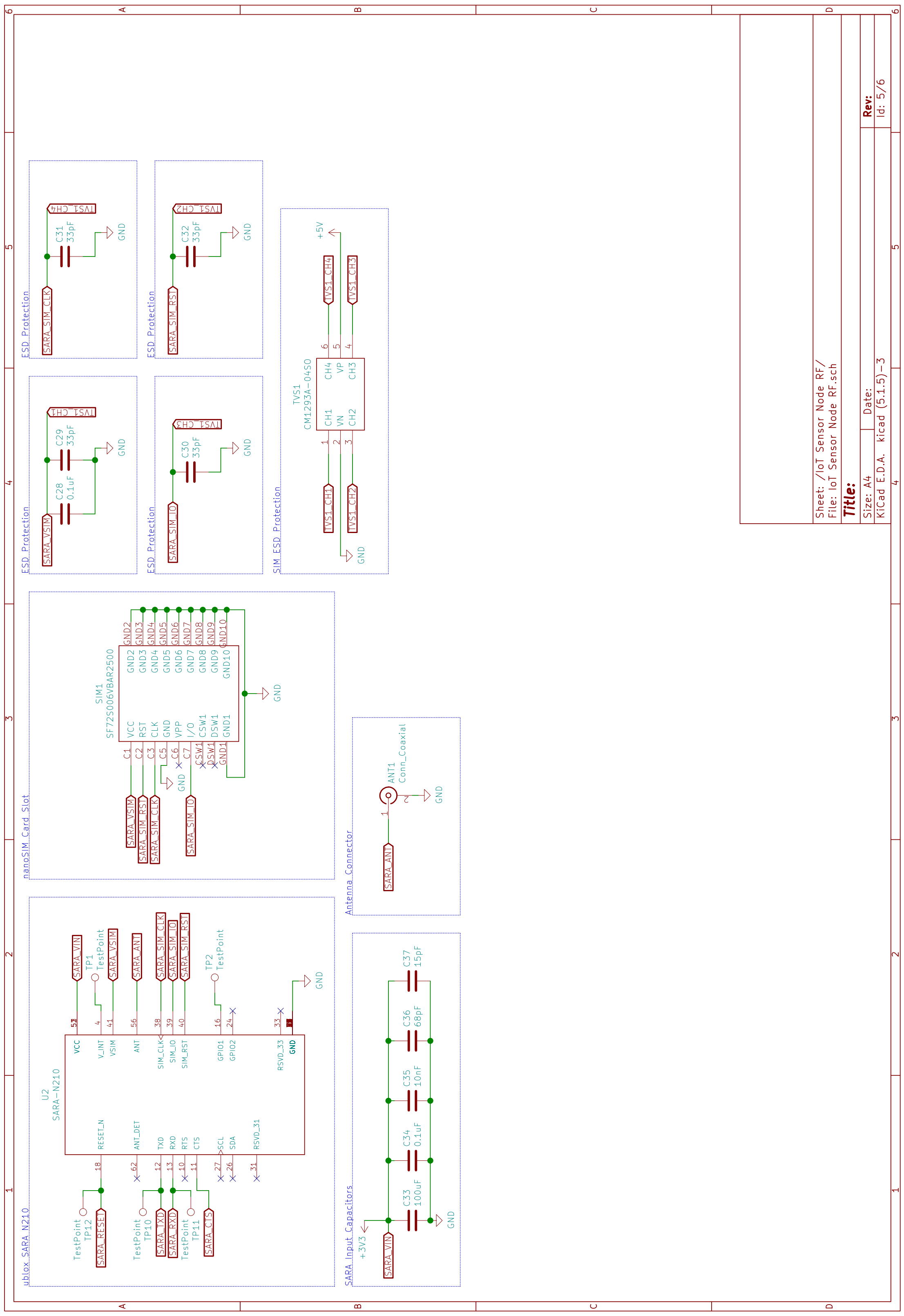

Figure B.6: Sensor Node Schematic, Page 5.

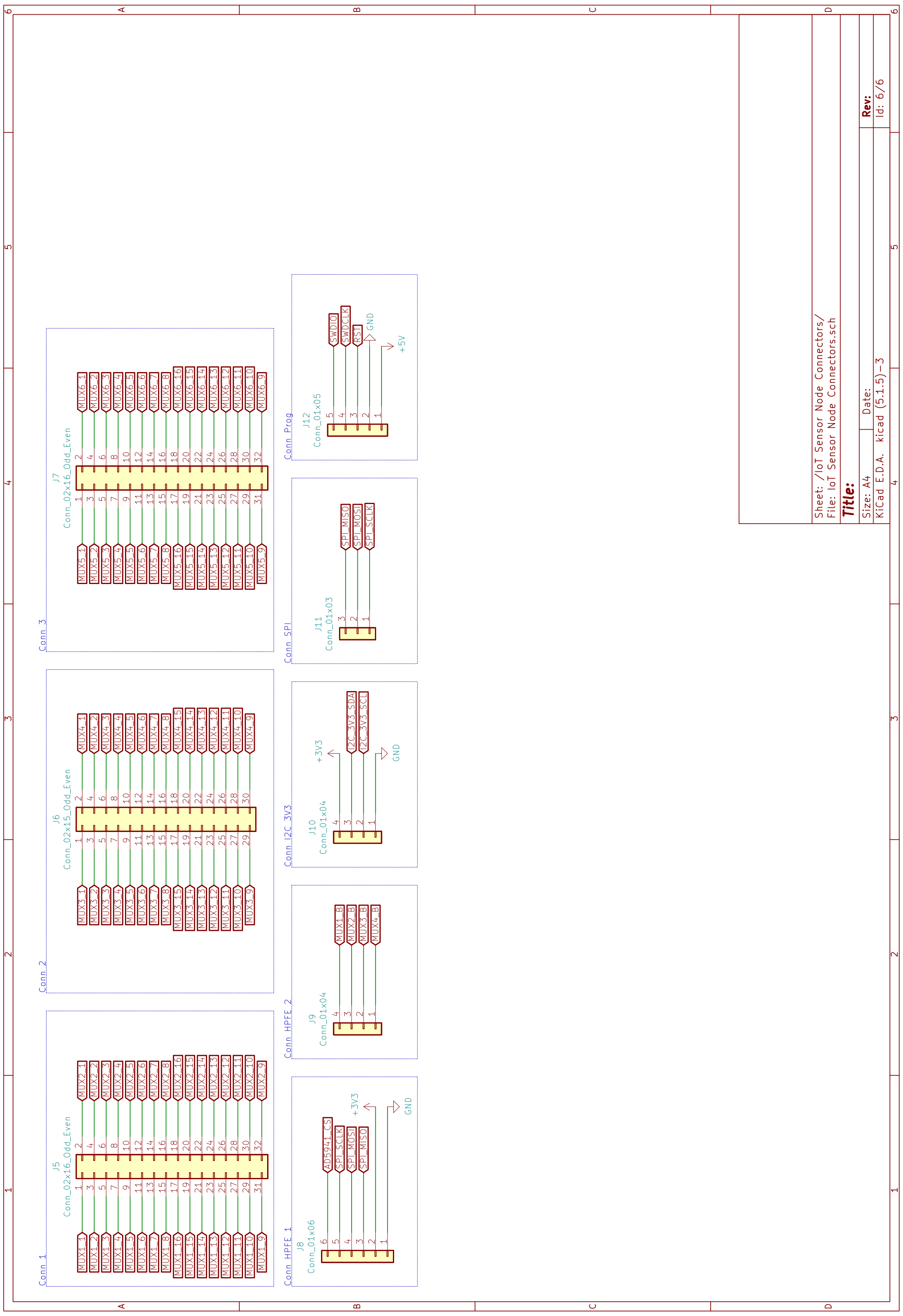

Figure B.7: Sensor Node Schematic, Page 6.

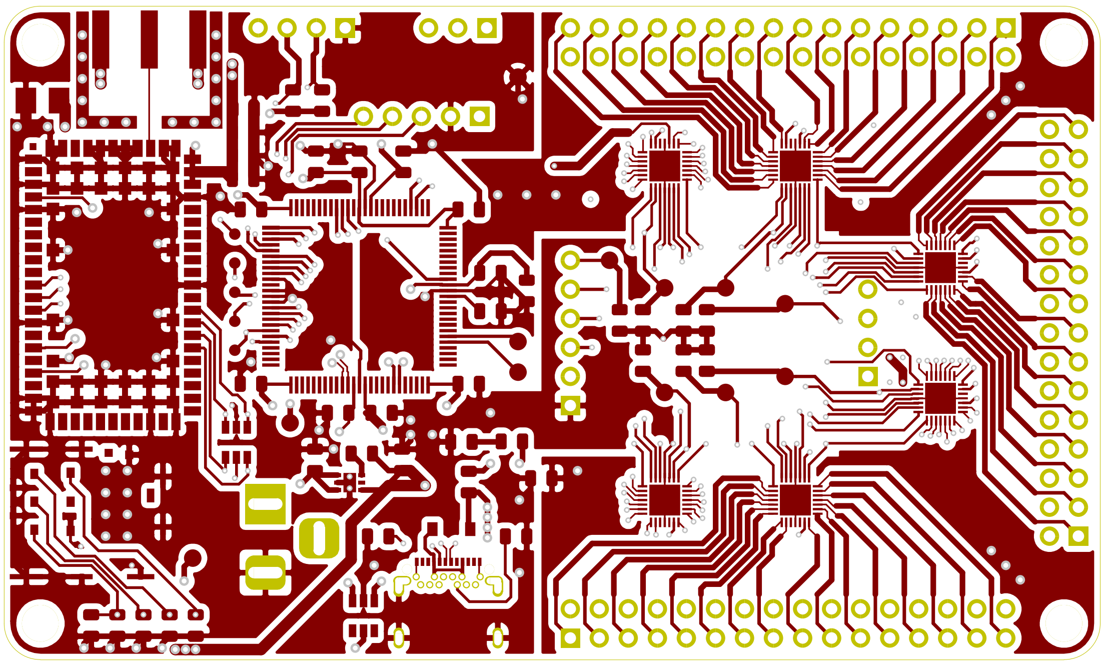

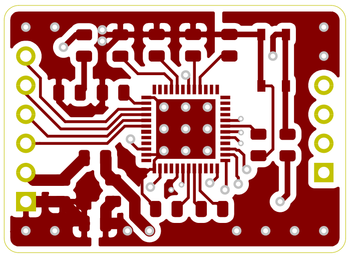

Figure B.8: Sensor Node Layout, Top Copper Layer.

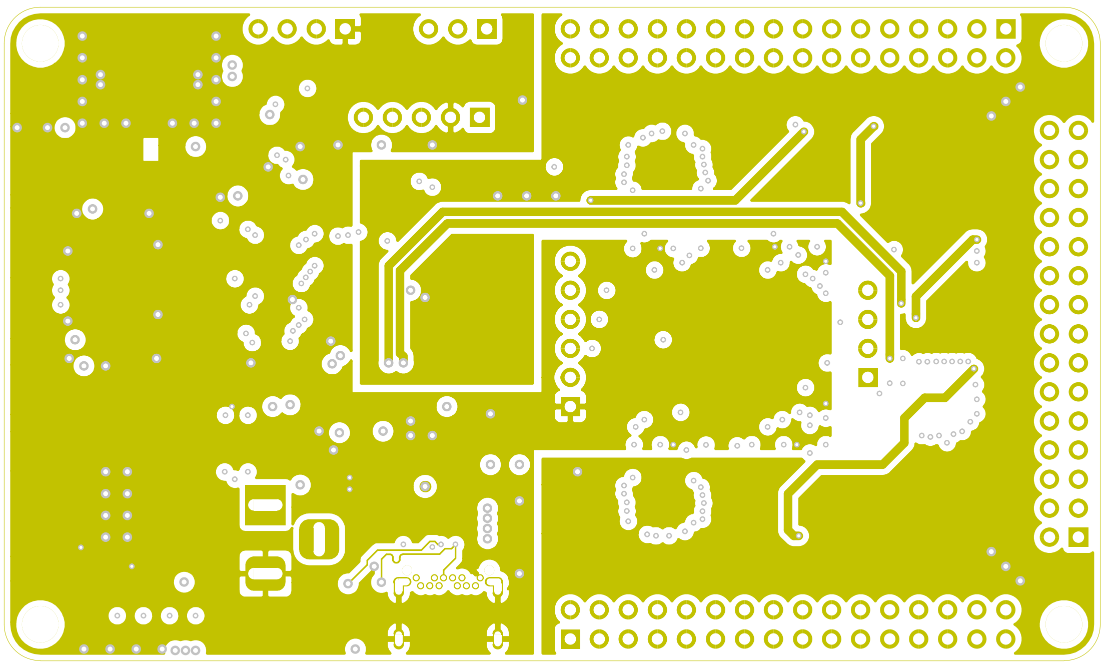
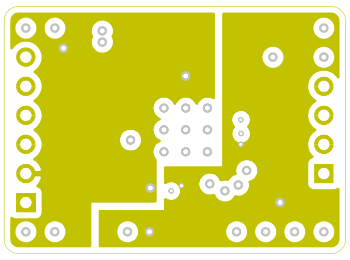
Figure B.9: Sensor Node Schematic, First Inside Copper Layer.

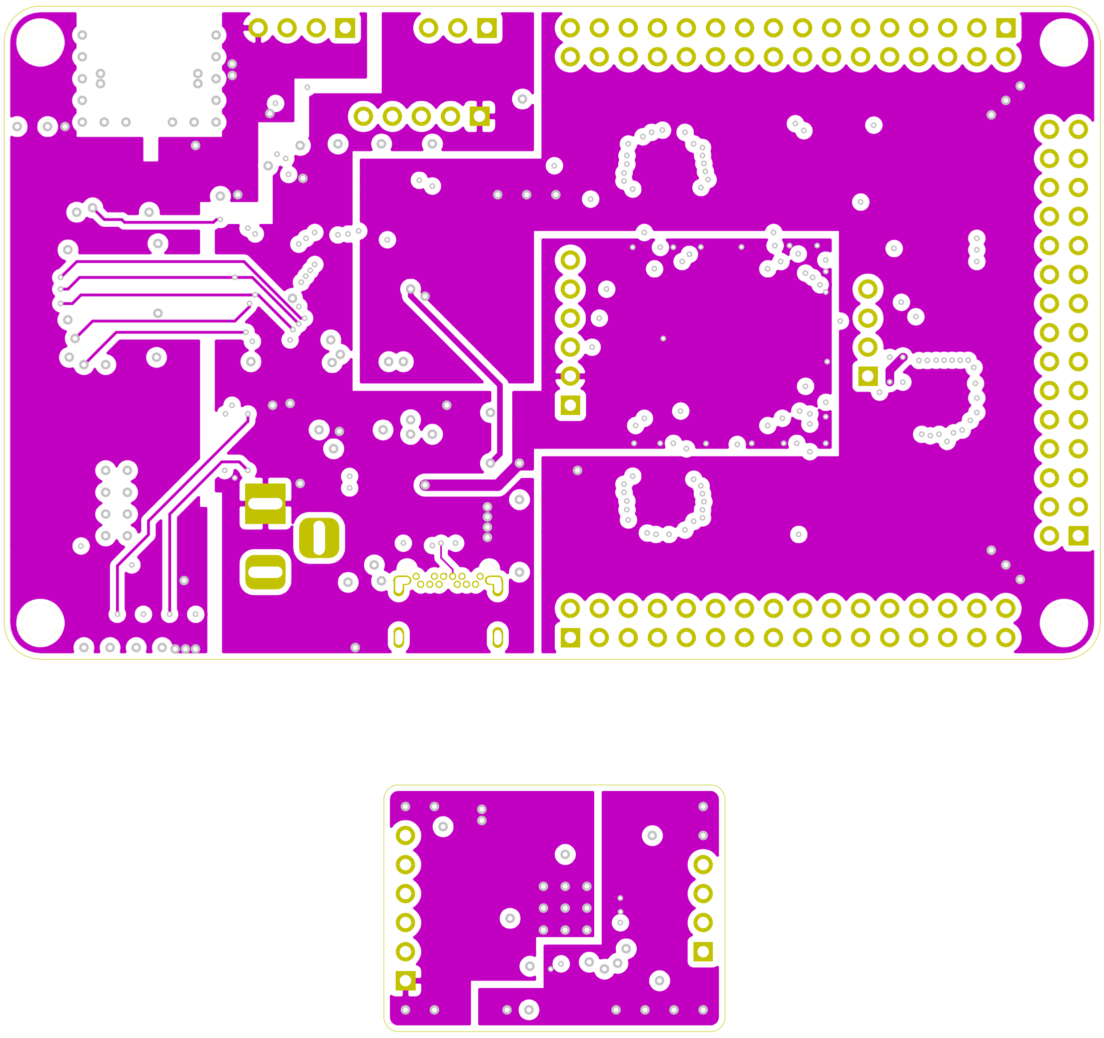

Figure B.10: Sensor Node Schematic, Second Inside Copper Layer.

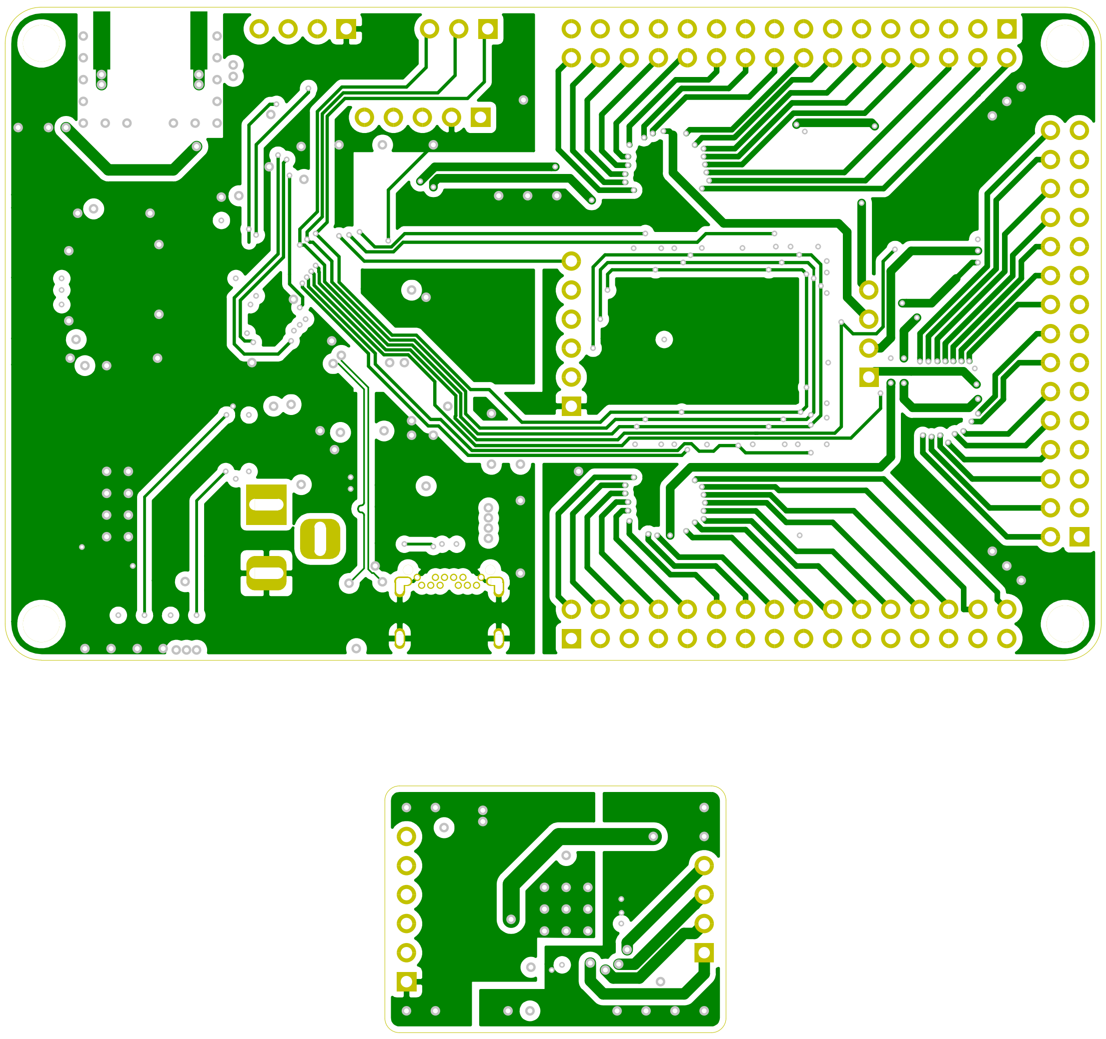
Figure B.11: Sensor Node Schematic, Bottom Copper Layer.

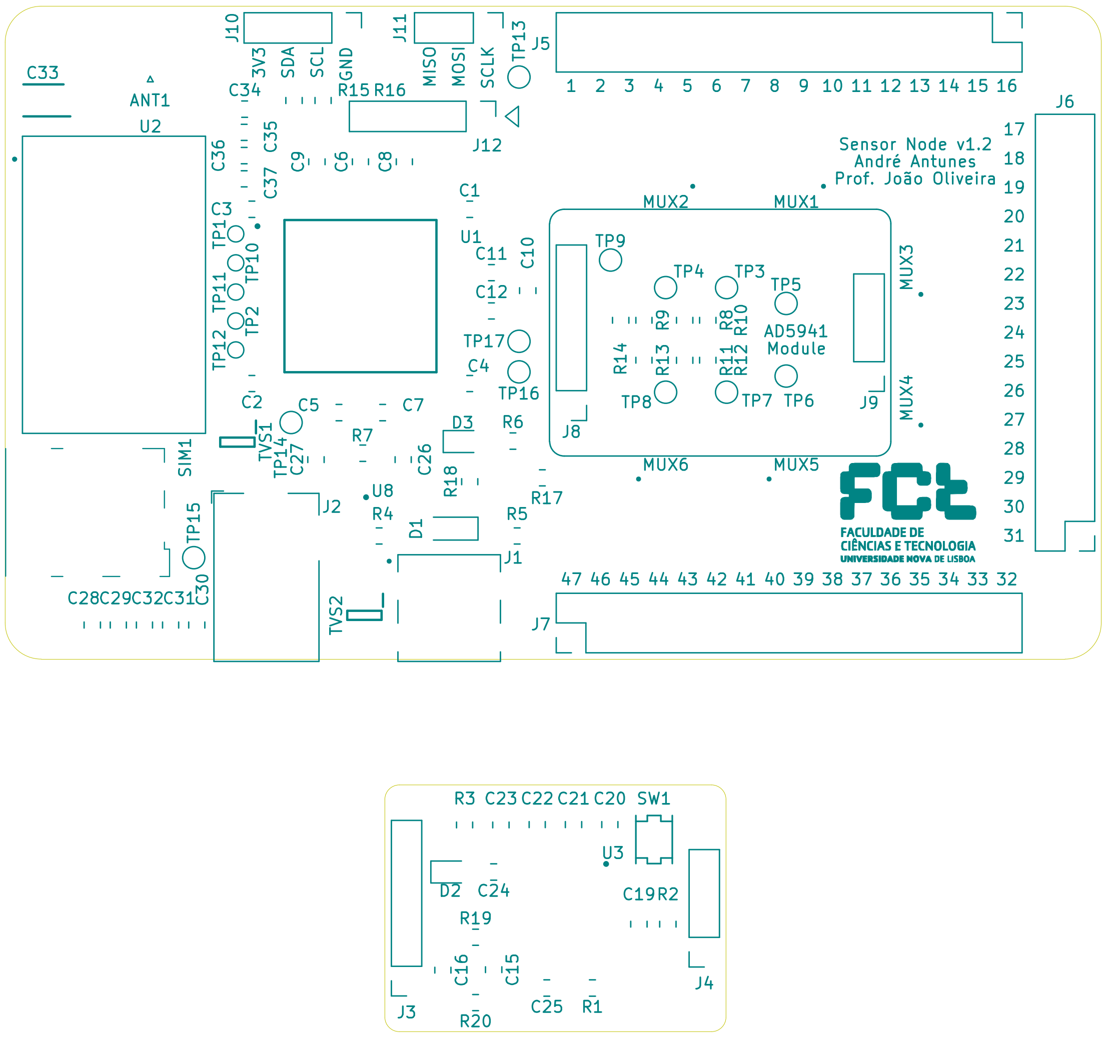

Figure B.12: Sensor Node Schematic, Top Silkscreen.

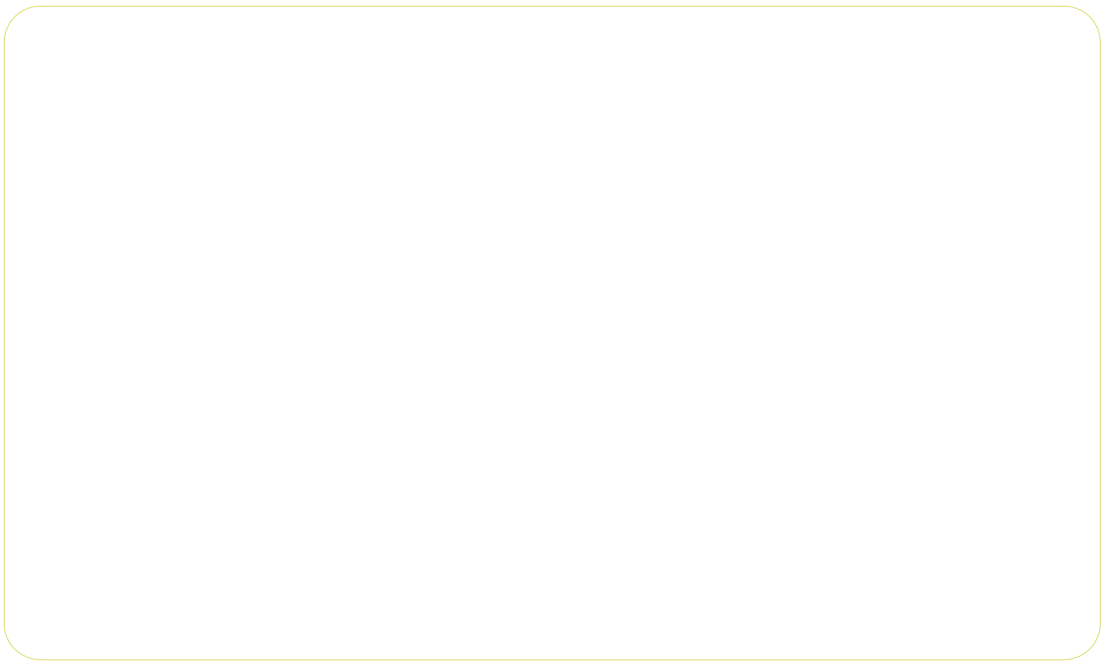

AD5941 Board v1.1
André Antunes
Prof. João Oliveira

Figure B.13: Sensor Node Schematic, Bottom Silkscreen.

Appendix C

PSoC Creator Analog Routing Window

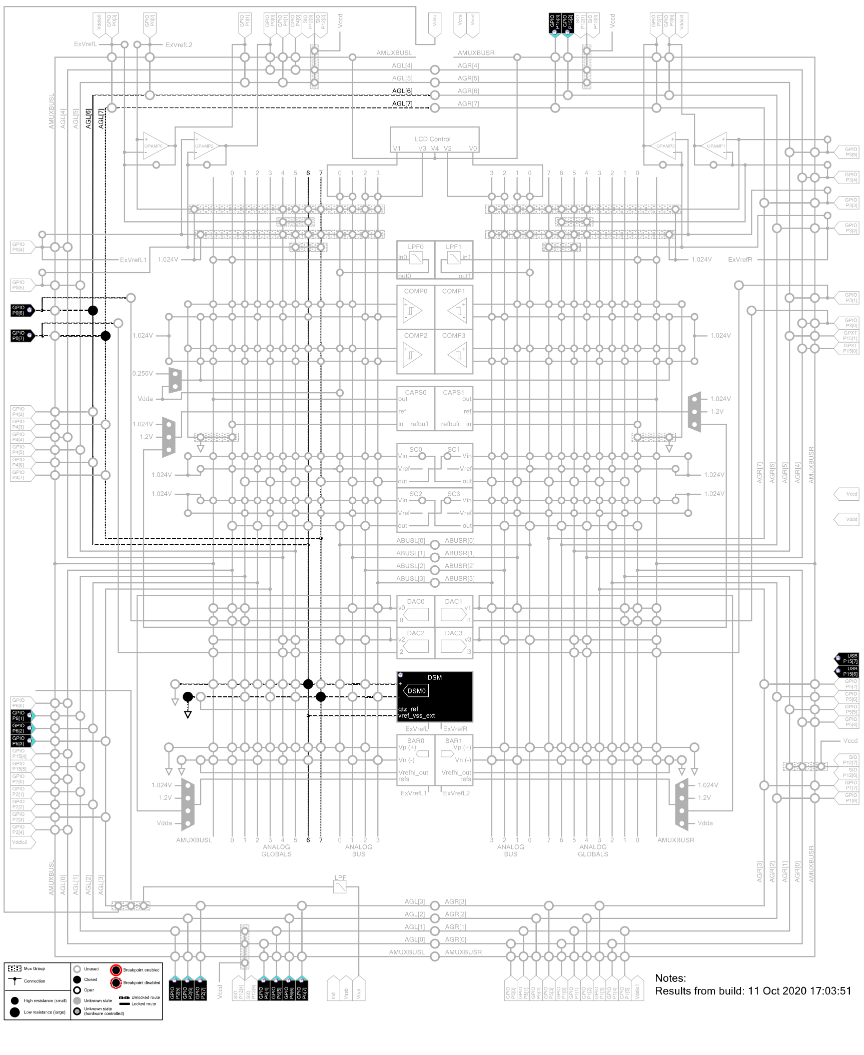

Figure C.1: PSoC Creator Analog Routing.

Appendix D

MATLAB Script for Sampled Data Processing

```
clear all
close all

tic
for c = 1:11
    switch c
        case 1
            data = csvread('20b_ds_mst_92_bg2_5k.csv');
            data(:,2) = [];
            n = 0.5;
            lsb = 1.024 / 2^21 * 10^6;
            figure(c)
            sgtitle({'20-bit DelSig ADC, Multi Sample (Turbo), SR = 92 SPS,
    Buf. Gain = 2, 5.000 Samples per Measurement', ' '}, 'FontSize', 28);
        case 2
            data = csvread('20b_ds_mst_182_bg1_5k.csv');
            data(:,2) = [];
            n = 0.5;
            lsb = 1.024 / 2^20 * 10^6;
            figure(c)
            sgtitle({'20-bit DelSig ADC, Multi Sample (Turbo), SR = 182 SPS,
    Buf. Gain = 1, 5.000 Samples per Measurement', ' '}, 'FontSize', 28);
        case 3
            data = csvread('18b_ds_mst_1238_bg2_10k.csv');
            data(:,2) = [];
            n = 1;
            lsb = 1.024 / 2^19 * 10^6;
            figure(c)
            sgtitle({'18-bit DelSig ADC, Multi Sample (Turbo), SR = 1238 SPS, Buf. Gain = 2, 10.000 Samples per Measurement', ' '}, 'FontSize', 28);
        case 4
            data = csvread('18b_ds_mst_2477_bg1_10k.csv');
            data(:,2) = [];
            n = 1;
            lsb = 1.024 / 2^18 * 10^6;
            figure(c)
            sgtitle({'18-bit DelSig ADC, Multi Sample (Turbo), SR = 2477 SPS, Buf. Gain = 1, 10.000 Samples per Measurement', ' '}, 'FontSize', 28);
        case 5
            data = csvread('16b_ds_mst_5505_bg2_20k.csv');
            data(:,2) = [];
            n = 2;
            lsb = 1.024 / 2^17 * 10^6;
            figure(c)
            sgtitle({'16-bit DelSig ADC, Multi Sample (Turbo), SR = 5505 SPS, Buf. Gain = 2, 20.000 Samples per Measurement', ' '}, 'FontSize', 28);
        case 6
            data = csvread('16b_ds_mst_11010_bg1_20k.csv');
            data(:,2) = [];
            n = 2;
            lsb = 1.024 / 2^16 * 10^6;
            figure(c)
            sgtitle({'16-bit DelSig ADC, Multi Sample (Turbo), SR = 11010 SPS, Buf. Gain = 1, 20.000 Samples per Measurement', ' '}, 'FontSize', 28);
        case 7
            data = csvread('14b_ds_mst_14840_bg2_20k.csv');
            data(:,2) = [];
            n = 2;
            lsb = 1.024 / 2^15 * 10^6;
            figure(c)
            sgtitle({'14-bit DelSig ADC, Multi Sample (Turbo), SR = 14840 SPS, Buf. Gain = 2, 20.000 Samples per Measurement', ' '}, 'FontSize', 28);
        case 8
            data = csvread('14b_ds_mst_29681_bg1_20k.csv');
            data(:,2) = [];
            n = 2;
            lsb = 1.024 / 2^14 * 10^6;
            figure(c)
            sgtitle({'14-bit DelSig ADC, Multi Sample (Turbo), SR = 29681 SPS, Buf. Gain = 1, 20.000 Samples per Measurement', ' '}, 'FontSize', 28);
        case 9
            data = csvread('20b_ds_mst_182_bg1_5k_high.csv');
            data(:,2) = [];
            n = 0.5;
            lsb = 1.024 / 2^20 * 10^6;
            figure(c)
            sgtitle({'High value resistors, 20-bit DelSig ADC, Multi Sample (Turbo), SR = 182 SPS, Buf. Gain = 1, 5.000 Samples per Measurement', ' '}, 'FontSize', 28);
        case 10
            data = csvread('18b_ds_mst_2477_bg1_10k_high.csv');
            data(:,2) = [];
            n = 1;
            lsb = 1.024 / 2^18 * 10^6;
            figure(c)
            sgtitle({'High value resistors, 18-bit DelSig ADC, Multi Sample (Turbo), SR = 2477 SPS, Buf. Gain = 1, 10.000 Samples per Measurement', ' '}, 'FontSize', 28);
        case 11
            data = csvread('16b_ds_mst_11010_bg1_20k_high.csv');
            data(:,2) = [];
            n = 2;
            lsb = 1.024 / 2^16 * 10^6;
            figure(c)
            sgtitle({'High value resistors, 16-bit DelSig ADC, Multi Sample (Turbo), SR = 11010 SPS, Buf. Gain = 1, 20.000 Samples per Measurement', ' '}, 'FontSize', 28);
    end

    setGlobala(1);
    set(gcf, 'Position', [100, 100, 1600, 900])

    data_1u_22r = data(1:(n * 10000));
    data_1u_465r = data((1 + n * 10000):(n * 20000));
    data_1u_992r = data((1 + n * 20000):(n * 30000));

    data_10u_22r = data((1 + n * 30000):(n * 40000));
    data_10u_465r = data((1 + n * 40000):(n * 50000));
    data_10u_992r = data((1 + n * 50000):(n * 60000));

    data_100u_22r = data((1 + n * 60000):(n * 70000));
    data_100u_465r = data((1 + n * 70000):(n * 80000));
    data_100u_992r = data((1 + n * 80000):(n * 90000));

    [n1, n991, m1, s1, nlsb1] = process(data_1u_22r, lsb, 22, 1);
    [n2, n992, m2, s2, nlsb2] = process(data_1u_465r, lsb, 465, 1);
    [n3, n993, m3, s3, nlsb3] = process(data_1u_992r, lsb, 992, 1);
    [n4, n994, m4, s4, nlsb4] = process(data_10u_22r, lsb, 22, 10);
    [n5, n995, m5, s5, nlsb5] = process(data_10u_465r, lsb, 465, 10);
    [n6, n996, m6, s6, nlsb6] = process(data_10u_992r, lsb, 992, 10);
    [n7, n997, m7, s7, nlsb7] = process(data_100u_22r, lsb, 22, 100);
    [n8, n998, m8, s8, nlsb8] = process(data_100u_465r, lsb, 465, 100);
    [n9, n999, m9, s9, nlsb9] = process(data_100u_992r, lsb, 992, 100);

    m4 = m4 / 10; m5 = m5 / 10; m6 = m6 / 10;
    s4 = s4 / 10; s5 = s5 / 10; s6 = s6 / 10;

    m7 = m7 / 100; m8 = m8 / 100; m9 = m9 / 100;
    s7 = s7 / 100; s8 = s8 / 100; s9 = s9 / 100;

%      figure(1);

    subplot(1,3,1)
    x1 = [m1,m4,m7];
    y1 = 1:3;
    bar(y1, x1, 'FaceColor', [0.25, 0.25, 0.25])
    xticklabels({'1\mu', '10\mu', '100\mu'})
    if (c < 9)
        title({'22\Omega Resistor' , '(Measured at 21.7\Omega)'}, 'FontSize', 18)
    end
    if (c > 8)
        title({'3.3K\Omega Resistor' , '(Measured at 3.28K\Omega)'}, 'FontSize', 18)
    end
    ylim([0 50]);
    errlow = [2*s1 2*s4 2*s7];
    errhigh = [2*s1 2*s4 2*s7];
    hold on
    ax = plot(xlim,[21.7 21.7], 'LineWidth', 2);
    ax.Color = [0, 0.4470 0.7410];
    er = errorbar(y1, x1, errlow, errhigh);
    er.Color = 'r';
    er.LineStyle = 'none';
    er.LineWidth = 2;
    hold off
    xlabel('Polarization Current (A)', 'FontSize', 16);
    ylabel('Measured Resistor Value (\Omega)', 'FontSize', 16);
    ax = gca;
    ax.XAxis.FontSize = 16;
    ax.YAxis.FontSize = 16;

    subplot(1,3,2)
    x2 = [m2,m5,m8];
    bar(y1 ,x2, 'FaceColor', [0.25, 0.25, 0.25]);
    xticklabels({'1\mu', '10\mu', '100\mu'})
    if (c < 9)
        title({'470\Omega Resistor', '(Measured at 465\Omega)'}, 'FontSize', 18)
    end
    if (c > 8)
        title({'6.8K\Omega Resistor' , '(Measured at 6.76K\Omega)'}, 'FontSize', 18)
    end
    ylim([0 600]);
    errlow = [2*s2 2*s5 2*s8];
    errhigh = [2*s2 2*s5 2*s8];
    hold on
    ax = plot(xlim,[465 465], 'LineWidth', 2);
    ax.Color = [0, 0.4470 0.7410];
    er = errorbar(y1, x2, errlow, errhigh);
    er.Color = 'r';
    er.LineStyle = 'none';
    er.LineWidth = 2;
    hold off
    xlabel('Polarization Current (A)', 'FontSize', 16);
    ylabel('Measured Resistor Value (\Omega)', 'FontSize', 16);
    ax = gca;
    ax.XAxis.FontSize = 16;
    ax.YAxis.FontSize = 16;

    subplot(1,3,3)
    x3 = [m3,m6,m9];
    bar(y1, x3, 'FaceColor', [0.25, 0.25, 0.25])
    xticklabels({'1\mu', '10\mu', '100\mu'})
    if (c < 9)
        title({'1K\Omega Resistor' , '(Measured at 992\Omega)'}, 'FontSize',
    18)
    end
    if (c > 8)
        title({'10K\Omega Resistor' , '(Measured at 9.90K\Omega)'}, 'FontSize'
    , 18)
    end
    ylim([0 1200]);
    errlow = [2*s3 2*s6 2*s9];
    errhigh = [2*s3 2*s6 2*s9];
    hold on
    ax = plot(xlim,[992 992], 'LineWidth', 2);
    ax.Color = [0, 0.4470 0.7410];
    er = errorbar(y1, x3, errlow, errhigh);
    er.Color = 'r';
    er.LineStyle = 'none';
    er.LineWidth = 2;
    hold off
    xlabel('Polarization Current (A)', 'FontSize', 16);
    ylabel('Measured Resistor Value (\Omega)', 'FontSize', 16);
    ax = gca;
    ax.XAxis.FontSize = 16;
    ax.YAxis.FontSize = 16;

    figHandles = findall(0,'Type','figure');

    syms fig_bit;
    eqn = 2 == nthroot(lsb * 10^(-6), fig_bit);
    bits = solve(eqn, fig_bit);
    bits = abs(round(bits));

    bits = double(bits);
    text3 = [num2str(bits), 'bits'];
    fn = text3;


%     export_fig(fn, '-pdf', figHandles(1))
%     for i = numel(figHandles):-1:2
%      export_fig(fn, '-pdf', figHandles(i), '-append')
%     end

end
toc

function [noise, noise99, m, s, nlsb] = process(x, lsb, r, curr)
    n = length(x);
    noise = max(x)-min(x);
    m = sum(x)/n;
    s = std(x);
    noise99 = 6 * s;
    nlsb = s / lsb;

    tbl = tabulate(x);
    indices = tbl(:,2) == 0;
    tbl(indices,:) = [];

    tbl( all(~tbl,2), : ) = [];  %rows
    tbl( :, all(~x,1) ) = [];  %columns

    tbl = num2cell(tbl);
    t = cell2table(tbl, 'VariableNames', {'Value','Count','Percent'});
    t.Value = categorical(t.Value);


%     a = getGlobala;
%     set(0,'DefaultAxesTitleFontWeight','normal');
%     figure(a+1);
%     bar(t.Value, t.Count)
%     set(gcf, 'Position', [100, 100, 1600, 900])
%     ylabel('Number of Samples', 'FontSize', 16);
%     xlabel('Measured Voltage (\muV)', 'FontSize', 16);
%     text = ['99.7% Noise = ', num2str(noise99), ' \muV, RMS Noise = ',
    num2str(s), ' \muV (', num2str(nlsb), ' LSB)'];
%     text2 = ['Pol. Current = ', num2str(curr), ' \muA , Resistor Value = ',
    num2str(r), ' \Omega'];
%     title({text, text2, ' '}, 'FontSize', 28);
%
%     a = a + 1;
%     setGlobala(a);

```

```

end

function setGlobala(val)
    global a
    a = val;
end

function r = getGlobala
    global a
    r = a;
end
```

Listing D.1: MATLAB Script